Influence of Ground Effect on the Flying V Aircraft

A numerical investigation

Ankith J. Santosh

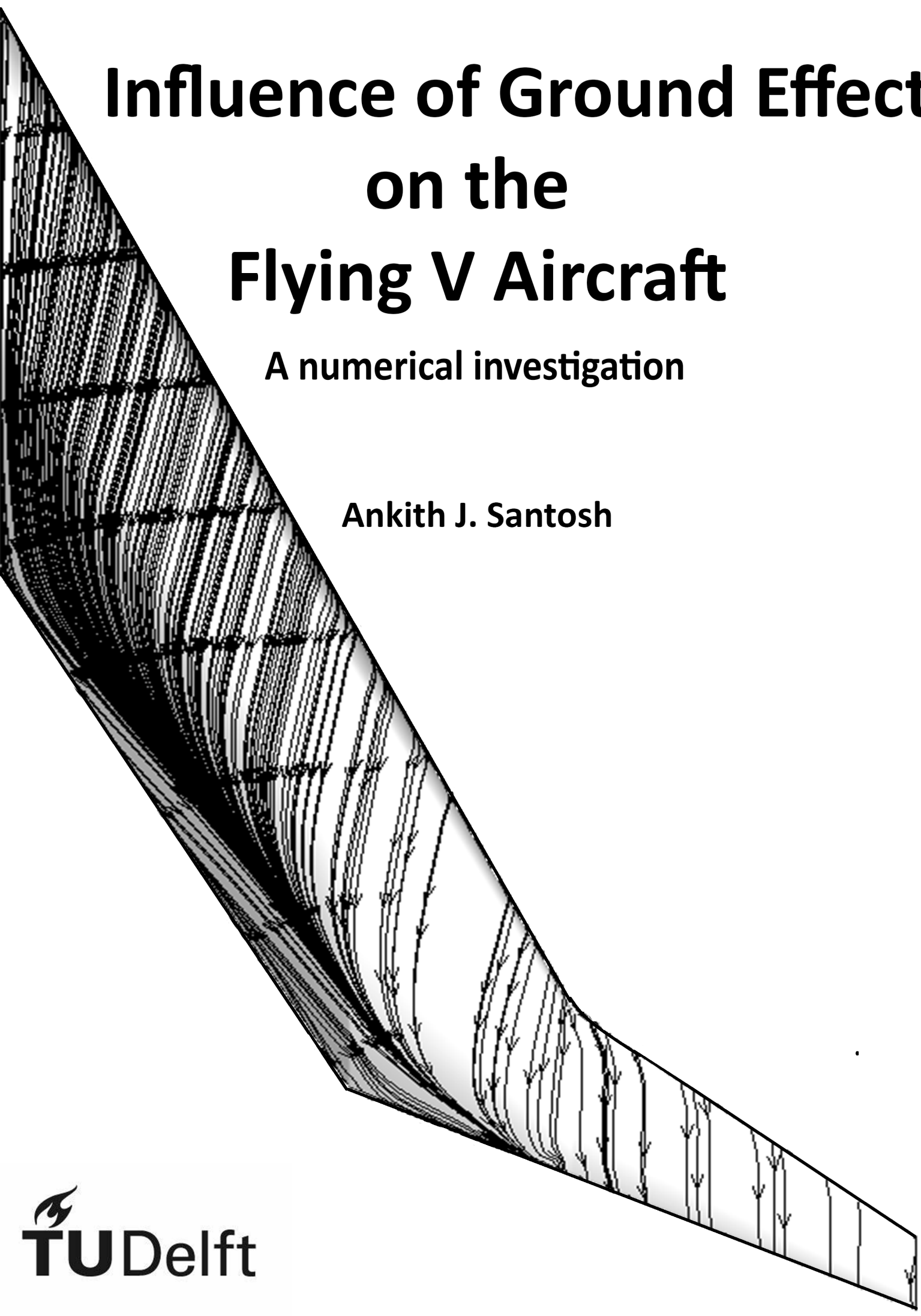

TU Delft

Influence of Ground Effect on the Flying V aircraft

A Numerical Investigation

by

Ankith J. Santosh

to obtain the degree of Master of Science
at the Delft University of Technology,
to be defended publicly on Thursday February 6, 2020 at 01:00 PM.

Student number:	4615611	
Project duration:	January 24, 2019 – January 24, 2020	
Thesis committee:	Prof. dr. ir. L.L.M. Veldhuis,	TU Delft, chair of the committee
	Dr. ir. R. Vos,	TU Delft, supervisor
	Dr. ir. M.I. Gerritsma,	TU Delft, committee member

TU Delft

Preface

Looking back to the day that I first set sail on this three and a half year long journey at the Delft University of Technology, I realize how immensely lucky and fortunate I have been. The experiences I've had have taught me so much, not just from the perspective of education, but also about who I am as a person. I have met and interacted with a lot of people who have greatly and positively influenced this journey. Given this opportunity, it would only be fitting for me to thank them.

At the foremost, I would like to express my deepest gratitude to my supervisor, Dr. Roelof Vos. It wasn't just a privilege to be able to learn and work alongside him, but without his constant guidance, understanding and support this project would not have been realized. When at times I found myself at a dead end, thank you for listening and motivating me to persist and persevere.

I am greatly indebted to Marco Palermo for the invaluable assistance he provided in helping me find quick and clever ways to overcome many a hurdle during the course of this entire thesis. It was only through his willingness to share his knowledge and expertise in computational fluid dynamics that I was able to run the plethora of simulations that were needed for garnering the results of this thesis. Grazie mille Marco!

A special word of mention to Jac van Egmond from mvAero for lending me his Large Eddy Simulations results to carry out my validation study on the Flying V. I would also like to thank John Stokes from ANSYS Canada for taking time out of his busy schedule to help me with different aspects of the mesh generation process.

Without the friends and colleagues who have been by my side from day one, this journey would never have reached its culmination. Thank you Sanjeet and Maria for always helping with assignments, solving doubts and moral support. Abhinand, Athreya, Nikhil, Sampath, Siddharth, Shubham and Jatinder - friends who I have the fortune of calling my brothers. Thank you for your patience and kindness in always ensuring that I took the right steps to fulfill this project. Only because I surrounded myself with friends like you I have been able to learn so much more than I ever imagined.

Thank you Roshan, Gautham, Krithika, Alan, Supriya, Namrata and Amulya for being the most amazing best friends. I really appreciate you all flying thousands of kilometers just to spend a couple of weeks here in Netherlands with me. Thank you for always checking on me and being awesome stress busters.

I owe an immense debt of gratitude to Nikhilesh, Kushal and Akshar. Over the past 1.5 years, you'll have taught me so much about hard work, the benefits of loving what you do, committing to achieving a goal and the importance of making sacrifices but never giving up. The three of you, through your hard work, humility and dedication have always stood as pillars of inspiration. I owe you all so much.

Finally, I take this opportunity to thank my parents and my sister. Through the complete faith they have always had in my ability, I was always allowed to pursue all and any of my ambitions. For this I am grateful. Their unconditional love and prayers have molded me into the person that I am today. Mummy, Papa and Ashu, I would never have made it to the Delft University of Technology without all the sacrifices you made and still continue to make each day for me. I want you to know that they do not go unnoticed. For this reason, I dedicate this thesis to you.

Ankith J. Santosh
Delft, February 2020

Abstract

In order to meet the growing market demands of quieter, more aerodynamically efficient aircrafts, manufacturers constantly strive to innovate and optimize their designs. Over the years however, the extent of innovation related to the conventional 'tubular fuselage' configurations have somewhat reached a stalemate as the gains obtained have only been marginal. It is for this reason, there has off-late been a surge in research pertaining to unconventional aircraft design and configurations. The Flying V (FV) is one such alternative that was conceptualized by J. Benad at TU Berlin along with the Future Projects Office (FPO) at Airbus Operations GmbH in Hamburg. Results obtained from past studies show a 25 % improvement in the lift to drag ratio of the FV as compared to the NASA Common Research Model (CRM), which was set as the basis of comparison for a fixed wing aircraft configuration. So far, aerodynamic studies have only focused on the cruise performance of the FV without any emphasis on its low speed behavior. Conventional aircrafts use high lift devices like flaps and slats to improve stability and increase the amount of lift its wings produce at lower speeds. The FV however, has no such high lift device and solely relies on the lift produced by its wing to achieve a speed that is low enough to land safely. For this reason, this thesis aims to investigate the influence of ground proximity on the lift, drag and pitching moments of the FV which in turn affect its take-off and landing characteristics.

Compressible RANS equations were solved with the k-omega SST turbulence model using ANSYS Fluent on a 4.6% scaled model of the FV. The ground was numerically realized by employing the moving ground boundary condition equal in velocity to the free stream. Results from these simulations have shown a 11% reduction in the drag polar of the FV when closest to the ground as compared to when in unbounded flow. Additionally, the proximity to the ground causes an increase in lift and this allows the FV to touch down at 19 degrees while the maximum rotation angle during take-off is predicted to be about 13 degrees for a positive climb gradient when also considering the One-Engine-Idle (OEI) scenario. This corresponds to a lift to drag ratio equal to 10 and a lift-off lift coefficient of 0.56 approximately.

The effect of ride height on the longitudinal stability of the FV showed that favorable pitching moments were obtained for angles of attack between 0° and 5° degrees and for angles greater than 17.5°. A near wake analysis was also performed for different angles of attack and at different heights from the ground to investigate the flow phenomena over the FV and the evolution of the wake downstream. No significant span wise flow is seen when $\alpha = 0°$ and the flow appears to travel parallel to the stream-wise direction. Additionally, in case of very high angles of attack, the flow streamlines confirm the occurrence of a large vortex emanating from the leading edge kink of the wing. When in unbounded flow a secondary vortex located inboard is produced at $\alpha = 17°$. The diameter of the tip vortex is seen to be greater than the inboard secondary vortex for $\alpha = 17°$. At greater angles of attack, the secondary vortex is seen to grow in diameter as the height reduces.

Contents

List of Figures

List of Tables

Nomenclature

Latin symbols

b	Wing span	[m]
$\bar{c}$	Mean geometric chord	[m]
C_L	Coefficient of lift	[-]
C_D	Coefficient of drag	[-]
$C_{D,0}$	Parasite drag coefficient at zero lift ($\alpha_L = 0$)	[-]
C_f	Coefficient of Skin friction	[-]
C_p, C_V	Heat capacity at constant pressure and volume	$[\frac{J}{molK}]$
D	Drag force	[N]
D_i	Induced drag	[N]
e	Oswald efficiency factor	[-]
$e-0$	Total energy	[J]
g	Acceleration due to gravity	$[ms^{-2}]$
h	Fuel Energy per unit mass [J/kg]	
k	Turbulence kinetic energy	$[Jkg^{-1}]$
Kn	Knudsen number	[-]
L	Lift Force associated with the free stream velocity	[N]
L	Representative physical length scale	[m]
L'	Lift Force associated with the local effective velocity	[N]
M	Mach number	[-]
$\dot{m}_f$	Fuel mass flow rate	[kg/s]
n	Amount of substance/ number of moles	[-]
P	Pressure	[Pa]
R	Ideal gas constant	[J/mol·K]
Re	Reynolds number	[-]
S	Sutherland Constant	[K]
S_{ref}	Reference area	$[m^2]$
T	Ambient Temperature	[K]
T_{ref}	Reference Temperature	[K]
T	Thrust	[N]
$u_{i,j}$	Components of velocity in the x, y, z directions	$[ms^{-1}]$
V	Volume	$[m^3]$
U_∞, V_∞	Free-steam velocity	$[ms^{-1}]$
U_τ	Skin friction velocity	$[ms^{-1}]$
V_{local}	Local effective velocity	$[ms^{-1}]$
W	Weight	[N]
y^+	Non dimensional wall unit	[-]

Greek symbols

α	Geometric angle of attack	[°]
α_{eff}	Effective angle of attack	[°]
α_i	Induced angle of attack	[°]
δ	Boundary layer thickness	[m]
ϵ	Rate of dissipation of turbulence energy	$[Jkg^{-1}s^{-1}]$
$\eta_{overall}$	Overall Efficiency	
Γ	Circulation	
γ	Specific heat capacity ratio	
q_∞	Dynamic pressure	$[Pa]$
$\Lambda_{\mathbf{LE}}$	Sweep angle at the leading edge	[°]
λ	Mean free path	[m]
μ	Dynamic viscosity	$[Pa \cdot s]$
μ_{ref}	Reference viscosity at temperature T_{ref}	$[Pa \cdot s]$
ω	Specific turbulence dissipation	$[s^{-1}]$
$\omega(y)$	Local downwash associated to a specific span-wise position	
ρ	Density	$[kgm^{-3}]$
τ_{ij}	Viscous stress	[Pa]
τ_w	Wall shear stress	[Pa]

Abbreviations

AEV	Aero-levitation Electric Vehicle
AIAA	American Institute of Aeronautics and Astronautics
AR	Aspect Ratio
ATAG	Air Transport Action Group
BOI	Body of Influence
BWB	Blended Wing body
CFD	Computational Fluid Dynamics
CRM	Common Research Model
DLR	Deutsches Zentrum für Luft- und Raumfahrt
DNS	Direct numerical Simulation
DPW2	Drag Prediction Workshop
ETOPS	Extended-range twin-engine Operational Performance Standards
FV	Flying V
FPO	Future Project Office
GGCB	Green Gauss Cell Based
GGNB	Green Gauss Node based
IATA	International Air Transport Association
ICAO	International Civil Aviation Organization
IGE	In Ground Effect
KBE	Knowledge Based Engineering
KIAS	Knots-Indicated Air Speed
LES	Large Eddy Simulation
LSCB	Least Squares Cell Based
MGC	Mean Geometric Chord
MUCL	Monotonic Upwind Scheme for Conservation Laws
NACA	National Advisory Committee for Aeronautics
N-S	Navier Stokes
OEI	One Engine Idle
OGE	Out of Ground Effect
PISO	Pressure Implicit with Split Operator
PDE	Partial Differential Equation
QUICK	Quadratic Upstream Interpolation for Convective Kinematics
RANS	Reynold's Averaged Navier-Stokes (equations)
RSME	Root Mean Square Error
SA	Spalart Allmaras
SIMPLE	Semi-Implicit Method for Pressure Linked Equations
SIMPLEC	Semi-Implicit Method for Pressure Linked Equations- Consistent
SSFT	Sub-Scale Flight Testing
SST	Shear Stress Transport
SU2	Stanford University 2
TFN	Through Flow Nacelle
WIG	Wing In Ground Effect

1

Introduction

According to the estimates presented by the International Civil Aviation Organization (ICAO), 2018 saw an increment of 6.1% in the total number of passengers that were transported via air as compared to 2017 [39]. By extrapolating these current trends, the International Air Transport Association (IATA), in its 20 year Air Passenger Forecast predicts a doubling of the total number of passengers traveling by air from 4.3 billion in 2018 to about 8.2 billion passengers in the year 2037 [61]. Many factors such as trade liberalization and visa approvals contribute to this increase. This increase in the number of air passengers equates to an enormous strain on the global aviation fuel demand. In 2018, the airline industry spent over $188 billion dollars on aviation fuel [38]. Now, given that the slump in global fuel prices has ended and an increase in fuel prices has been forecast over the years to come from about $70/barrel to over $100/barrel, this amount could increase drastically [72] . In the long term, airline companies will have to deal with not just the increase in fuel prices but also an increase in the number of passengers traveling. This would in turn require a significant increase in air traffic with estimates showing an increase of 37% in the number of flying aircrafts from 26,307 in the current global aircraft fleet to about 37,978 by the year 2028 [17].

These statistics are important to better understand the impact that global commercial aviation has on the environment. The Air Transport Action Group (ATAG) stated that as of 2018, nearly 895 million tonnes of carbon dioxide (CO_2) was released into the atmosphere by flights all over the world [10]. Although there is an increase in emission, the average fuel burnt per passenger has considerably reduced over the years because of the introduction of more fuel efficient engines, aircrafts and changes in operational practice. In fact the commercial aviation sector is 80% more fuel efficient per passenger kilometer as compared to the jets that flew in the 1960s.

However trends have increasingly shown that the rate of these technological improvements will not suffice to stabilize the negative impact of the growing air traffic.The ICAO projects a nearly 300-700% increase in CO_2 emissions by the year 2050 [39]. Developing sustainable bio-fuels or switching to electric power offer a good alternative but these improvements are currently expensive to manufacture and implement. Battery units too, that are used today are heavy and cannot be used as a single power source for an aircraft. Over the past decade improvements in aircraft design have been limited to an increase just under 10% efficiency by way of reducing wing tip vortices via optimized winglet designs and improved engine performance. The relaxation of the Extended-range Twin-engine Operational Performance Standards (ETOPS) regulations that limited twin engine aircrafts from flying trans-Atlantic distances has allowed the phasing out of four-engine aircrafts and is seen as the largest change made to modern long range commercial jets. The typical blueprint of commercial aircraft that consists of a tubular fuselage, wings and vertical tail has remained relatively constant with little or no change in the past few decades.

This tubular fuselage accounts for nearly 30%-50% of an aircrafts total zero-lift drag [69]. More drag equates to more thrust that is required to maintain a particular speed. This cylindrical fuselage as such remains a primary reason for the loss in fuel efficiency of modern conventional aircrafts. Given these facts, a major change in aircraft design is the need of the hour- a design that offers less drag, considerable improvement in fuel efficiency while still being able to offer similar passenger capacity as compared to today's conventional aircrafts.

1.1. Unconventional Aircraft Design

The various external influences that can affect the commercial aviation industry (some of which have been addressed above) and the future has always served as an impetus for aerospace/ aeronautical engineers and researchers to constantly conceptualize, innovate and manufacture aircraft that achieve a certain performance improvement such as drag reduction, increased useful load, reduced runway distance required and/or multiple combinations [44].

Over the years, a number of different unconventional aircraft designs have been showcased such as the 'Bird of Prey' concept developed by Airbus which employs bio-mimicry and incorporates features from the tail and wing of a bird. Similarly, many other concepts as shown in figure 1.1 such as the Prandtl Plane air freighter developed by the University of Pisa, the Blended Wing Body (BWB) concept called the X-48C developed by Boeing and the D8 Double Bubble developed by Aurora Flight Sciences are being studied and have garnered a lot of attention.

(a) Prandtl Plane Air Freighter[4]

(b) Aurora D8 Double Bubble[33]

(c) Boeing X-48C[66]

Figure 1.1: Examples of unconventional aircraft designs

Among the many different alternatives to a 'conventional aircraft' that have been conceptualized over the years, the idea of a true flying wing has long been on the minds of designers throughout the 20th century [73]. A flying wing as the name suggests, is an aircraft that does not consist of a tail or a cylindrical fuselage. This contributes to a significant reduction in the total wetted area leading to a loss in the skin friction drag which allows it to be more fuel efficient. Additionally, since the engines can be placed above the wing and the design doesn't require the use of complicated high lift devices, the flying wing offers to be a much quieter aircraft [23].

When it comes to aerodynamic performance, the flying wing provides an increment in the lift to drag ratio. The chord lengths associated with the flying wing are almost twice as large as the chord length of a conventional aircraft's wing. As a result of this larger length, the Reynolds number(Re) of the flow over the wings of the flying wing is much higher. Since a pure flying wing doesn't use a vertical tail and/or horizontal stabilizers, the associated induced drag and friction is nullified. Studies estimate an increase of nearly 20% in the lift to drag ratio of the flying wing configuration when compared with a conventional aircraft at similar flight conditions[15].

Calculations made by Northrop [58] show that the minimum parasite drag[1] of a flying wing as compared to a conventional aircraft is anywhere between 50% to 77% lesser depending on whether cruise or landing conditions govern. Based on the Breguet range formula as shown in equation 1.1, the maximum range is obtained when parasite drag is equal to induced drag. Northrop showed that for a specific cruise speed,

[1] Parasite drag is caused by moving any solid object through a fluid medium. The atmosphere is considered as the fluid medium in case of aircrafts

the flying wing requires about 11% - 25% less power and will fly about 13% to 33% further as compared to conventional aircrafts using the same amount of fuel.

$$Range = \frac{h}{g}\frac{L}{D}\eta_{\text{overall}} ln \frac{W_{\text{initial}}}{W_{\text{final}}} \tag{1.1}$$

where,

$$\eta_{\text{overall}} = \frac{TU_{\infty}}{\dot{m}_f h} \tag{1.2}$$

For level, unaccelerated flight, the thrust required is given by the sum of parasite drag and induced drag as shown in equation 1.3,

$$T = q_{\infty} S C_{D,0} + q_{\infty} S \frac{C_L^2}{\pi ARe} \tag{1.3}$$

Intuitively because of the absence of a cylindrical fuselage, the entire surface of the flying wing is contributing to lift generation. The flying wing possesses a high thickness to chord ratio allowing all the passengers and cargo to be housed within the cavity of its wings. This larger thickness to chord ratio at the center of the aircraft reduces the aerodynamic forces that act on the outer wings. Additionally a lower lift coefficient is required to produce an elliptical span-wise load distribution [68]. The inherent design of the flying wing reduces the effects of shock waves and the presence of subsonic flow behind the shock, thus allocating appropriate and ample space for the installation of engines. Its ability to place engines on its upper surface functions to drastically reduce forward radiated fan noise and engine exhaust noise that otherwise reflects off the lower surface of an aircrafts wing. The flying wing is expected to have reductions ranging between 4dB and 26.6 dB in the estimated perceived noise levels in comparison to the Boeing 787 and Airbus A380 [62][78].

Although getting rid of the fuselage, vertical tail and elevators has its own advantages, their absence also brings about its own set of disadvantages that flying wing designs need to consider and overcome. For instance:

- The shorter length of the flying wing can cause a change in the moment of the force from static stability to static instability[21].
- The flying wing has also shown to have a non-linear increase in lift and a non-linear change in the pitching moment at lower angles of attack [87]. This non-linearity arises as a result of flow separation on the upper surface of the wing which causes the aerodynamic center to move forward , clearly implying that the flying wing concept faces issues with regard to its longitudinal stability.
- This pitching moment cannot be accounted for by the flying wing through trim as it does not consist of a tail-elevator assembly as is the case for conventional aircrafts. It is for this same reason that high lift devices such as flaps cannot be used.
- Intuitively, this means that the maximum lift coefficient of a flying wing will only be obtained at very high angles of attack but yet lower in magnitude when compared to the maximum lift coefficient of today's conventional aircrafts.

In order to obtain longitudinal stability and for the purposes of trim, the flying wing makes use of control surfaces which are positioned on the trailing edge. The extent of control that is provided by these control surfaces depend on their size and position along the wing. Care must also be taken to ensure that flow separation at high angles of attack does not impact the effectiveness of the control surfaces.

Taking into account the need for an unconventional aircraft along with the various advantages and disadvantages that the flying wing design offers, the Flying V (FV) concept was introduced and designed with the potential of being the future of commercial aviation. Various characteristics of the Flying V related to its design, aerodynamics, structure, propulsion and control have already been studied and is also currently on going further research and development.

1.2. Thesis Outline

In this thesis, the literature research into all previous studies on the Flying V along with an in depth explanation of ground effect , its causes and it's influence on the aerodynamic performance of airfoils, wings, aircrafts and wings in ground effect (WIG) is provided in chapter 2.A detailed description of the computational domain that was created to simulate flow over the FV and the boundary conditions that were applied are given in chapter 3. Also included in this chapter is the Reynolds and Mach number scaling that was done to simulate the flow phenomena that the full scale model of the FV would experience on the scaled model. This chapter also explains the meshing strategy that was adopted to efficiently carry out a parametric study while still being able to accurately capture the forces and flow phenomena. To conduct CFD simulations, knowledge of the main governing equations of fluid flow and the different methodologies available is extremely important. This is included in chapter 4. Additionally, to model turbulence in a CFD simulation, different turbulence models, each with their own advantages and disadvantages exist. Results obtained after conducting a validation study to determine the best turbulence model to be used are also documented in this chapter. Chapter 4 also consists of the results obtained from a domain sensitivity and a grid dependence study. These studies were conducted to ensure that the boundary conditions and the refinement of the mesh bear little to no influence on the solutions obtained from the simulations. In 5 the results obtained based on the parametric study carried out by varying the FV at different heights from the ground at different angles of attack along with explanations for the same are presented. Finally conclusions made and recommendations for further understanding the behavior of the FV in ground effect are provided in 6.

2

State of the Art

This chapter attempts to provide a general review of past research into the development of the Flying V, the fundamentals of ground effect aerodynamics and past studies of different aircraft and wings in ground effect. A good understanding of past research and rudiments will help in developing the problem statement along with the research objectives to facilitate a good assessment and interpretation of the results obtained.

2.1. Flying V

As previously mentioned, the initial design of the FV was conceptualized by J. Benad in tandem with the Airbus Future Projects Office in Hamburg Germany. The FV was designed to have an elliptical lift distribution as shown in figure 2.1a with its neutral point [1] positioned behind the center of gravity in order to achieve longitudinal stability. Benad showed that through optimization, the FV had a 10% overall improvement in the lift-to-drag ratio as seen in figure 2.1b for different angles of attack as compared to the Airbus A350-900, which was chosen as the reference aircraft to be compared with the FV [14].

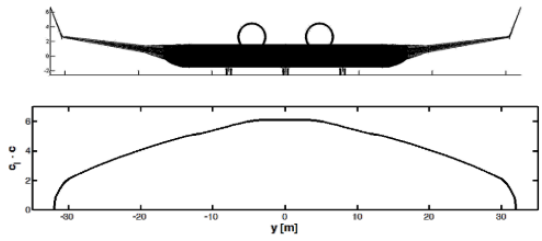

(a) Elliptical lift distribution of the FV

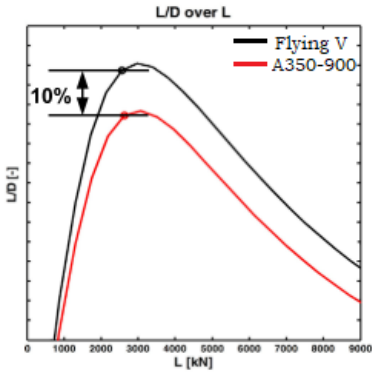

(b) Lift/drag ratio fo the FV compared to the A350-900

Figure 2.1: Preliminary results of the FV obtained by Benad [14]

Benad also estimated the mass of the FV by scaling down different aircraft parts. For instance to measure the mass of the pressurized cabin, the A320 fuselage was scaled into sections and extra mass was added to compensate for the shape of the cabins of the FV which are elliptical as compared to being circular as for the A320. During take off and landing Benad estimated that the maximum angle of attack of the FV is equal to 12.5°. Faggiano [27] used a very specific aerodynamic design approach while optimizing the design of the FV that Benad first proposed in 2015 [14]. The approach consisted of broadly dividing the FV into its main components- the main wing and two fins, treating them separately. This approach was implemented on ParaPy which is a Knowledge Based Engineering (KBE) platform that allows the user to create and modify geometry using Python code unlike software such as CAD which requires constant user intervention. It

[1] Neutral point refers to the position at which an aircraft is neither stable nor unstable i.e. CG is neutrally stable

also consists of tools like the "Salome Meshing tool" that automatically creates grids from 3D geometry and exports it to different flow solvers. Now, based on different variables - 10 wing plan-form, 43 profile and 3 fin, two separate approaches on ParaPy were tested - a single and dual step optimization procedure, where plan-form and airfoil parameters were varied successively and simultaneously [27]. Using an Euler Solver and the vortex lattice method, a feasible model was first generated and then by using the SU2 (Stanford university solver) Euler optimization, a design for minimum cruise drag was obtained. In cruise condition, the flow can be assumed to be in-viscid and so the Euler equations were solved instead of the Navier Stokes (N-S) Equations as the former is computationally much cheaper. The geometry of the FV was then modified and optimized based on a specific set of cruise conditions as shown in Table 2.1.

Table 2.1: Cruise conditions used to optimize the FV's geometry in Faggiano's investigation [27]

Parameter	**Value**
C_L	0.26
M	0.85
P_{cruise}	1650.38 Pa
T_{cruise}	216.65 K
ρ_{cruise}	0.27 kgm^{-3}

Under similar conditions, the initial baseline design gave lift to drag (L/D) ratios equal to 20.04, which was similar to that of the NASA CRM. After optimization, Faggiano was able to obtain a 25% improvement in the L/D ratio over the NASA CRM model. This optimization which consisted of sweeping back the outer wing from 15° to 30° and twisting it downwards, along with a decrease in the wing area to 883m^2 also resulted in a 50% reduction of the pitching moment coefficient and a reduction in the wave, vortex and profile drag. This change in wing plan-form shape is shown in Figure 2.2. Although this optimization resulted in a 10m increase in the length of each wing, it was also shown that the overall size of the FV was still smaller than that of the reference aircraft as seen in Figure 2.2. It must be noted that both of these investigations conducted by Benad [14] and Faggiano[27]considered only an isolated air-frame.

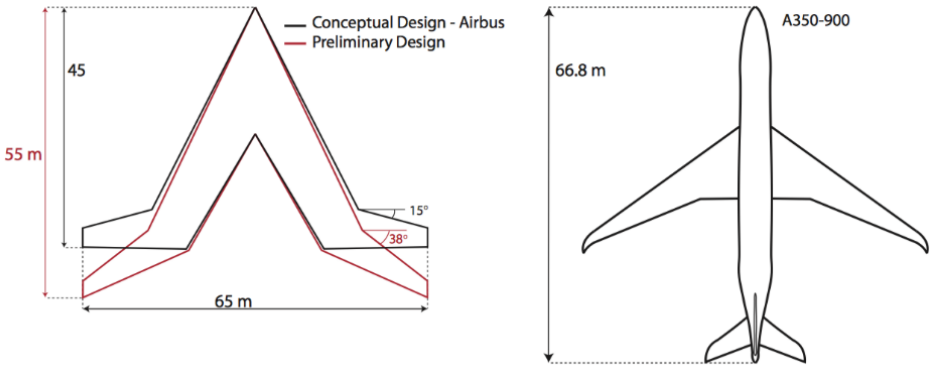

Figure 2.2: Difference in initial and optimized FV plan-form and its comparison with that of the A350-900 [27]

Benad [14] used handbook methods to estimate the structural weight of the FV. However, the accuracy of these handbook methods for such unconventional configurations cannot be trusted completely. It is for this reason, van der Schaft [77] analyzed the structural concept of the FV and gave an estimation of its mass characteristics. In this study, the fuselage was integrated into the wing cavity by way of an oval skeleton which consisted of multiple arcs with a fixed radius that was supported by structural elements used to carry the resultant forces created by the differences of the internal bending moment. This is very different as compared to the dual-tube concept introduced by Benad[14] but still maintains the same design philosophy of having a cavity that is volumetrically efficient with better airfoil shaping parameters and one that allows for a more spacious cabin layout.

The optimized fuselage shown in Figure 2.3 was separated into three main sections namely the streamwise oriented nose section, a main section and a tapered section. All of these sections are positioned parallel to the leading edge. Between the nose and the main section a transition structure is created that also acts

(a) Top View

(b) Isometric View

Figure 2.3: Optimized structural results obtained by van der Schaft's study[77]

as a wing carry-through structure. A similar transition structure is put to use between the main and tapered sections which creates a smooth transformation from the fuselage section to the main wing section.

Palermo[59] in 2019 studied the static longitudinal stability and control characteristics of the FV. Through experimental investigations an optimal center of gravity location was defined and then a parametric study was performed, where the influence of the location of the center of gravity on flight performance using either the limited or complete amount of the pitching moment control authority was studied. The results obtained from the experimental campaign were validated with those from CFD simulations. To create the scaled model of the FV, the Froude scaling laws were used [86]. To accurately size the different control surfaces located on the trailing edge at the back, along the central and outer trunks of the FV, a horizontal tail volume comparable to that of the reference A350-900 aircraft was used. These control surfaces play a crucial role in providing longitudinal and lateral stability for the FV. Figure 2.4 shows the top view of the control surface characteristics along the FV plan-form.

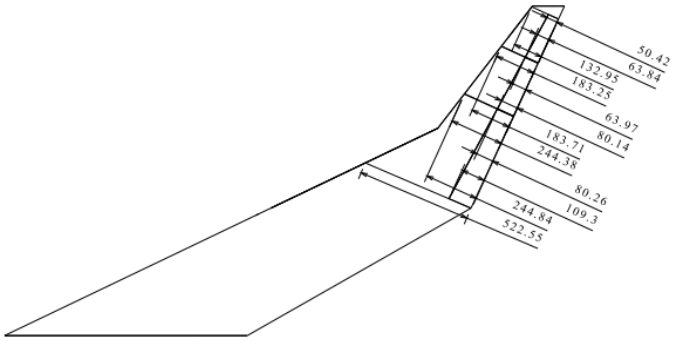

Figure 2.4: Dimensions of the control surfaces across the FV plan-form [59]

To perform the CFD simulations, the Spalart-Allmaras (SA) model was used to solve the Navier-Stokes (NS) equations. A hybrid mesh was generated that consisted of 40 inflation layers from the surface of the aircraft with a first cell height of $5 \cdot 10^{-6}$ meters to achieve an average $y^+ < 1$. Three grids were generated - the first consisting of tetrahedrons and wedges, the second consisting of polyhedrons and the third being a refined version of the second grid.

The experimental results showed that the control surfaces do not go through any significant loss in efficiency for the whole range of tested angles of attack and as a result there was no deep-stall behavior observed. The aerodynamic center when the control surfaces are not deployed was calculated to be 1.42 metres away from the nose of the FV in the longitudinal direction. Similarly, the center of gravity was found to be located 1.336 metres away from the nose of the FV. At this location, a maximum lift coefficient of 0.7 can be obtained. It was also concluded that the initial design used for the wind tunnel model's control surfaces help further reduce the landing speed by way of trimming the FV at higher angles of attack which is why it can also be used for the future Sub-Scale Flight Testing (SSFT) model. Numerical results obtained through CFD show much larger differences of the drag and pitching moment characteristics with experimental results. Using the λ_2 criterion, the behavior of the different vortical structures produced across the wing at different angles

of attack were visualized. A more detailed explanation of each of these vortical structures is provided in the report [59].

All of the results obtained from these studies- [14, 27, 59, 77], except the mass estimation, were mainly based on an isolated air-frame. The presence of an engine and nacelle on the upper surface of the air-frame would significantly affect the aerodynamics. This is why, Pascual [70] was tasked with optimizing the position of the FV's propulsion system, one that would minimize the negative interferences between the air-frame and the engine. A two-step approach was followed based on a latin hyper-cube sampling strategy. The design space consisted of 30 points where the influence of the engine position was studied. The two most extreme positions to analyze the influence of the engine orientation on the aerodynamic performance of the FV was then analyzed. Now when it comes to the engines being simulated to study the aerodynamics of the FV, they could be used as through-flow-nacelles (TFN) or as an actual engine that sucks in air to produce thrust. The latter was chosen when running every simulation as a TFN configuration would not be able to accurately simulate the flow behavior around a fully powered engine. Based on the results, an appropriate position for the engines to have the least aerodynamic interference was recommended. A schematic of this is shown in Figure 2.5.

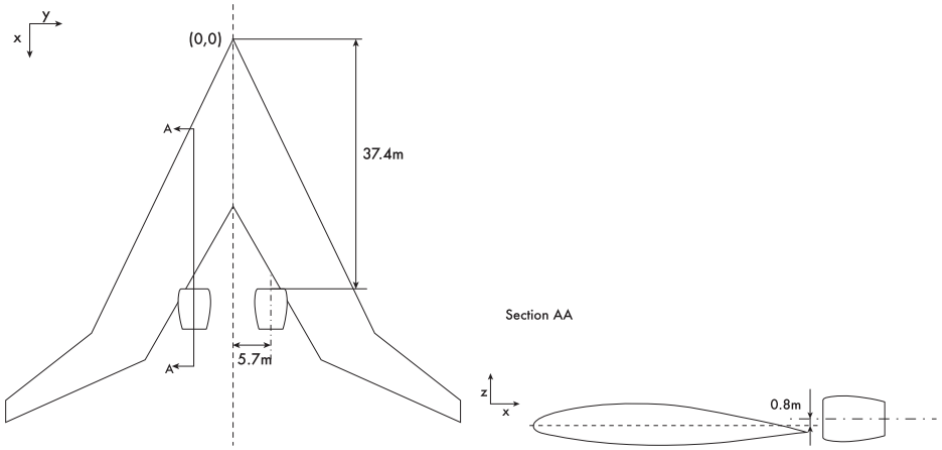

Figure 2.5: Optimized Engine Position on the FV [14]

This position was determined by also taking into consideration the structural limits and stability of the FV. The results obtained by Pascual showed that in comparison to the ideal integrated positions of the engines as in Figure 2.5, if the engines were placed very close to the symmetry plane or towards the center of the aircraft, there would be a large reduction in the lift to drag ratio with losses reaching as high as 55%. Additionally, this recommended location of the engines showed a 10% improvement in lift to drag ratio as compared to the initial design offered by Benad [14] in 2015. What needs to be understood is that this investigation only suggests an optimal location for the engines to be placed on the FV, but apart from finding an optimal intake geometry for the lip on the NASA CRM engine, no new design for an engine has yet been provided.

2.1.1. Physical Model

The geometry used throughout this project is a 4.6% geometrically scaled model of the Flying V. For computational efficiency, only the half model of the FV will be employed in the simulations, capitalizing on the symmetry of the model. The different plan-form characteristics of this model are shown in Figure 2.6 below. The total wingspan is equal to 2.99 meters with an overall length of 2.5 meters. The dashed line in the figure represents the mean geometric chord (MGC) of the FV, which has a length of 0.821 meters. The center of gravity (CG) of the FV which is also presented in Figure 2.6 is located at a point 1.33 meters away from the origin.

As reported by Palermo [59] the leading edge sweep is equal to about 64.4° after which it reduces to 37.8° till the tip of the wing. The outer wing is characterized by −4.3° of twist. The chord lengths at different span-wise sections are shown in Table 2.2 along with the corresponding sweep angles between each section measured from the leading edge.

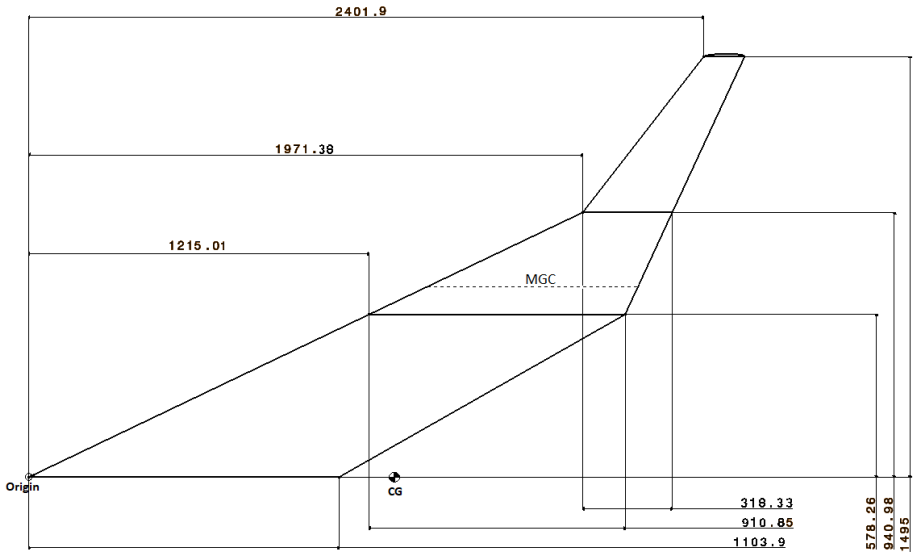

Figure 2.6: Plan-form top view of the Flying V model using for this investigation (Dimensions in mm) [59]

Table 2.2: Plan-form characteristics of the FV

Section	**c** [meters]	Λ_{LE}
1	1.104	64.4
2	0.910	64.4
3	0.318	37.8
4	0.145	37.8
$\bar{c}$	0.821	64.4

For the remainder of this thesis, all of the length scales are non-dimensionalized using the wing-span b and the forces are non-dimensionalized using a reference chord length of $\bar{c} = 0.8204$m and a reference area equal to $S_{\text{ref}} = 0.9345\text{m}^2$.

2.2. Ground Effect

In order to fully understand the concept of ground effect, an accurate definition of the decomposition of the aerodynamic force acting on a wing into its components is required. As seen in figure 2.7, the lift component acts in a direction normal to that of the free-stream and the component of drag acts in a direction that is parallel to the free-stream. During a flight, a wing produces lift due to a pressure differential between its upper(suction side) and lower (pressure side) surfaces [7].

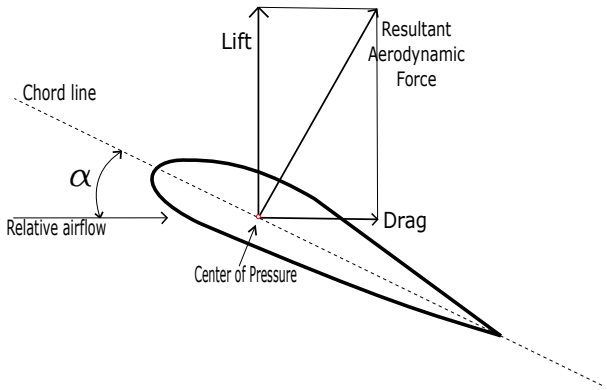

Figure 2.7: Cross section of a wing depicting the components of aerodynamic force

2.2.1. Downwash

In nature, an equilibrium must always exist and so a fluid will always flow from a region of higher pressure to a region of lower pressure. In case of the wing, high pressure air leaking over to the suction side at the wingtips, creates tip vortices as seen in Figure 2.8a . These vortices are counter rotating and cause air on the top to move towards the center and air at the bottom to move away from the center.

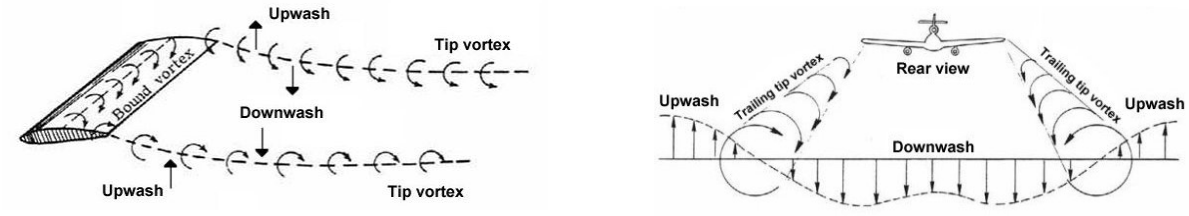

(a) Tip vortex and bound vortex/vortex filament over the entire span of a finite wing

(b) Downwash Distribution across the wingspan

Figure 2.8: An illustration of the tip vortices produced and the downwash distribution across an aircrafts wing [29]

For a finite wing, a vortex filament is said to exist in the span-wise direction. Based on Helmholtz theorem [35], this vortex filament will stay continuous as long as it is on a surface or in a loop. A visualization of this loop is given in Figure 2.8a. If this vortex filament has a circulation $\vec{\Gamma}$, such that $\vec{\Gamma}$ acts along the length of the filament in a direction that is defined by the right hand rule, the tip vortices will also have a circulation $\vec{\Gamma}$. Due to this circulation, these vortices have a higher downwash that slowly reduces towards the center of the wing, creating a span-wise downwash distribution as shown in Figure 2.8b. This span wise change in downwash causes a change in the lift produced over the wing.

The airfoil shown in Figure 2.9 has a geometric angle of attack α. Due to the local downwash $\omega(y)$, the free-stream velocity V_∞ acts on the airfoil in terms of a local effective velocity, V_{local}. The angle between V_∞ and V_{local} is called the induced angle of attack, α_{i} as shown in figure 2.9a).

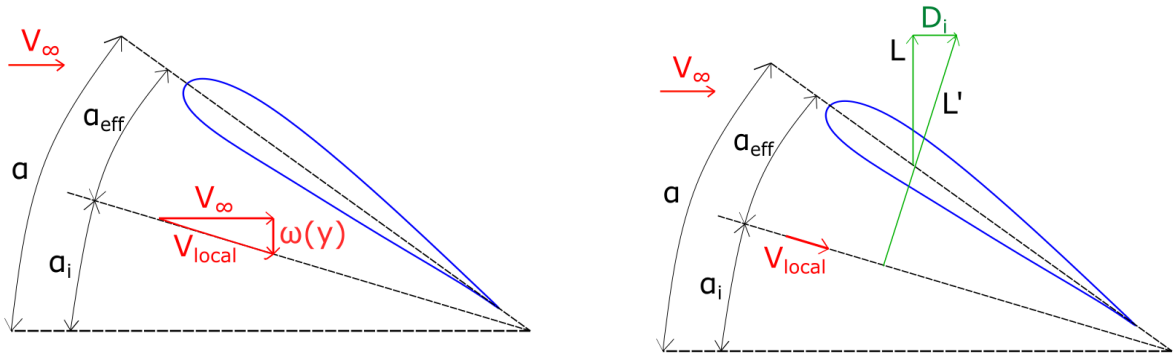

(a) Difference between α_{eff} and α

(b) Induced drag

Figure 2.9: Illustration of the effects of downwash

Essentially, the effective angle of attack that is created due to downwash is given by,

$$\alpha_{\text{eff}} = \alpha - \alpha_{\text{i}} \tag{2.1}$$

It is defined as that part of the geometric angle of attack that lies between the local chord of a wing and the effective airflow, V_{local}. The strength of the vortices determine the increase or decrease of the effective angle of attack. Since $\alpha_{\text{eff}} < \alpha$, the amount of lift generated over a given section of the wing is reduced. If L is the lift vector that is perpendicular to the free-stream V_∞ and L' is the the lift vector corresponding to V_{local}, the shift in the lift vector from L to L' as shown in figure 2.9b will contribute to the total drag of the wing. This contribution due to the rearward tilt of the lift vector as a result of downwash is called the induced drag D_{i}.

Now, when a wing is close to the ground, the downwash that is created by the tips gets distorted as it interacts with the ground which prevents it from completely developing. This results in the lowering of the induced angle of attack, α_i. Consequently according to equation 2.1, the effective angle of attack, α_{eff} increases leading to a less aft tilting of the lift vector and a reduction in the induced drag ,D_i. The minimum drag however will remain the same. This change in the aerodynamics that occurs is called ground effect. This has been showcased in different experimental investigations such as [2] [16].

Depending on the kind of wing that an aircraft uses, ground effect can be classified into two categories:

- Attached flow ground effect : high aspect ratio wings as in the case of commercial and transport aircrafts
- Separated flow ground effect: delta wings as in the case of fighter aircrafts

The first of these categories, attached flow ground effect, can be further classified into chord dominated ground effect and span dominated ground effect. In case of the latter i.e. span dominated ground effect, the main influencing parameter is the height-span ratio. Abramowski [5] explains that since the induced drag of a wing is dependent on the span-wise lift distribution and varies inversely with the wing's aspect ratio, when in ground effect, an aircraft with wings that have a larger aspect ratio would experience a greater reduction in the induced drag when compared to wings with a smaller aspect ratio. In case of chord dominated ground effect, the main influencing parameter is the height-chord ratio. From the perspective of total pressure, the additional lift experienced by a WIG is because of a rise in static pressure on its suction side with the ground. The total pressure of a flow field, which is equal to the sum of the static and dynamic pressures, must always remain constant throughout. When a wing flies in close proximity to the ground, the flow is forced to travel between the wing and the ground where an air cushion is created because of a decrease in dynamic pressure and a subsequent increase in static pressure [36]. This increase in static pressure is known as 'ram pressure' and in certain instances can cause the air beneath the wing to stagnate resulting in the highest possible coefficient of pressure ≈ 1. It is further explained that chord dominated ground effect does not necessarily always contribute to lift. Depending on if the under side of a wing is convex and if the angle of incidence is very low or even negative, a 'venturi nozzle' can be created resulting in high speed low pressure air sucking the wing down.

Additionally, depending on the kind of application, ground effect can be classified into

- Static Ground Effect (SGE): where the flying altitude does not vary with time.
- Dynamic Ground Effect (DGE): where the flying altitude continuously varies with time. For example, an aircraft taking off or in final approach onto a runway.
- Mutational Ground Effect (MGE): where there exists an abrupt change in flying altitude. For example, landing and take-off maneuvers on aircraft carriers.

Gudmundsson [34] in the book titled General Aviation Aircraft Design explains that an aircraft will begin to experience changes in its aerodynamic characteristics at a height that is equal to almost two wingspans from the ground. However it is further stated that these changes are negligible at that height and it is reasonable to consider the influence of ground effect when an aircraft is about one wingspan from the ground. As an aircraft continues to get closer to the ground the amount of ground effect that its wing experiences also increases.

2.2.2. Previous studies of wings in ground effect

The phenomenon of ground effect has long been studied since the early 20th century by physicists like Albert Betz and Wieselberger [85]. McCormick [50] in a similar approach estimated the change in induced drag by making use of the theory of reflection. A horseshoe vortex was used to replace a rectangular wing which was reflected such that the resulting vertical velocities were equal to zero along the reflection plane for each image. The influence of ground proximity on the downwash of the wing using Biot Savarts law was futher studied, and a induced drag factor ϕ was developed. It related the induced drag experienced IGE and OGE as shown below in equation 2.2 [50]:

$$\phi = \frac{C_{D_i}(IGE)}{C_{D_i}(OGE)} = \frac{(16 \cdot h/b)}{1 + (16 \cdot h/b)^2} \tag{2.2}$$

In case of an elliptical lift distribution similar to that of the FV, Asselin [9] estimated the ground influence coefficient to be calculated as:

$$\phi = 1 - \frac{2}{\pi^2} ln(1 + \frac{\pi}{8 \cdot h/b}) \tag{2.3}$$

Majority of past ground effect investigations have been based on whether 2-D chord dominated ground effect or 3D span dominated ground effect is being studied. In case of chord dominated ground effect, airfoils at low to moderate angles of attack have been extensively studied. Hsuin and Chen [37] conducted numerical simulations to study the influence of camber and thickness on the aerodynamics and performance of a 2D airfoil in ground effect. An important takeaway from this study was that the forces acting on the airfoil were found to be dependent on the passage of flow between the airfoil and the ground.

Qu et al [64] a numerically investigated the flow physics of a National Advisory Committee for Aeronautics (NACA) 4412 airfoil in ground effect for a range of angles of attack (−4° to 20°) and ride heights. At lower angles of attack, the blocking effect arises resulting in an increase in pressure in the region between the airfoil and the ground. At higher angles of attack they observed that the separation point continuously shifted its location gradually towards the leading edge as the ride height was reduced. Additionally, because of an increase in the adverse pressure gradient along the chordwise direction a larger separated flow is observed on the upper surface of the airfoil. This large separation is responsible for an increment in negative lift as the pressure on the upper surface increases to values greater than on the lower surface.

Abramowski[5] studied the flow over a NACA/Munk M15 airfoil. A 40 % increase in the lift coefficient over the same in unbounded flow was observed. The potential of WIG crafts was highlighted and also an empirical formula for conducting preliminary calculations of chord dominated ground effect as shown in equation 2.4 was presented.

$$C_{L,\text{ground}} = C_L \left(\frac{h}{c}\right)^{-0.11} \tag{2.4}$$

Mahon and Zhang [49] conducted an experimental campaign followed by numerical investigations to study the negative lift (down force) created by a Tyrrel-02 airfoil. It was observed that with a decrease in height the down force continued to increase up to a peak value after which a dramatic reduction was obtained. This was explained to be because of the previously mentioned Venturi effect created by the presence of a convergent divergent 'nozzle' between the lower surface of the airfoil and the ground. Although an increase in α_{eff} occurs, the impact of the Venturi effect is greater and lift is made negative.

In case of 3D span dominated ground effect, the trajectories of tip vortices and the flow aerodynamics have been of primary interest.

Moon et al [52] studied the impact of aspect ratio on the aerodynamics of a 3D wing of an Aero-levitation Electric Vehicle (AEV) in ground effect. The efficiency of the wing i.e. its lift-to-drag ratio was shown to gradually reduce with a reducing span as a result of an arch vortex that was created between the horizontal and vertical wings of the vehicle.

Deng[20] conducted numerical studies to highlight the differences in aerodynamic behavior of the DLR F6 wing-body both in unbounded flow and in ground effect. The lift, drag and moment coefficients for the wing and fuselage were analyzed separately. Results showed that the lift gain on the wing was much larger than the drag change on the fuselage. While on the contrary, the pitching moment generated on the fuselage was larger than that of the wing. The shape of the separation bubble that is produced at the wing root trailing edge section remained relatively unchanged, however, the size of the separated area showed some dissimilarities as seen in figure 2.10.

Jia et al [42] studied the aerodynamic characteristics of a rectangular wing and a delta wing with the same aspect ratio (= 4) in ground effect with varying heel angles. Included in the analysis were also results of these wings with end plates and ailerons attached.

In the results it was observed that for a specific bank angle, the side of the wing closer to the ground (descending side) is greater influenced by ground effect than the side of the wing away from the ground (rising side). With end plates attached, the tip vortices were further weakened and so in proximity to the ground, the wing was less affected by these vortices and a significant increase in lift was generated as shown in figure 2.11a. Also shown in figure 2.11b is that the drag force reduces with an increase in heel angle and the end plates help to further decrease it. Since the bank angle induces an un-symmetric distribution of lift across the span of the wing, a righting moment is generated. Similarly, because of an uneven drag distribution across the wing that is higher at the rising side and lower on the descending side, an adverse yaw moment is also produced.

In case of the delta wing, ground effect was shown to be dependent on the local chord length. As such the lift force generated decreased along the span towards the tip. Compared to the rectangular wing, the righting

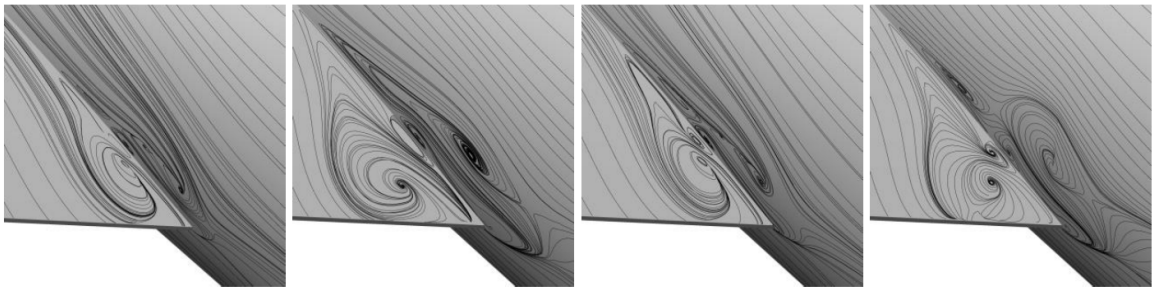

(a) OGE (b) $h/c = 1.00$ (c) $h/c = 0.50$ (d) $h/c = 0.25$

Figure 2.10: Surface streamlines on the wing fuselage section at an $\alpha = 1.23°$ [20] at different heights (non dimensionalized with the chord of the DLR F6 wing)

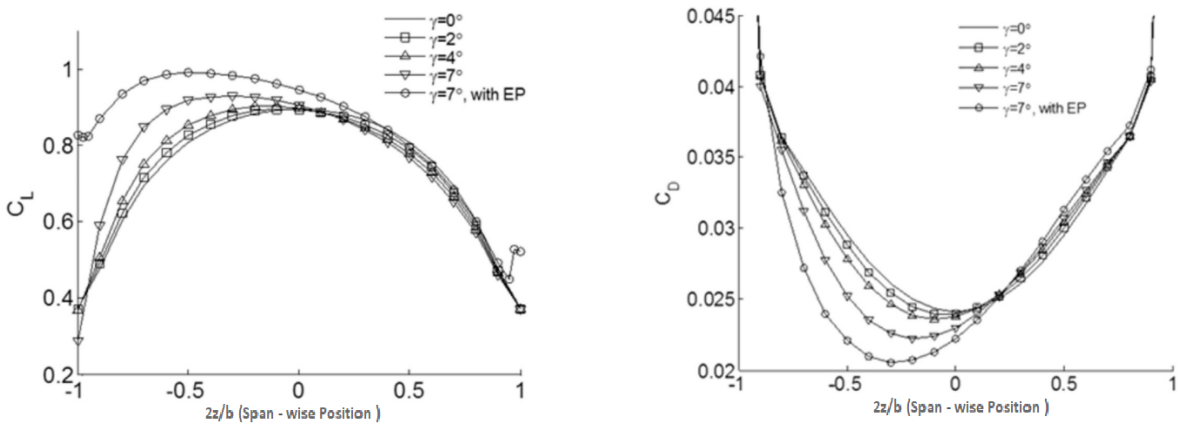

(a) Lift Coefficient Distribution

(b) Drag Coefficient Distribution

Figure 2.11: Span-wise distributions of lift and drag coefficient at h/c=0.3 and $\alpha = 6°$ [42]

and adverse yaw moments were much smaller as majority of the lift was produced along the root of the wings. This implied that lesser control was required to overcome the moments thereby displaying the advantage in maneuverability that the delta wing possessed over the rectangular wing.

Pauson Jr. and Kjelgaard [60] conducted an experimental and theoretical investigation on thick wings both in and out of ground effect to study the influence of a variety of sweep angles. A NACA 0018 constant chord, untwisted wing with a centerbody was used and tested for four leading edge sweeps of 0°,15°,30° and 45°. They observed that the aspect ratio of the wing does not greatly influence the performance of the wing when the sweep angle was increased. Another conclusion drawn from their results was that the value of the minimum coefficient of drag, C_D, increases with a reduction in the wing aspect ratio since the drag associated with the centerbody, which is otherwise constant, becomes proportionally larger relative to the drag produced by the wing. On the other hand, the opposite takes place and the magnitude of minimum C_D decreases when the sweep angle is increased because the centerbody drag would now make a smaller contribution. When longitudinal stability was considered, results showed that at very low ride heights, as the flow beneath the wing accelerates, C_L decreases and C_D increases causing a significant nose up pitching moment.

2.3. Problem Statement

In a statistical summary conducted by Boeing [71] of all commercial flights from 1959 to 2017, they discovered that final descent, landing and take-off should be considered as the most critical parts of any flight, accounting for 48 % and 13% respectively, of all accidents. These figures are significant considering that these stages of flight makeup just 6% of an aircrafts entire journey. It is therefore irrefutable that any new aircraft that is

designed must be extremely stable, maneuverable and possess good low speed performance in proximity to the ground. Conventional aircrafts use high lift devices like flaps and slats to improve stability and increase the amount of lift its wings produce at lower speeds. The FV however, has no such high lift device and solely relies on the lift produced by its wing to achieve a speed that is low enough to land safely.

2.3.1. Influence of Ground Effect on Landing

- When an aircraft descends into ground effect, which starts at a height equal to the wingspan of the aircraft [34], the decrease in downwash will give an increase in the effective angle of attack. This means that a smaller wing angle of attack will be required to maintain the same coefficient of lift. If a constant pitch attitude is maintained, the increase in lift will reduce the rate of descent and cause the aircraft to level off, in an effect known as 'floating,' which lengthens the required landing distance[18].
- Staufenbiel and Schlichting [82] studied the longitudinal stability of an airplane in ground effect. Their results showed that the decrease in induced drag will cause a reduction in deceleration, and any excess speed above the correct threshold speed could lead to a considerable float distance.
- The reduction in power required can also give the aircraft a tendency to rise above the intended descent path to the runway. This effect is called "ballooning" [82].
- If the airspeed is allowed to decay late into the final approach and the pilot attempts to arrest the ensuing increase in sink rate by raising the nose, thereby increasing the angle of attack, the wing may stall on entering ground effect resulting in a heavy landing.

2.3.2. Influence of Ground Effect on Takeoff

- The effects of climbing out of ground effect is exactly the opposite to that of entering. The lift coefficient reduces and so the wing will need an increase in the angle of attack to compensate [18]. This would mean that the drag increases and hence more power would be necessary. The increase in downwash will generally cause a nose up pitching moment requiring the pilot to pitch down.
- It is possible to become airborne in ground effect at a lower air speed and angle of attack. However, after leaving ground effect, the aircraft could sink and settle back onto the runway [82]. This makes it vital that the right speed and attitudes are used for takeoff.
- The nose up pitching moment that is expected may induce an inadvertent over rotation and cause a tail strike as well.

Based on all of these reasons which describe the effects of ground proximity on an aircrafts flight behavior, the influence of ground effect on the FV at various heights above the ground should be analyzed.

2.4. Research Question

Based on the problem statement mentioned above, the following research question was posed:

"How are the longitudinal stability, low speed performance characteristics and aerodynamic behavior of the FV affected when in ground proximity?"

The following sub-questions pertaining to the main research question were formulated:

- How is the lift and drag characteristics of the FV affected by different angles of attack at different heights from the ground ?
- By analyzing flow phenomena over the FV, can an explanation for the improvement in lift be derived.
- How does the proximity to the ground affect the pitching moment stability of the FV ?
- How does the wake of the FV and its structure develop in proximity to the ground ?

3

Numerical Methodology

This chapter describes in brief the different methodologies that were adopted to successively perform the multitude of CFD simulations for this project. Included in this chapter are sections that describe the computational domain, the different boundary conditions that were applied on each face of the domain, the fluid properties and the meshing strategy that was put to use in order to best capture the aerodynamic characteristics and flow phenomena over the half model of the FV.

3.1. Fluid Properties

The Reynolds number(Re), for an object moving through a fluid with a velocity V_∞ that has a density ρ and a dynamic viscosity μ is defined as :

$$Re = \frac{\rho U L}{\mu} \tag{3.1}$$

where L is a characteristic length of the object. The Mach number(M) is defined as the ratio of flow velocity to the local speed of sound (a).

$$M = \frac{U}{a} \tag{3.2}$$

According to dynamic similarity, if two geometrically similar objects (same shape but different size) have the same applied boundary conditions and the same Reynolds number and Mach number (M), then, regardless of the fluid properties, i.e. μ and ρ, the flow will stay 'relatively' similar.

As mentioned by Faggiano [27], the Airbus A350 is considered as the reference aircraft that the FV is compared with. Based upon a 188.240 tonne landing weight and a 'full' configuration i.e. slats at 27° and flaps at 37.5°, the lowest selectable landing speed of the A350 is about 135 Knots-Indicated Air Speed (KIAS) which is approximately 69ms^{-1} [31]. Therefore, in the context of this thesis, the assumed landing speed of the FV is also set at 69ms^{-1} $\approx M = 0.2$. An important understanding given this chosen landing speed is that as a result of the large thickness to chord ratio of the FV and its highly swept wings, air would locally accelerate over $M = 0.3$. This implies that there would be a change in density greater than 5% which would cause the flow to become locally compressible in nature. For this reason, throughout this entire thesis density is assumed to be a function of space and the **compressible RANS** equations will be solved.

Using Blasius turbulent boundary layer thickness equation (equation 3.3) where x is the characteristic length, during the mesh generation, the creation of inflation layers over the wing to resolve the turbulent boundary layer from within the viscous sub-layer is done by considering the highest Reynolds number. Based on the length of the local chord length, the highest Reynolds number of the flow is obtained at the root of the wing. The Reynolds number associated with the full scale FV is estimated to be about 108 million for a root chord length of 22.06 meters.

$$\delta \approx \frac{0.37x}{{Re_x}^{0.2}} \tag{3.3}$$

Full scale simulations are computationally very intensive. In case of a parametric study, continuously performing full scale simulations can be counter productive given the available time frame and computational

resources. In order to overcome this difficulty, the process of Reynolds and Mach number scaling can be implemented. By maintaining the geometric and dynamic similarities, these scaling laws facilitate the usage of a smaller scaled model where flow phenomena and forces expected in the case of a full scale model can be replicated and captured [47].

To simulate similar flow phenomena and forces as on the full scale model using the smaller scaled model that has a root chord length of 1.10 meters, the isentropic flow equations given by 3.4, 3.5 and 3.6 respectively, are used to obtain modified values of viscosity for a fixed Mach and Reynolds number.

$$\frac{P}{P_t} = \left(1 + \frac{\gamma - 1}{2} M^2\right)^{\frac{-\gamma}{\gamma - 1}} \tag{3.4}$$

$$\frac{T}{T_t} = \left(1 + \frac{\gamma - 1}{2} M^2\right)^{-1} \tag{3.5}$$

$$\frac{\rho}{\rho_t} = \left(1 + \frac{\gamma - 1}{2} M^2\right)^{\frac{-1}{\gamma - 1}} \tag{3.6}$$

Owing to computational limitations because of an exponential increase in the number of cells that are required to be meshed as a result of an extremely small first cell height, the Reynolds number for the scaled simulations was set at 10 million rather than at 108 million. Studies such as [41] and [54] substantiate this change by showing that the flow phenomena for streamline bodies (for example:airfoils,wings etc.) at very high Reynolds numbers ($> 10^6$) stays relatively the same. A simple MATLAB script that incorporates these equations to output the necessary fluid properties is presented in Appendix A.

The modified fluid properties that will be used for the remainder of this thesis except for the verification and validation of the different turbulent models are tabulated in table 3.1

Table 3.1: Values of different fluid properties to be used in the RANS simulation of the scaled model

Quantity	**Units**	**Value** (Full-scale Model)	**Value** (Scaled Model)
Chord length	m	22.06	1.10
Re	-	108 million	10 million
$Mach$	-	0.2	0.2
Speed of Sound	ms^{-1}	343	340.20
Velocity of Fluid	ms^{-1}	69	68.04
Temperature of Fluid	Kelvin (K)	288.15	288.15
ρ	kgm^{-3}	1.225	1.225
μ	PaS	1.716×10^{-5}	9.4830×10^{-6}

The RANS equations are solved on the assumption that fluid behaves as a continuum rather than as discrete particles. To ensure that the fluid medium represented by the altered values of different fluid properties which will be applied to perform the RANS simulations of the scaled model is still a continuum, it is imperative to also calculate the Knudsen number (Kn). The Knudsen number which is defined as the ratio of the mean free path(λ) to a representative physical length scale (L) as shown in equation 3.7.

$$Kn = \frac{\lambda}{L} \tag{3.7}$$

The value of the Kn, classifies fluid flow into different regimes [43] :

- $Kn < 0.01$: Continuum flow
- $0.01 < Kn < 0.1$: Slip flow
- $0.1 < Kn < 10$: Transitional flow
- $Kn > 10$: Free-molecular flow

The Knudsen number, in tandem with kinetic theory, can also be expressed in terms of the Mach and Reynolds number which are commonly used aerodynamic parameters as shown in equation 3.8

$$Kn = \frac{Ma}{Re}\sqrt{\frac{\gamma\pi}{2}} \tag{3.8}$$

In the above equation, γ is the heat capacity ratio defined as the ratio of heat capacity at constant pressure (C_p) to the heat capacity at constant volume (C_V). For the scaled model, the temperature of the fluid is estimated to be about $290.45K$ which corresponds to a heat capacity ratio of $\gamma = 1.4$ [3]. Substituting this along with the fixed values of Mach number (= 0.2) and Reynolds number (= 10 million), the Knudsen number is evaluated to be equal to 2.96×10^{-8}. Comparing with the different regimes stated above, it can be asserted that the fluid remains a continuum.

3.2. Computational Domain

The side view of the computational domain that was utilized to perform the CFD simulations with the FV in ground proximity is shown in figure 3.1. The origin of this domain is located at the leading edge tip of the root of the wing. Also seen within the main computational domain, in figure 3.1, is another smaller rectangular domain that has a length of $5b$ and a height of $2.66b$ measured from the origin which exists at a distance of $6.66b$ from the edge of the larger rectangular domain as shown in the figure. This smaller domain is known as a 'body of influence' (BOI) which was created in prospective of gaining more control and slowing down the refinement in the vicinity of the wing. The BOI is extruded to a distance of about $5b$ while on the other hand the larger 2D domain is extruded to a distance that is equal to the length of the upper plane from the origin. The appropriate distance at which these planes must be set so as to not interfere or influence the simulation results is mentioned in section 4.2 where the results from a domain sensitivity test have been presented. This extrusion will result in the formation of a 3D domain in the shape of a cuboid consisting of 6 boundary faces namely: an inlet plane, an outlet plane, a symmetry plane, an upper plane, a side plane and a ground plane. The inlet plane is located at a distance of $6.66b$ from the origin while the outlet plane is located at a distance of $40b$ from the inlet plane.

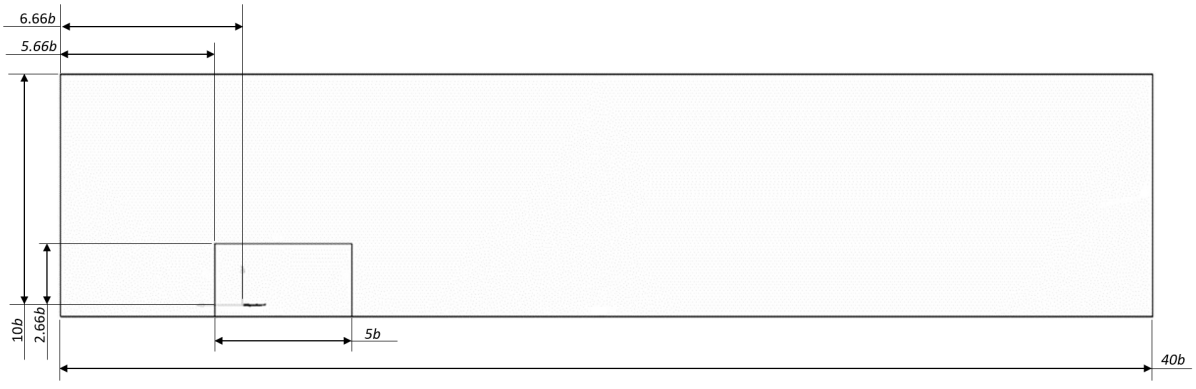

Figure 3.1: Computational domain used to study the influence of ground effect

The 3D geometry that was created by Palermo[59] for his study on the longitudinal static stability of the FV scaled model is used for this thesis. Owing to symmetry and to facilitate a faster convergence, only the half model of the FV was used.

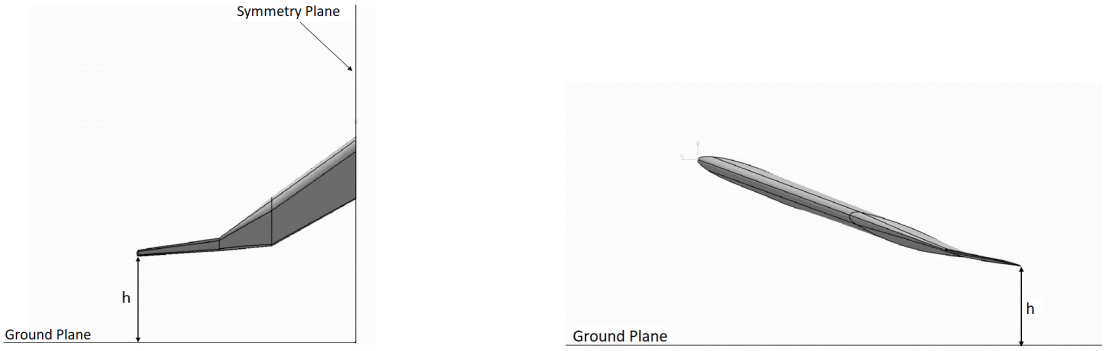

(a) Front View

(b) Side View

Figure 3.2: Illustration of how the ride height of the Flying V is measured from the ground

Now since this thesis is based on the influence of ground proximity on the FV's performance. It is crucial to accurately measure the height of the FV from the ground. A number of different reference positions such as the origin, the quarter chord point and the CG were considered to be selected as reference points to specify a height from the ground while varying the angle of attack. However, it was observed that for each of these locations at the lowest ride height and at higher angles of attack, the wing geometry would intersect through the ground plane. In order to prevent this from happening the trailing edge tip of the wing was chosen as the reference point on the FV from which the height to the ground is measured. Figures 3.2a and 3.2b provides an illustration how the height from the ground to this point is measured.

As mentioned in section 2.2.2, an aircraft truly begins to experience the effects of ground proximity at a height equal to half its wing span. Based on this, the ride heights considered for this study have been were varied between $0.0769b$ and $0.5b$. The heights corresponding to different scales of the FV are also tabulated in table 3.2.

Table 3.2: Specification of ride heights considered for this study along with the height corresponding to the full scale of the FV

Non-dimensional height (-)	**4.6 % Scaled model** (meters)	**1:1 Scale model** (meters)
$0.0769b$	0.23	5
$0.15b$	0.45	9.75
$0.25b$	0.74	16.25
$0.5b$	1.49	32.5

3.3. Meshing Strategy

Now that the required boundary conditions and computational domain is understood and set, this domain needs to be divided into many small elements called cells. In each of these cells, the discretized conservation equations are solved so that flow variables such as pressure and velocity can be calculated throughout the computational domain. In finite volume methods, this division of the domain into cell volumes is called mesh generation. In any CFD simulation, the results obtained are considered accurate and valid if a good quality mesh is used. However, the generation of a good quality mesh is often considered to be the most arduous and time consuming step of the entire simulation process.

For the numerical simulation of ground effect, different grids need to be created every time the angle of attack and ride height is varied. Apart from simply having a mesh that is able to capture all geometrical features of the FV, the mesh should also be capable of recording regions of the mesh that undergo large changes in flow variables such as pressure, temperature, velocity etc.

For the present study, all the meshes were created using the ANSYS Fluent Meshing tool. An unstructured grid comprising of polyhedral cells and refinements within the body of influence and in vicinity to the walls of the wing was created. Polyhedral cells have 10 faces and so opens the possibility of having ten different neighbors. This makes the calculation of gradients using nearest neighbor interpolations and linear shape functions much more accurate. These cells are less sensitive to larger aspect ratios and very effective in regions of re-circulation [1]. Peric [63] has shown that using a polyhedral cell mesh reduces the number of cells

required by almost four times when compared to a tetrahedral cell mesh. They bring down the memory requirement by 50% while using just a tenth of the total computation time needed by a tetrahedral mesh. Cross sectional views of the polyhedral cell mesh created for the entire domains in case of the wing IGE and OGE have been shown in figures 3.3a and 3.3b

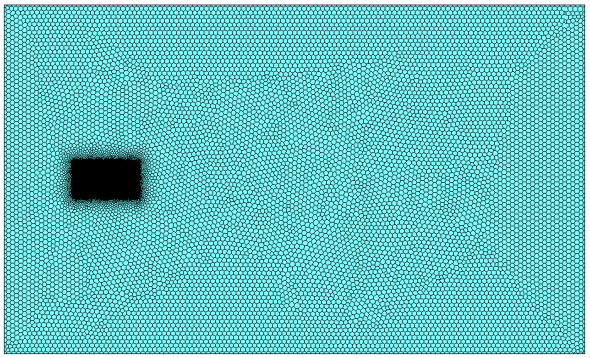

(a) Free-Stream Grid

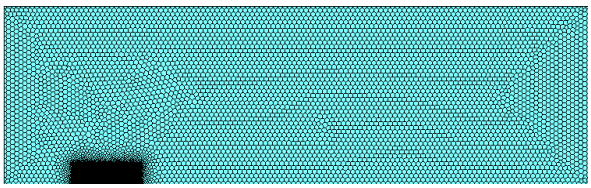

(b) Grid In ground effect

Figure 3.3

Since this thesis is based on a parametric study which requires the mesh to be created multiple times, decomposition of every mesh into specific sub-regions and domains of different refinements would be rather inefficient. Instead, a user defined 'body of influence' which can have any arbitrary shape or size and that intersects smoothly within the fluid domain was used. Figure 3.4 displays very clearly how the body of influence helps to slow down the refinement from the wing to the outer mesh while also setting up a well refined wake region. The polyhedral elements within the body of influence was specified to have a maximum size of 0.048 meters.

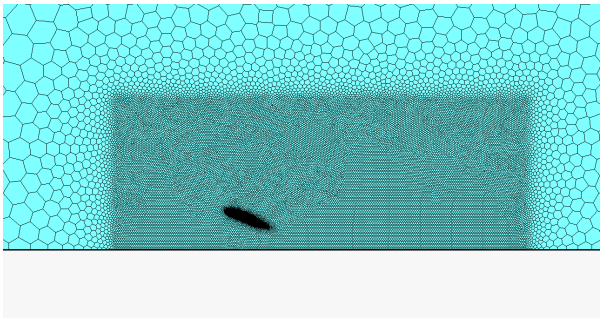

Figure 3.4: Body of Influence created for a WIG

To effectively capture the surface of the FV with great detail, the face sizing method was used where all elements on the surface mesh had a size of 0.003 meters. Figure 3.5 displays the mesh that was created on the surface of the FV.

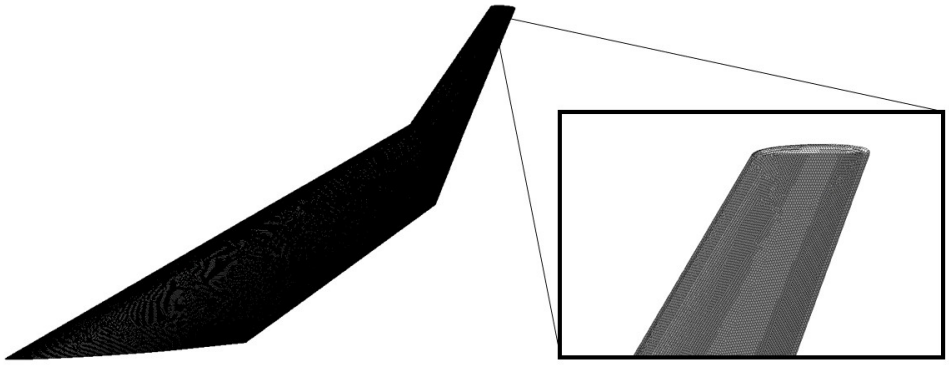

Figure 3.5: Surface Mesh created through face sizing on the FV geometry

From the far field, closer towards the surface of the FV, there is a decrease in the velocity profile of the flow, non linearly, up to a point which lies on the surface of the FV, where the velocity is equal to zero owing to the no-slip boundary condition that has been applied. It is important in any external flow CFD simulation that the mesh is able to capture this change in wall normal velocity. Boundary layer resolution is crucial to analyze the influence of the ground on the performance of the FV as the CFD results are expected to accurately determine the right locations of the separation point and pressure fluctuations on the surface. The boundary layer region can be captured by either making use of inflation layers or by using wall functions to approximate the shear stress. The non-dimensional number, y^+ gives an accurate indication of how well the boundary layer is discretized. It is given by the equation:

$$y^+ = \frac{u_\tau y_{\text{wall}}}{\nu} \tag{3.9}$$

where,

$$u_\tau = \sqrt{\frac{\tau_w}{\rho}} \tag{3.10}$$

In the above two equations, u_τ represents the skin friction velocity, τ_w is the wall shear stress given by equation 3.11 and y_{wall} is the height of the first layer of cells.

$$\tau_w = \frac{1}{2} C_f \rho V_\infty^2 \tag{3.11}$$

According to the 'law of the wall' [79], a fully developed boundary layer profile can be divided into different layers depending on the y^+ value. A $y^+ < 5$ corresponds to the viscous sub layer region. The buffer layer exists between $5 < y^+ < 30$. When $30 < y^+ < 300$ it corresponds to the log-law region.

When using wall functions to resolve the boundary layer, the first cell center can be placed within the log layer ($5 < y^+ < 30$). Now although they help to significantly reduce the number of cells and the time required for computation, wall functions limit the number of cells that can be sensibly placed within the boundary layer, causing errors due to approximations in the pressure drop and the velocity results starting from the first cell itself.

Based on a grid dependence study that was performed by Roberts et al [67], it was indicated that simply refining into the viscous sub-layer ($(y^+ < 5)$ would be insufficient to provide representative results and so a $y^+ \leq 1$ would be necessary. Therefore, throughout this thesis, all the meshes generated for the purpose of ground effect studies had a minimum $y^+ = 0.8$ thereby minimizing any approximations in the boundary layer flow.

The first cell height was calculated with respect to the maximum Reynolds number over the wing using the root chord length and the free stream velocity. Multiple inflation layers growing at a fixed growth rate of 20% with respect to the previous layer's thickness was used to encase the entire boundary layer. The Blasius solution for calculating the turbulent boundary layer thickness (δ) over a flat plate, given by equation 3.3 was used to approximately determine that a total of 40 inflation layers corresponding to a $y^+ = 0.8$ and a first cell height of 2.5×10^{-6} meters was used to simulate the FV in ground effect.

A cross sectional view of the inflation layers created around the wing is shown in figure 3.6a. Figure 3.6b highlights how well the inflation layers wrap around the curvature of the leading edge of the wing and its smooth transition into the far-field cells of the body of influence.

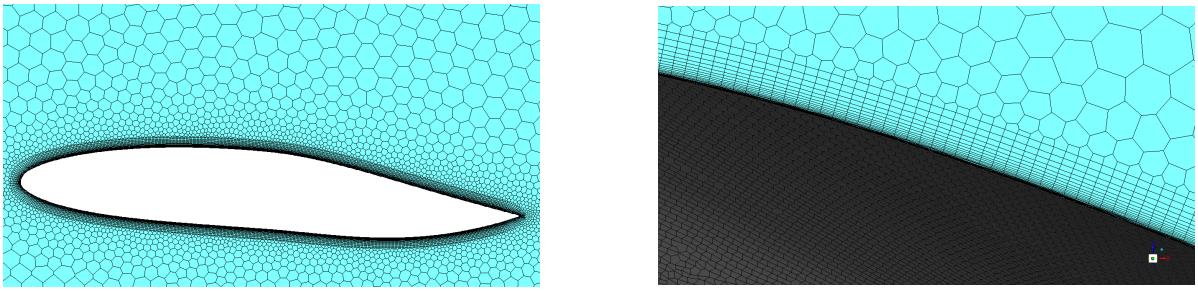

(a) Cross section of the wing

(b) Curvature of the leading edge of the wing

Figure 3.6: Inflation layers created to model boundary layer flow

Similar to the study conducted by Roberts et al, a grid dependence analysis was performed to determine the maximum element size within the body of influence that would be required to deliver accurate repeatable results. The conclusions and results drawn from this analysis have been documented in Section 4.3.

3.4. Boundary Conditions

The accuracy of any kind of numerical simulation does not just require a good understanding of the physics of the underlying problem but also an adequate selection of the turbulence model that will be used and the application of the right boundary condition [18]. It's for this reason that during the specification of the different boundary conditions, the different issues that can arise and the properties associated with each must be taken into account. In general fluid flow problems, the coupling of the velocity and pressure fields make designating inlet and outlet boundary conditions an arduous task.

It is important to keep in mind the conservation of mass across the inlet and outlet of the domain. Since the inlet boundary condition serves as a mass source of the fluid to the domain, the outlet boundary condition should serve as a mass sink. To guarantee that the right boundary conditions are applied at the inlet of the domain, a number of different criteria provided by [19] as listed below, can be used:

- Variation of physical properties
- Flow velocity direction and magnitude.
- Variation of turbulence properties at inlet.
- Uniform or non-uniform distribution of the specific parameter.

Different boundary conditions can be applied at the inlet and outlet planes of the domain. The most popular configuration known for its robustness and rapid converging potential is the imposed velocity profile at the inlet and a constant pressure at the outlet of the domain. This configuration has been used in a number of different studies pertaining to airfoils, wings, BWB and commercial aircrafts in ground effects such as [20] [42] [49] [88] [91]. However, the velocity inlet boundary condition is intended only for in-compressible flows and its use in compressible flow situations can cause erroneous results as it allows stagnation conditions to float to any magnitude [8]. For this reason a fluid pressure is defined at the inlet plane with a gauge pressure equal to 2865.6Pa and a total temperature of 290.45 K. At the outlet plane a static pressure of 0Pa is applied.

The upper plane of the domain and the side plane are considered as slip walls which have a specified shear stress equal to $0Pa$ in all three directions (x,y,z). The FV is a rigid body and so in order to model the viscous effects of the flow around it, the surface is assigned with the no slip boundary condition. This boundary condition implies that the velocity at the wall i.e. the surface of the FV is equal to 0. Finally a symmetry boundary condition was applied on the symmetry plane where the half model of the Flying V is mounted. This acts as a zero shear slip wall with zero flux across the plane.

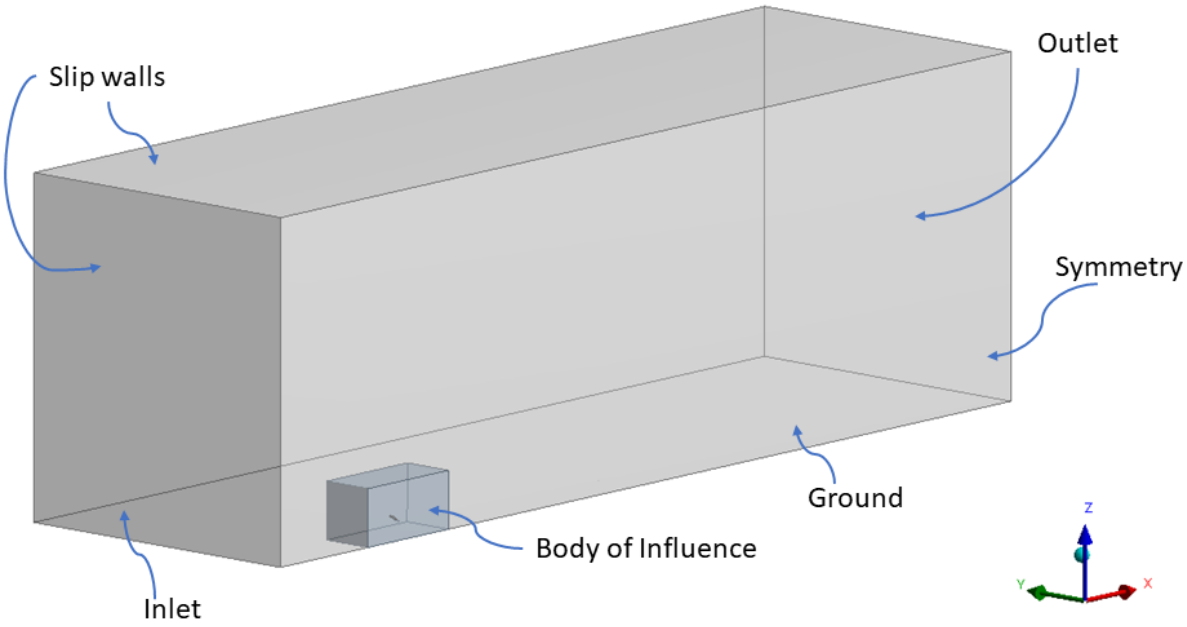

Figure 3.7: Illustration of boundary conditions applied on the computational domain walls

When studying the phenomenon of ground effect on any aircraft, it goes without saying that the boundary condition applied to simulate the ground should be very carefully imposed.

3.4.1. Ground Boundary Condition

Walker et al [83] on comparing the theoretical and experimental studies in the area of ground effect noted that incorrect assignments of ground surface boundary conditions caused computational and experimental results to differ from each other by a huge margin. For instance, if viscous effects are not taken into consideration correctly, there can be an over prediction of the lift-drag ratios as a result of an under prediction in the values of the drag forces.

Past literature has shown that there has always been a huge predicament when it comes to the selection of the right ground boundary condition. After modeling the ground using a no-slip boundary condition and analyzing six different airfoils in laminar, in-compressible and viscous flow at varying heights above the ground, Hsiun and Chen [37] concluded that the efficiency of an airfoil in ground effect depended on the space between the airfoil and the ground. When replicated in a wind tunnel, the no-slip boundary condition is identical to a stationary ground. A couple of years later in 1997, Steinbach [76] commented that the right ground boundary condition that should have been used in this study was a slip wall. A slip wall, in CFD, as mentioned in the previous subsection refers to a boundary that has zero shear stress. He further recommends that the correct boundary condition for the ground would be a 'reflected grid', similar to a symmetry wall. Now for a slip wall boundary, the normal component of velocity is set to zero, allowing the ground to move at different speeds relative to the aircraft flying above it. A symmetry boundary condition however sets all the normal gradients to zero. These boundaries if employed, would result in different solutions. George [30] and Fago et al [25] both came to a similar conclusion and suggested that a moving ground boundary condition should instead be used to study bluff bodies which are positioned at heights equal to or lesser than 10% of the body's length.

In 2006, T. Barber et al [11] studied the performance of the NACA 4412 airfoil with all four of these different boundary conditions - stationary(no-slip), slip, symmetry and a moving ground. The velocity profiles obtained after using each of these ground boundary conditions is shown in figure 3.8.

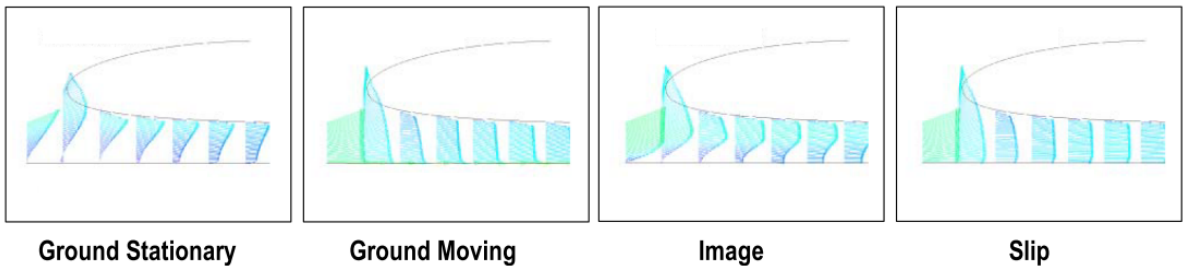

Figure 3.8: Velocity profiles for different ground boundary conditions at a h/c=0.025 of a NACA 4412 airfoil [11]

In case of the stationary ground and the image models, a re-circulation region was observed below the leading edge of the airfoil. A similar trend was also observed in case of the image model. The ground moving model however showed velocity vectors increasing in magnitude as the speed of the flow increased to meet the wall velocity. Using Particle Image Velocimetry (PIV) to experimentally observe the effects of having a moving ground and a stationary ground, he observed that towards the lower boundary, in case of the former, the flow stays uniform and a boundary layer is only produced at the upper boundary where the wall is stationary as shown in figure 3.9b. In the ground stationary configuration, seen in Figure 3.9a, he observed incorrect boundary layers located both at the upper and the lower boundaries. Based on his numerical computations and experimental investigations, he thus concluded that the moving ground boundary condition is the most accurate in representing the ground when an aircraft is positioned at a very low altitude.

In a study on boundary layer control with a moving belt that was conducted by Ahmed [6], he quoted from a study of a 2D wing profile in the stationary ground model by Beese [12] that the displacement thickness in the stationary ground model can achieve negative values. Instead of displacing mass, this would cause the boundary layer to then draw fluid from the in-viscid flow at its edge, in turn introducing an angularity into the flow, leading to significant errors. He too concluded that the moving ground boundary condition would offer the best simulation of the ground effect.

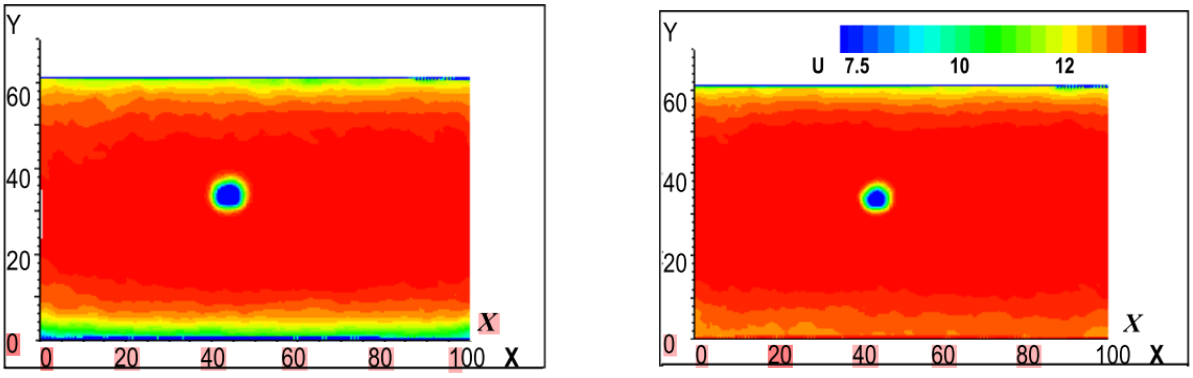

(a) Stationery ground

(b) Moving Ground

Figure 3.9: Mean velocity profiles obtained using PIV with a cylinder placed in the domain [11]

Based on the above mentioned conclusions from previous literature and supported by the use of a similar boundary condition in Deng[20], C.T. Lao et al[45] and Sereez et al [74], the moving ground boundary condition will be used in this thesis to assess the performance of the FV. This moving ground will move at a velocity equal to 0.2 Mach, ensuring a condition that best represents real life conditions. This is because in a ground fixed reference frame, both air and ground is fixed as the aircraft flies over the ground, however in a vehicle fixed reference frame as in the case of a wind tunnel experiment or a CFD simulation, the opposite occurs and both air and the ground must move at a velocity equal to the free stream velocity.

Table 3.3: Boundary conditions applied on each zone of the computational domain to perform RANS simulations

Zone	Boundary Condition
Inlet	Pressure inlet with gauge pressure =2865.6 Pa and T_t = 290.45K
Outlet	Pressure outlet where the static pressure = 0 Pa
Upper	Slip wall with specified shear stress equal to zero
Side	Slip wall with specified shear stress equal to zero
Ground	No slip translational moving wall in the (1 0 0) direction with a velocity equal to free-stream
Symmetry	Symmetry
FV	No slip wall

3.5. Turbulence Modeling

3.5.1. Navier Stokes Equation

By applying Newtons laws of motion to a fluid element the governing equations for a viscous fluid can be obtained. These governing equations which are the conservation of mass, the conservation of momentum and the conservation of energy are together called as the Navier Stokes equations. Depending on the compressibility of the fluid, these equations behave differently.

For a compressible Newtonian fluid, the Navier Stokes equations are given by,

$$\frac{\partial \rho}{\partial t} + \frac{\partial}{\partial x_j}\left[\rho u_j\right] = 0 \tag{3.12}$$

$$\frac{\partial}{\partial t}\left(\rho u_i\right) + \frac{\partial}{\partial x_j}\left[\rho u_i u_j + p\delta_{ij} - \tau_{ji}\right] = 0 \tag{3.13}$$

$$\frac{\partial}{\partial t}\left(\rho e_0\right) + \frac{\partial}{\partial x_j}\left[\rho u_j e_0 + u_j p - u_i \tau_{ij}\right] = 0 \tag{3.14}$$

where the total energy e_0 is defined as

$$e_0 = e + \frac{u_k u_k}{2} \tag{3.15}$$

and the viscous stress, τ_{ij} is given by

$$\tau_{ij} = 2\mu S_{ij} \tag{3.16}$$

In the above equation the viscous strain-rate (S_{ij}) is defined as

$$S_{ij} \equiv \frac{1}{2}\left(\frac{\partial u_i}{\partial x_j} + \frac{\partial u_j}{\partial x_i}\right) - \frac{1}{3}\frac{\partial u_k}{\partial x_k}\delta_{ij} \tag{3.17}$$

In order to close equations 3.12, 3.13 and 3.14 the equation of state for an ideal gas, given by equation 3.18 is also necessary to be solved.

$$pV = \rho RT \tag{3.18}$$

The viscosity is then calculated using the Sutherland's law which is given by equation 3.19 assuming that air within the domain is a calorically perfect gas. In the equation, $\mu_{ref} = 1.716 \times 10^{-5} PaS$ and T_{ref} = 273.15K are the reference values of viscosity and temperature and S = 110.4K is known as the Sutherland's constant.

$$\mu = \mu_{ref}\left(\frac{T}{T_{ref}}\right)^{\frac{3}{2}} \frac{T_{ref} + S}{T + S} \tag{3.19}$$

Direct Numerical Simulation (DNS) offers a complete solution to the Navier Stokes equations both spatially and temporally by making use of integral length scales and capturing the kinetic energy dissipation which occur on scales that possess viscosity, called the Kolmogrov scales [26]. The computational cost for running a DNS to resolve all the time and length scales scales with $Re^{2.7}$ [65]. Additionally, since the number of cells required for a computation is limited by the performance and memory of today's computers the use of DNS is restricted to only low Reynolds number flows with simple geometries.

It is for this reason that different methods that offer the right amount of compromise between accuracy and computation cost have been developed. One such method that is used to carry out the majority of today's CFD simulations within the industry is the RANS formulation [22].

3.5.2. Reynolds Averaged Navier Stokes Equation

In case of an in-compressible fluid, the process of Reynold's averaging is applied to a variable or an equation in time, given by equation 3.21. This is done to separate turbulent fluctuations from the mean flow [8]. To do this a variable Φ is first decomposed into its mean and fluctuating components (Reynolds decomposition) given by equation 3.20

$$\Phi \equiv \overline{\Phi} + \Phi' \tag{3.20}$$

$$\overline{\Phi} \equiv \frac{1}{T}\int_T \Phi(t)\,dt \tag{3.21}$$

For a compressible fluid, ANSYS Fluent applies a density weighted time averaging method called the Favre averaging in addition to the classical time averaging given by equations 3.20 and 3.21 [8]. Seen in equation 3.22 is the process of density weighted averaging which is done by multiplying a parameter, say Φ with the density ρ, calculating the average of this product and dividing it with the average of the density.

$$\widetilde{\Phi} \equiv \frac{\overline{\rho\Phi}}{\overline{\rho}} \tag{3.22}$$

$$\Phi \equiv \Phi'' + \widetilde{\Phi} \tag{3.23}$$

As given in Vos et al [80], in case of Reynold's averaging, the variable Φ denotes the velocity components where the primed parameters stand for fluctuations from the average which are equal to zero when integrated over time. In case of Favre's averaging, the variable Φ refers to scalar quantities like pressure, energy etc. In this case, the average of the doubly primed quantities are not equal to zero but the product of the density with the doubly primed fluctuations is (i.e. $\frac{1}{\Delta t}\int_0^{\Delta t} \rho u''\,dt = 0$).

Now by substituting the averaged parameters into equations 3.12, 3.13 and 3.14 and time averaging these equations we obtain:

$$\frac{\partial \overline{\rho}}{\partial t} + \frac{\partial}{\partial x_i}\left[\overline{\rho}\widetilde{u_i}\right] = 0 \tag{3.24}$$

$$\frac{\partial}{\partial t}\left(\overline{\rho}\widetilde{u_i}\right) + \frac{\partial}{\partial x_j}\left[\overline{\rho}\widetilde{u_j}\widetilde{u_i} + \overline{p}\delta_{ij} - \widetilde{\tau_{ji}^{tot}}\right] = 0 \tag{3.25}$$

$$\frac{\partial}{\partial t}\left(\overline{\rho}\widetilde{e_0}\right) + \frac{\partial}{\partial x_j}\left[\overline{\rho}\widetilde{u_j}\widetilde{e_0} + \widetilde{u_j}\overline{p} - \widetilde{u_i}\widetilde{\tau_{ij}^{tot}}\right] = 0 \tag{3.26}$$

where,

$$\widetilde{\tau_{ij}^{tot}} \equiv \widetilde{\tau_{ij}^{lam}} + \widetilde{\tau_{ij}^{turb}} \tag{3.27}$$

$$\widetilde{\tau_{ij}^{lam}} \equiv \widetilde{\tau_{ij}} = \mu\left(\frac{\partial \widetilde{u_i}}{\partial x_j} + \frac{\partial \widetilde{u_j}}{\partial x_i} - \frac{2}{3}\frac{\partial \widetilde{u_k}}{\partial x_k}\delta_{ij}\right) \tag{3.28}$$

$$\widetilde{\tau_{ij}^{turb}} \equiv -\overline{\rho u_i'' u_j''} \approx \mu_t\left(\frac{\partial \widetilde{u_i}}{\partial x_j} + \frac{\partial \widetilde{u_j}}{\partial x_i} - \frac{2}{3}\frac{\partial \widetilde{u_k}}{\partial x_k}\delta_{ij}\right) - \frac{2}{3}\overline{\rho}k\delta_{ij} \tag{3.29}$$

Equations 3.24 - 3.29 together form the Reynolds averaged Navier Stokes equations for a compressible perfect gas.

3.5.3. Eddy Viscosity Modeling

The term $-\overline{\rho u_i'' u_j''}$ seen in equation 3.29 is known as the turbulent Reynolds stress and it accounts for the turbulent fluctuations in fluid momentum. It's presence in equations 3.24 and 3.25 introduces a closure problem. In order to solve this closure problem, a set of approximations to the Reynolds stress term can be made in terms of mean quantities. Different orders of closure exist when it comes to the mathematical solution of this problem. A first order closure evaluates the Reynolds stress as a function of only the mean velocity and geometry. By using the solution obtained from modeling transport equations for different turbulence characteristics, a second order closure can be obtained [40]. The order of closures can even be cubic or quadratic,

but at the same time the level of complexity also increases. These different approximations that are applied, do so in the form of different "turbulence models." Each of these turbulence models have their own set of advantages and disadvantages.

Based on previous literature such as [20, 49, 74, 89, 90], four different eddy viscosity models commonly grouped according to the number of transport equations that are associated with each method, namely the one equation Spalart- Allmaras (SA) model and the two equation standard $k-\epsilon$ model, $k-\omega$ model and $k-\omega$ Shear Stress Transport (SST) model, were shortlisted to be tested in a validation study presented in chapter 4

3.6. Solution Methods and Solver Settings

The commercial CFD software ANSYS Fluent 2019r1 was used as the solver to perform the computations. The pressure-velocity coupling schemes and the various spatial discretization schemes that were employed to run the simulations are discussed below.

3.6.1. Pressure Velocity Coupling

To solve the discretized Navier Stokes equation, two different approaches known as the segregated approach and the coupled approach exist [8]. Both these approaches solve the continuity, momentum and energy equations differently. For instance, the segregated approach sequentially solves the equations which are themselves separated from each other. On the other hand, the coupled method will solve the governing equations simultaneously.

The need for using a pressure-velocity coupling arises as pressure is not a conserved property and has no governing transport equation of its own. When observing the equation of continuity given in 3.24, it is seen that pressure is not explicitly featured in it. This would cause the continuity equation to act as an additional constraint on the velocity field [57]. The Navier Stokes equations however do show a dependence of the pressure on the velocity and visa versa. This dependence is brought about by the coupled approach by making use of inter-equation coupling while the segregated approach makes use of one of the 3 available pressure velocity coupling methods made available by ANSYS Fluent:

- SIMPLE (Semi-Implicit Method for Pressure Linked Equations)
- SIMPLEC (Semi-Implicit Method for Pressure Linked Equations- Consistent)
- PISO (Pressure Implicit with Split Operator)

SIMPLE

For the simulations performed in this thesis, the SIMPLE algorithm was used. This algorithm enforces the mass conservation by creating a relationship between pressure and velocity to obtain the pressure field [8]. It utilizes a guessed pressure correction field that is substituted into the continuity equation and updated until the equation satisfies the velocity.

The momentum equation is first solved to calculate the velocity field after which, using the pressure distribution from a previous iteration or an initial guess the pressure gradients are calculated.

Essentially, the corrected velocity and pressure variables are given by,

$$u = u^* + u' \tag{3.30}$$

$$p = p^* + p' \tag{3.31}$$

where $(\cdot)^*$ refers to guessed values and $(\cdot)'$ refer to corrections that are applied.

In Fluent an under relaxation is applied as seen in equation 3.32 because the methodology used for pressure correction is prone to divergence [57].

$$p = p^* + \alpha p' \tag{3.32}$$

The under relaxation factor α ranges between 0 and 1.

The SIMPLEC pressure velocity coupling makes use of under relaxation factors ranging between 0.7 and 1. these high values of α can lead to instability due to high mesh skewness and so it would make more sense to use the SIMPLE algorithm.

The PISO algorithm is mostly recommended for transient flow calculations when a large time step is desired [8]. PISO performs additional corrections namely, the neighbor correction and the skewness correction to obtain a higher degree relation between the pressure and velocity corrections.

3.6.2. Computation of Gradients

The calculation of scalars at the cell faces, secondary diffusion terms and derivatives of velocity make the calculation of gradients an indispensable step [8]. In ANSYS Fluent, three different methods are made available, namely:

- Green Gauss Cell Based (GGCB)
- Green Gauss Node Based (GGNB)
- Least Squares Cell Based (LSCB)

As their names suggest, the GGCB and GGNB methods apply the Green Gauss Theorem, as presented in equation 3.33, on arbitrary control volumes to calculate the gradients of a variable.

$$\nabla\phi = \frac{1}{\forall}\sum_{f}^{N_{faces}} \phi_f A_f \tag{3.33}$$

where ϕ_f is the value of ϕ at the cell face centroid.

According to this theorem, the gradient of a scalar ϕ, over a control volume $\forall$, is equal to the sum of the products of the face value ϕ_f and surface vector A_f [51].

The Green Gauss methods mentioned above calculate the value of ϕ_f in two different ways.

- The GGCB method calculates the face value of ϕ_f as the average of two adjacent cells irrespective of the quality of the cell.

$$\phi_f = \frac{\phi_a + \phi_b}{2} \tag{3.34}$$

  In equation 3.34, ϕ_a and ϕ_b are scalar values at the cell centers of two cells that have a common face.

- The GGNB method calculates ϕ_f as the mean of values of the nodes on the face as seen in equation 3.35

$$\phi_f = \frac{1}{N_f}\sum_{n}^{N_f}\phi_n \tag{3.35}$$

  In the above equation, N_f refer to the number of nodes per face and ϕ_n is the weighted average of surrounding cells.

- The least square cell based method uses the least square approximation[2]

The process by which GGNB calculates the value of ϕ_f i.e. by solving a minimization problem to obtain exact solutions of a nodal linear function allows it to be at least first order accurate along with the LSCB method for any cell geometry. GGCB is reported to be highly inconsistent [51]

Deciding between GGNB and LSCB was seen to be highly case specific. Simulations were run separately with each of these methods but results showed that the LSCB method would cause the equations of continuity and momentum to blow up for all tested cases. The Green Gauss Node Based method delivered repetitive results consistently for all tested cases albeit being computationally intensive compared to the LSCB method which is why it was chosen as the method to compute the gradients.

[2]Method of minimizing the sum of the squares of the residuals for every equation

3.6.3. Spatial Discretization

Choosing the order of discretization depends on the alignment of the mesh with the flow. A first order scheme is admissible when the mesh is well aligned with respect to the fluid flow direction. However, when there is a misalignment between the two and the fluid crosses the edges of the cells in the mesh at an angle, then the first order scheme would lead to an increase in the numerical diffusion. In case of a polyhedral mesh, a constant alignment with the fluid flow is not possible and so a second order discretization scheme would be more apt to use [8].

Pressure

For the discretization of the momentum equation, the face pressure values between adjacent cells is required but is unknown. For this, ANSYS Fluent provides different interpolation schemes that compute this from values stored in the cell centers. The schemes are:

- Standard
- PRESTO!
- Linear
- Second order
- Body force weighted

For this study, the second order scheme was selected to be used as it has been reported to offer better improvement over the standard and linear schemes [8]. The other schemes are typically used in the presence of large body forces, presence of porous media, high swirl numbers etc.

Density

When the flow is in-compressible, ANSYS Fluent uses arithmetic averaging for the calculation of density. However, when the flow is compressible, as mentioned previously, in equation 3.18 , the ideal gas law is used to compute density and so Fluent utilizes an upwind interpolation on the cell faces. Many such upwind interpolation schemes are offered, such as:

- First order upwind
- Second order upwind
- Quadratic Upstream Interpolation for Convective Kinematics (QUICK)
- Monotonic Upwind Scheme for Conservation Laws (MUSCL)

The first order upwind scheme which equates the cell face density to the cell center value is considered to be the best in terms of stability to discretize the pressure correction equation (equation 3.32) when compared with the other methods. However this first order upwind scheme brings with it very large diffusivity. QUICK is typically used in the presence of shocks and MUSCL is way too expensive computationally as this scheme is third order accurate [8]. For this reason, the second order upwind discretization scheme is used.

Other quantities such as momentum, turbulent kinetic energy and the total energy are also discretized using the second order upwind discretization.

3.6.4. Convergence Criteria

A CFD simulation consists of an iterative procedure to arrive at a final solution. In this study a steady state flow is desired and so an initially uniform flow field is iterated over a period of time until a steady state flow field is obtained. This is termed as convergence. Convergence as such depends on a number of different criteria. One such criteria is the 'residual' which is defined as the change of a conserved variable in each cell volume of a mesh. The residual calculated is local to every cell volume and can never be equal to zero. A keen eye must always be kept on the forces during every simulation. A number of different convergence criteria are required to be met in order to ensure sufficient accuracy:

- The first criteria is that the absolute residuals fall below a specified tolerance.
- The coefficients of lift, drag and pitching moment arrive at a steady constant value.
- The total number of iterations specified have been computed.

A detailed description of the different convergence criteria adopted are presented in section 4.3

4

Verification and Validation

As stated by Dose[22], the CFD simulations conducted within industry is based on the modeling of the RANS equations using different turbulence models. The use of these turbulence models are a source of modeling errors as each of them model the Reynolds stress term ($\overline{-\rho u_i'' u_j''}$) by making different approximations. It is therefore essential for the credibility of the results that these modeling errors can be quantified. This chapter aims to do just that by:

- Testing the accuracy of different turbulence models
- Studying the influence of the domain boundaries on the solution
- Taking into account the effects that grid refinement has on the solution by performing a grid dependency study
- Analyzing the grid quality.

4.1. Validation of turbulence Model

The validation of a turbulence model is an important step to determine the extent to which a particular model can accurately represent the solution obtained from an experimental investigation or the results obtained from using a higher fidelity method. High fidelity methods like Direct Numerical Simulations (DNS) and Large Eddy Simulations (LES) are used for comparison as they resolve a larger range of scales involved in turbulent flow compared to the models that are used in RANS.

4.1.1. Validation Case

The LES results obtained by Jac van Egmond at **mvAERO** were used as the reference case for the comparison of results that were obtained by running different turbulence models. In his study the 4.6% scaled model of the FV in unbounded flow was used. The FV was oriented at 4 different angles of attack i.e. $0°, 10°, 20°, 30°$, while the inlet velocity was set at 20ms^{-1}. Based on a reference chord length of 0.8204 meters, the Reynolds number of the flow was estimated to be about ≈ 1 million. The density and viscosity of air was set at 1.225kgm^{-3} and $1.78 \times 10^{-5} PaS$ Standard Temperature and Pressure (STP).

A separate computational domain was created such that its ground and upper plane were at a distance of $33.33b$ from the origin that is located at the tip of the leading edge on the root of the wing. As shown in 4.1, by placing these planes away from the wing, the FV can be assumed to be in unbounded flow. Similar to the computational domain shown in figure 3.2a, a body of influence was created around the wing with dimensions $20b \times 13.33b$. Since a domain sensitivity study was not performed for the validation study, the boundaries of the domain were placed at a larger distance away from the FV. The inlet plane was located at a distance of $33.33b$ from the origin while the outlet was located at a distance of $100b$ from the inlet plane. This was done to ensure that the boundary conditions applied on the walls of the computational domain did not influence the results of the simulation. Further explanation on how this can occur is given in section 3.3. Boundary conditions similar to those mentioned in 3.3 were also applied for this domain with the exception of the ground plane which was set as a slip wall owing to the simulation being in unbounded flow.

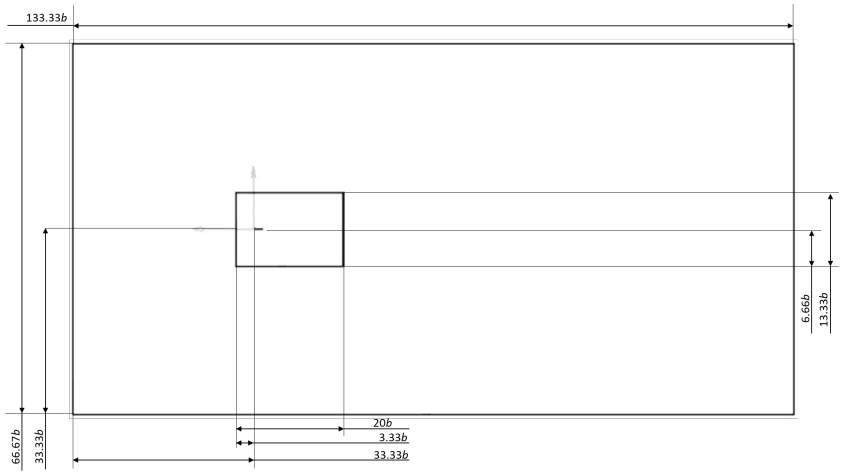

Figure 4.1: Computational Domain used for the validation study and also for unbounded flow simulations

The mesh that was generated was created with a maximum edge length of 0.8 meters in the far-field. The boundary layer was resolved using 30 inflation layers that had a fixed first cell height of 8.9×10^{-6} meters for a corresponding $y^+ = 0.5$. The body of influence had a maximum element size of 0.048 meters while the surface mesh had a fixed face sizing of 3×10^{-3} meters. Based on this refinement, the total number of elements was approximately equal to 25 million.

4.1.2. Comparison of Aerodynamic Coefficients

The aerodynamic coefficients of lift, drag and pitching moment computed using the four different turbulence models are shown in figures 4.2 4.3 and 4.4. Also included in these images, in addition to the LES results, are the aerodynamic coefficients that were obtained by Palermo [59] for the same test case along with the results he obtained from CFD using the Spalart Allmaras (SA) turbulence model to validate his experimental results.

In figure 4.2 the aerodynamic lift coefficients calculated by the different methods are plotted against α varying between 0° and 30°. It is seen that the different computational methods i.e. both LES and RANS, predict a similar 'linear' increase in lift with an increasing angle of attack. The numerical methods over predict the values of C_L at all angles of attack when compared with the experimental values and the deviation from the experimental results is seen to increase as the angle of attack increases. A maximum deviation of about 11.6% between the SA turbulence model and the experimental value is seen at $\alpha = 30°$

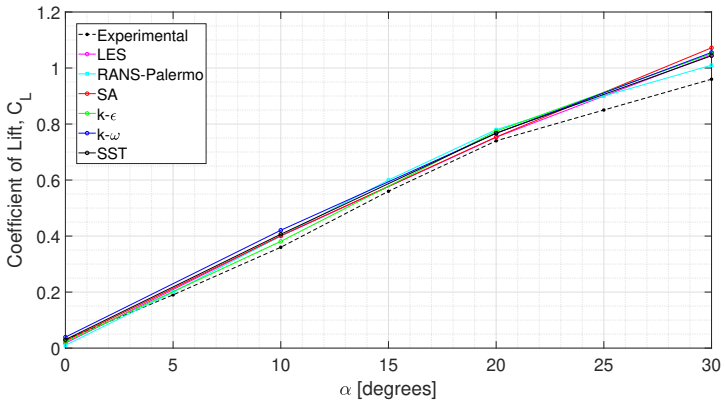

Figure 4.2: Comparison of coefficient of lift, C_L, calculated by the different turbulence models with LES results obtained by Egmond[24] and the results obtained by Palermo[59]

The comparison of the coefficient of drag with respect to α is shown in figure 4.3. As would be expected all curves predict the increase in drag that is associated with an increase in α as a result of the increase in frontal area of the wing in the direction of the flow and an increase in the thickness of the turbulent boundary layer. However, similar to the plot seen above in figure 4.2 there is an increasing disparity between the individual

values of C_D calculated by the different methods that begins from moderate to high angles of attack. The $k-\epsilon$ model shows the greatest deviation from the experimental results at $\alpha = 30°$ by almost 30.2%. With regard to the CFD simulations carried out by Palermo, there is a good overall agreement between the calculated lift coefficients. At low angles of attack however, there appears to be a difference of about 3.2% that remains consistently up to $\alpha = 15°$ after which a better correlation is seen between the calculated drag coefficients.

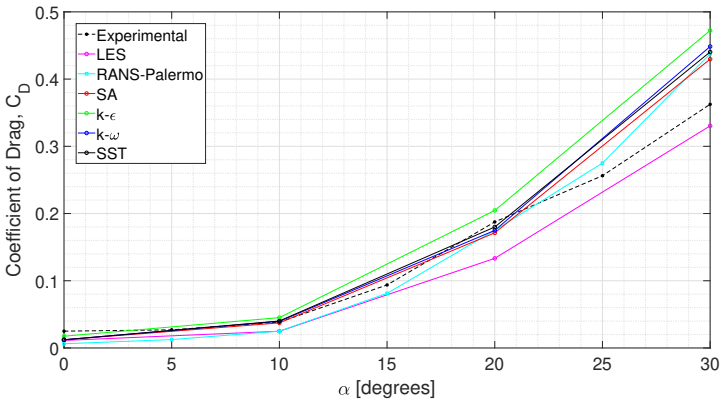

Figure 4.3: Comparison of coefficient of drag, C_D, calculated by the different turbulence models with LES results obtained by Egmond[24] and the results obtained by Palermo[59]

Lei [46] while studying the effect of RANS turbulence models over a wing body configuration for α varying between $-5°$ and $40°$ and a Reynolds number of 9.45×10^5 addressed the similar discrepancy that is seen in the lift and drag coefficient curves calculated by the turbulence models and the experimental results.

The large inconsistencies that are seen in the drag forces are explained by the inability of the turbulence models to include the laminar-turbulent transition [46], specifically the SA turbulence model. This turbulence model fails to predict large separation and vortex breakdown which typically occur at high angles of attack resulting in dissipation that is large enough for estimating only smaller separation and so an increase in the lift and drag coefficients is seen. In case of the $k-\epsilon$ model it was reported that the model poorly predicts leading edge separation where pressure gradients are stronger but does well in capturing flow away from the walls[46].

In figure 4.3, among the four different turbulence models tested, the SA model is observed to display the closest results to LES. On the other hand, the $k-\epsilon$ model shows the maximum deviation from LES while the $k-\omega$ and $k-\omega SST$ models show slightly closer results to that of SA. To explain the differences between the RANS results and LES, the way each of these numerical methods solve turbulence needs to be further assessed. Over the FV and in its wake, the flow is extremely complex and the distribution of the strain rate tensor $\overline{S_{ij}}$ is highly anisotropic changing relative to the position of the FV. The different turbulence models however, are based on the isotropic modeling of the eddy viscosity and so are limited in their ability to accurately capture the anisotropy of the components of Reynolds stresses. This was also reported by Gatski and Rumsey [28] and Murakami [56]. An additional factor that plays a role in the offset of values is the fact that LES is a high fidelity approach used in CFD to model turbulence by explicitly resolving the larger turbulent scales. It makes use of high order or low order numerical schemes depending on if an extremely fine grid is used. As such it is characterized by very less numerical diffusion/dissipation errors which would explain the lower drag coefficient values as compared to those obtained from the Eddy viscosity models. Analyzing figure 4.4 qualitatively, it can be seen that both LES and RANS predict a similar trend in the pitching moment from $\alpha = 0°$ and $\alpha = 20°$

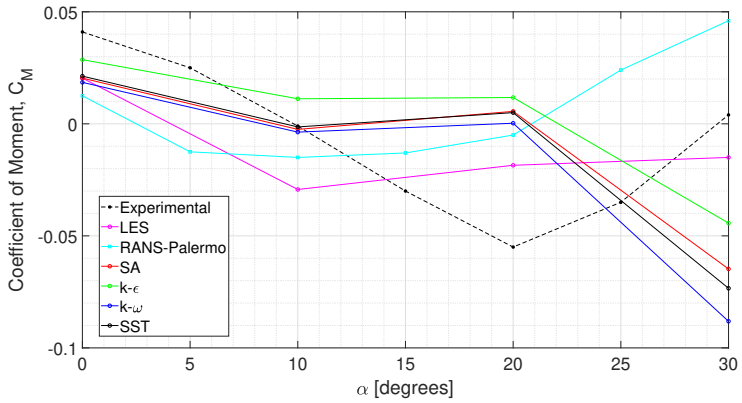

Figure 4.4: Comparison of pitching moment coefficient, C_M, calculated by the different turbulence models with LES results obtained by Egmond[24] and the results obtained by Palermo[59]

There is a nose down moment predicted up to 10° after which all turbulence models and the LES show a nose up moment. The experimental results however, show a significant different with respect to LES and RANS. A nose down moment is obtained all the way to $\alpha = 20°$.

For $\alpha > 20°$ however, significant inconsistencies are seen with respect to the moments calculated by all the different methods. Experimental values of C_M and the RANS results obtained by Palermo [59] predict a pitch up break tendency with a difference of about 91.30% between the two magnitudes at $\alpha = 30°$. LES predicts a slight nose up pitching moment of 18.9% with respect to the moment coefficient at $\alpha = 20°$ which dwarfs in comparison to what is predicted from the experimental and RANS results of Palermo which sees a 105% increase in the magnitude of moment coefficient from $\alpha = 20°$ to $\alpha = 30°$.

Now in order to gain an overall perspective of which turbulence model works the best when compared to the LES results, the Root Mean Square Error (RMSE) given by equation 4.1 was calculated.

$$RMSE = \sqrt{\frac{\sum_{i=1}^{N}(x - x_i)^2}{N}} \tag{4.1}$$

where x_i is the calculated coefficient, x is the known result and N is the sample size.

The calculated RSME for each of the coefficients is presented in table 4.1.

Table 4.1: Root mean square errors of the aerodynamic coefficients calculated by the different turbulence models

Turbulence Model	$\mathbf{C_{L,RMSE}}$	$\mathbf{C_{D,RMSE}}$	$\mathbf{C_{M,RMSE}}$
SA	0.0133	0.0535	0.0307
$k-\epsilon$	0.0148	0.0801	0.0295
$k-\omega$	0.0170	0.0630	0.0399
$k-\omega$ SST	0.0104	0.0602	0.0344

Based on the calculated values of RMSE, the $k-\omega SST$ model had the least overall C_L deviation at 0.0104 while the $k-\omega$ model was calculated to have the highest. The SA model showed the least deviation when comparing the drag coefficient C_D. Although all the turbulence models predicted a nose down pitch break after $\alpha = 20°$, the lowest $C_{M,RMSE}$ was attributed to the $k-\epsilon$ model. For conclusive evidence on which turbulence model would work best, a further investigation of the results obtained was necessary.

4.1.3. Comparison of Contours

The comparison of the aerodynamic coefficients by the different turbulence models is insufficient in determining the right turbulence model. These models need to also be able to accurately represent the flow phenomena. For this reason, the pressure coefficient (C_P) contours on the surface of the wing are compared with those from LES. In figure 4.5 the pressure coefficient contours on the suction side of the FV oriented at $\alpha = 20°$ obtained from different turbulence models is compared with the same from LES.

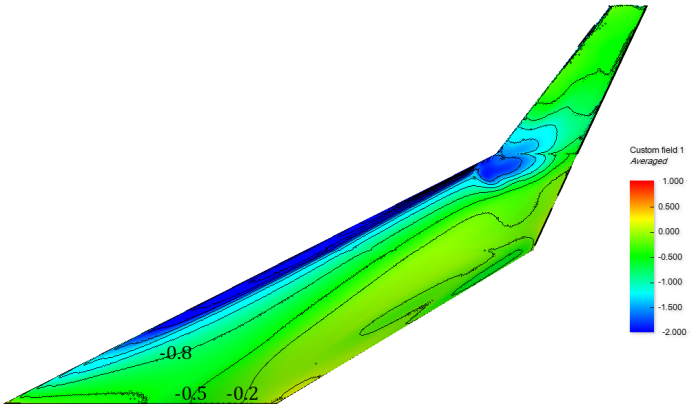

(a) LES [24]

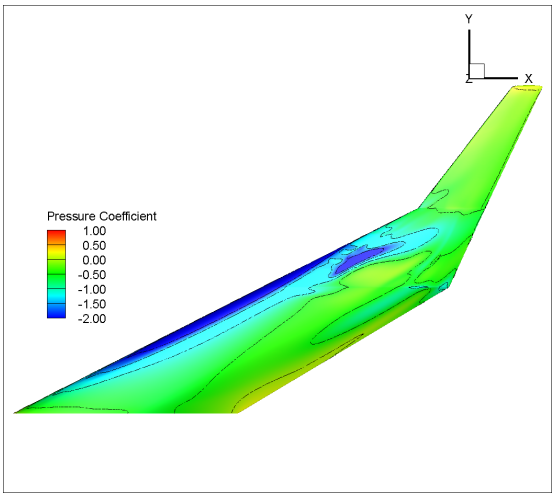

(b) Spalart-Allmaras model

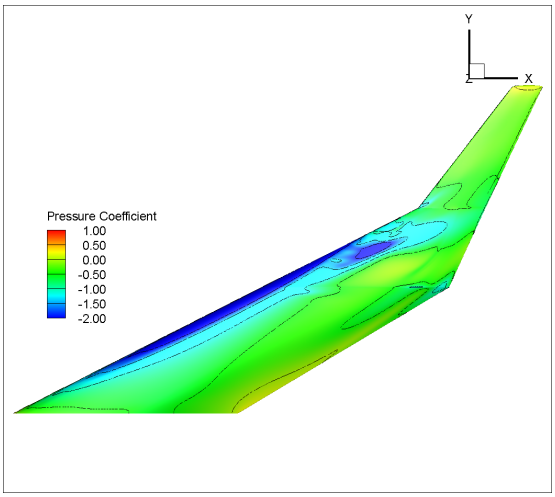

(c) k-ω model

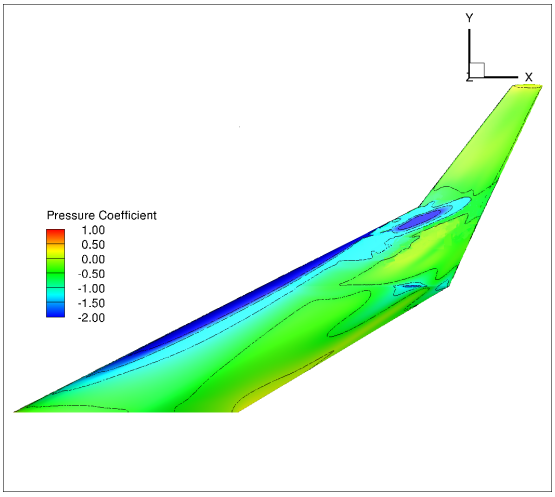

(d) SST model

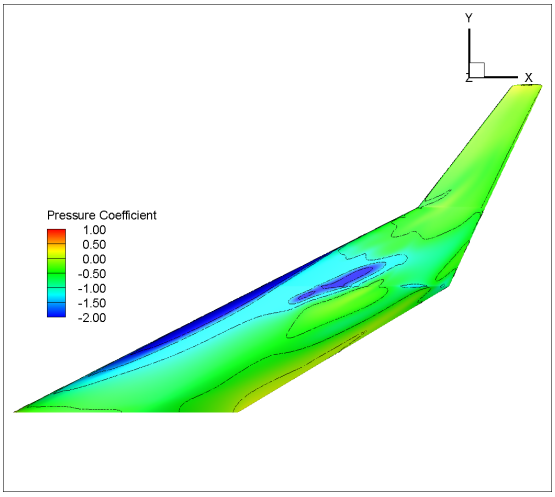

(e) k-ϵ model

Figure 4.5: Contours of Pressure Coefficient on the Upper Surface of the FV

In figure 4.5 it can be seen that all four turbulence models predict the acceleration of the flow over the leading edge of the wing quite well. Towards the trailing edge of the wing, close to the root, the high pressure region (indicated by the slight shade of yellow) is also well predicted by the eddy viscosity models. A significant difference however, is seen between the models at the leading edge kink of the wing where the flow accelerates outward. From the visualization of the iso-surfaces of vorticity, Palermo [59] has shown that a large vortex exists in this region which is why an acceleration is seen. The SA , $k-\epsilon$ and the $k-\omega$ models all

fail to accurately position the location of this vortex and instead place it towards the end of the inboard trunk of the FV. The $k-\omega$ SST model on the other hand successfully predicts the location of this low pressure region as is seen in figure 4.5b.

In a study on the vortex breakdown detection over a delta wing, Wibowo et al [84] too studied the influence of employing different turbulence models. They showed that the SA turbulence model delays the formation of a vortex breakdown while on the contrary the $k-\omega$ and $k-\epsilon$ models produced results that were identical and produced vortex cores that were lesser in strength. It was the $k-\omega$ SST model that presented the best match with the experimental results and also with those obtained from carrying out LES. Lei [46] in his study offered an explanation for this by attributing the failure of the SA model in capturing the vortex formations as a result of its highly dissipative nature. He also reported that the $k-\epsilon$ model does show results similar to the $k-\omega$ model and the $k-\omega$ SST, however at high angles of attack the model fails because of a large amount of dissipation within the vortex core and near wall regions.

Based on these recommendations and the comparisons made in sections 4.1.2 and 4.1.3, the **k − ω SST** model was selected as the best turbulence model to be used for this study of ground effect on the FV.

It is interesting to note that the test case that was used to determine that the $k-\omega$ SST model was the best, was one that was highly in-compressible with an inlet flow velocity set to $20 ms^{-1}$. However the study pertaining to this thesis employs the compressible RANS equations as the inlet flow velocity would be set to 0.2 Mach $\approx 68.04 ms^{-1}$.

Although the flow in the validation case has a Reynolds number of 1 million and simulations that will be performed for ground effect studies have a higher Reynolds number of about 10 million, the $k-\omega$ SST turbulence model can still be considered the best. This is because by validating at a lower Reynolds number and inlet velocity where separation occurs easily, the same turbulence model would work just as good if not better for cases pertaining to a higher Reynolds number [20] where separation is delayed. With regard to using the turbulence model for compressible flow, at Ma < 5, the Morkovin hypothesis states that for boundary layers, the effect of density fluctuations on the turbulence is small [53]. Based on this hypothesis, the additional turbulence terms which arise as a result of both time and Favre averaging of the boundary layer equations can be treated as those for constant physical properties. Both Vos et al [80] and Schlichting et al [32] have stated and shown respectively that the use of these models offer good predictions even in highly compressible flow with fluid velocities that are as high as 5 Mach.

4.2. Domain Sensitivity

A key part of any CFD simulation is the determination of the domain size and the positioning of the FV within this domain. Determining the right proximity of the computational domain wall boundaries to the half model of the FV is essential because of its influence on the simulations results. These boundaries can affect the simulation in two different ways:

- In case of external aerodynamics, if the size of the domain is too small, the interaction between the flow over the wing and the boundary condition that is applied on a domain wall will influence the forces acting on the geometry and the different flow features, structures and phenomena that are produced.
- If the size of the domain is extremely large, the number of cells required to appropriately fill the domain could significantly increase inflicting a higher computational cost.

This sensitivity analysis was done by shrinking a very large domain consecutively to test the effect of the boundaries. To obtain an optimized domain size, the distance between the slip walls which correspond to the boundaries that make up the upper surface of the domain and the surface opposite to the symmetry plane was varied between $8.361b$ and $1.672b$ as shown in figure 4.6 below.

The flow conditions used for the domain sensitivity study are the exact conditions that are applied for studying the influence of ground effect on the FV. For this analysis,

- The FV was oriented at an angle of attack equal to 20° at a height of $0.25b$ away from the ground.
- The inlet velocity was set to 68.04 ms^{-1} and a grid with a $y^+ = 0.9$ was used for meshing.

Now since the aim of this analysis is to study the influence of the 'size of the domain and its boundaries' on the flow field, the mesh included a 'body of influence' that had a fixed level of refinement which was maintained for all five domains being tested. By doing so, any differences in the fluid flow will be caused only due to the change in the size of the domain and the interference with the boundary walls. This body

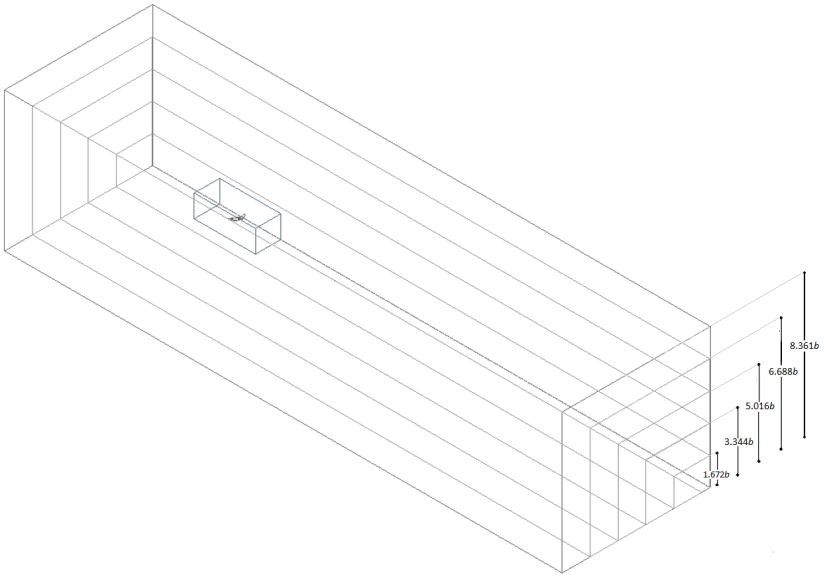

Figure 4.6: Comparison of the different domains created for the sensitivity analysis

of influence had a length of $5b$ and a width and height of $2.66b$ as mentioned in section 3.2. The size of the elements within the body of influence was set to 0.0482 meters.

Figures 4.7a, 4.7b and 4.7c show the percentage change in the lift, drag and pitching moment coefficients calculated at each of the varying domain lengths with respect to the calculated values pertaining to the largest domain with a length of $8.361b$.

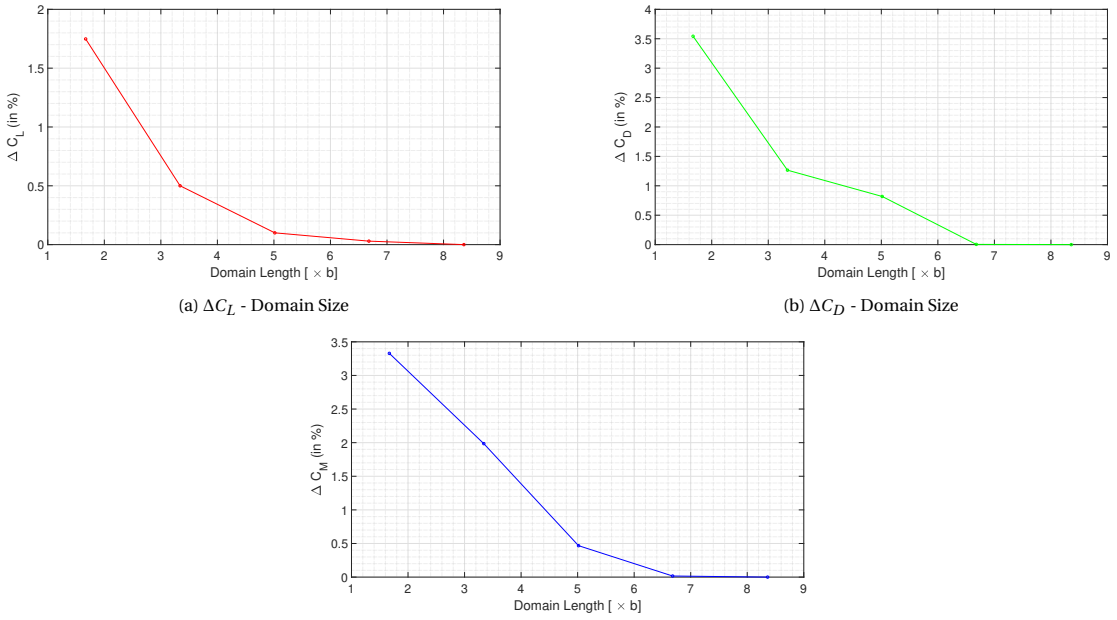

(a) ΔC_L - Domain Size

(b) ΔC_D - Domain Size

(c) ΔC_M - Domain Size

Figure 4.7: Change in aerodynamic coefficients corresponding to the size of the domain

A large reduction in the percentage change of all three coefficients is seen from the smallest to the largest domain that is tested. The rate of change of all these values reduce as the size of the domain increases particularly at after a domain length of $5.016b$. A change of $< 0.1\%$ should be considered as the criteria that must be met to deem a solution insensitive to the boundary conditions applied on the walls of the domain.

Based on these results it can be seen that a domain size of **6.688b** is the ideal domain size that should be used for conducting ground effect analysis of the FV.

The results have all been tabulated in table 4.2

Domain Size	ΔC_L (%)	ΔC_D (%)	ΔC_M (%)
$1.672b$	1.74829	3.54263	3.32795
$3.344b$	0.50010	1.26558	1.98564
$5.016b$	0.10010	0.81850	0.46767
$6.688b$	0.02960	0.00396	0.01628
$8.361b$	0	0	0

Table 4.2: Comparison of calculated aerodynamic coefficients for different domain sizes

4.3. Convergence Monitoring

The discretization of the governing equations of fluid flow yield a linearized set of algebraic equations that are solved by an iterative method. Appropriate convergence conditions that indicate when a solution is to be terminated need to be defined. For this reason the residuals of continuity, velocities in x,y,z directions, energy and the eddy viscosity were all monitored for every single case.

Figure 4.8shows the convergence history for the case of the FV in ground effect at an $\alpha = 20°$ and a h/b = 0.25. The simulation was allowed to run until all residuals reached a limit of 1e-10

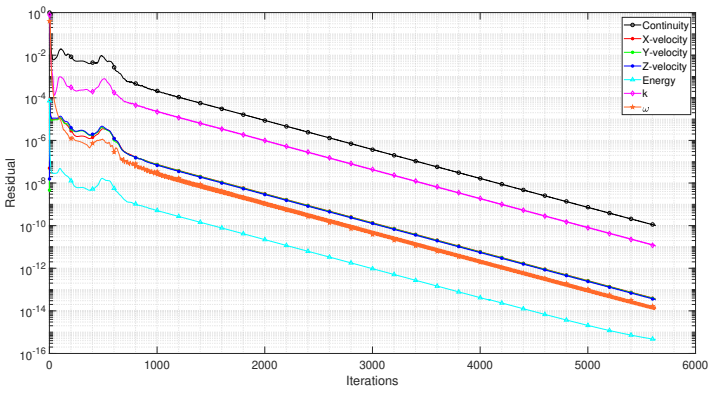

Figure 4.8: Comparison of the different domains created for the sensitivity analysis

After 5630 iterations, the convergence history shows that the residuals of continuity amounted to $9.962e^{-11}$, the residuals of velocity were approximately $3.5e^{-14}$, that of turbulent kinetic energy was approximately $1.15e^{-11}$ while the residuals of specific dissipation rate was $1.34e^{-14}$ and the residuals of energy had converged to $4.5e^{-16}$.

Now although residuals do give a good idea of the convergence of the solution, they are insufficient. For this reason to determine if a steady state has been attained the forces of lift, drag and moment are also monitored in addition to the above mentioned quantities. In this study, a solution is considered to have achieved a steady state when the error computed with respect to the forces at the last solved iteration , F_{end} is equal to 10^{-6}. This error is estimated by plotting equation 4.2

$$\epsilon = \left| 1.000001 - \frac{F_i}{F_{end}} \right| \tag{4.2}$$

F_i is the force acting on the FV corresponding to the i-th iteration. The computed errors of the lift, drag and pitching moment have been presented in figure 4.9.

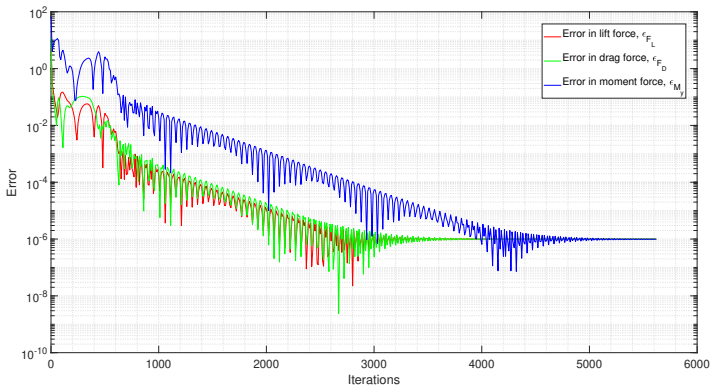

Figure 4.9: Comparison of the different domains created for the sensitivity analysis

It can be seen that converged values of lift, drag and moment are achieved after roughly 5000 iterations. The corresponding residual of the continuity equations after the same number of iterations is approximately $7.1e^{-10}$

Based on these estimations of error and the representation of convergence history the following criteria were used to determine if a solution has fully converged :

- The monitored forces converge to a specific value that does not vary upto the sixth decimal place.
- The continuity equation residual is at least equal to $1e^{-9}$

4.4. Grid Dependance

Although a CFD simulation can converge given a specific grid, in a parametric study such as this, it must be ensured that the solution is also independent of the mesh resolution. On one hand a coarse mesh can result in erroneous results and on the other hand an extremely fine mesh can drastically increase the computation time. Therefore a mesh that offers a balance between the accuracy of results and computation time is required. To determine this optimal mesh, a convergence study must be performed.

In order to study the sole influence of mesh resolution on the solution, the element size within the BOI was varied between 0.024 m to 0.096 m. A constant first cell height of 2.5×10^{-6} corresponding to a y^+ of 0.8 was used. The properties of all three grids generated and tested are listed in table 4.3

Grid #	**Grid**	**y$^+$**	**First cell height** μm	**Growth rate**	**Element size** m	**Number of Cells** $x10^6$
1	Coarse	0.8	2.5	1.2	0.096	15.06
2	Medium	0.8	2.5	1.2	0.048	21.54
3	Fine	0.8	2.5	1.2	0.024	30.50

Table 4.3: Specification of the different grids

The total number of cells were 15, 21 and 30 million respectively for each of the three different grids. The FV was oriented at 6 different angles of attack between $\alpha = -5°$ and $\alpha = 20°$ at a height of $0.15b$ from the ground. The calculated lift, drag and pitching moment coefficients with respect to α obtained from using the three different grids are shown in figures 4.10a, 4.10b and 4.10c.

It can be seen that all three grids are mesh independent upto $\alpha = 10°$ when comparing the lift coefficient vs α curve in figure 4.10a. Deviations between Grid 1 and Grids 2 and 3 start to arise from $\alpha > 10°$ on wards. All three grids show close values between $\alpha = 10°$ and $\alpha = 15°$. Grid 1 is seen to over predict the values of C_D by about 57% to the values calculated by Grids 2 and 3. while above 15°, Grid 1 under predicts the drag coefficient. For the entire range of α, grids 2 and 3 present C_D values that don't deviate from each other a lot with maximum deviation of 8.7% seen at $\alpha = -5°$.

In comparison to the lift and drag coefficient curves, the curves associated to the pitching moment coefficient indicate that the values of C_M are dependent on the grid refinement. Figure 4.10c shows that up to

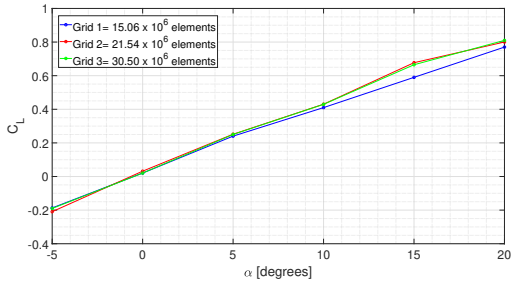

(a) C_L calculated by the different grids

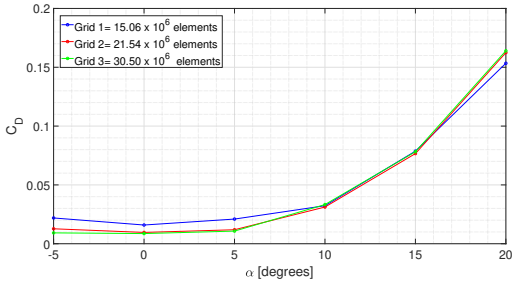

(b) C_D calculated by the different grids

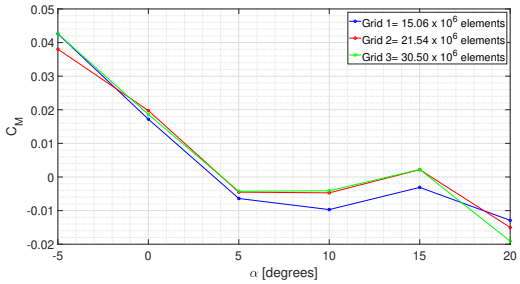

(c) C_M calculated by the different grids

Figure 4.10: Comparison of aerodynamic coefficients calculated by the different grids

$\alpha = 5°$ the values of C_M are relatively grid independent with deviations picking up at the 10° point. All three grids regardless of their refinement display a similar trend. Up to $\alpha = 15°$, grids 2 and 3 show C_M values that are very similar to each other. Although all 3 grids predict a sudden node down moment after $\alpha = 15°$, they display significant deviations from each other, implying that with regard to C_M, post $\alpha = 15°$, the grids 2 and 3 are mesh dependent.

In conclusion, it is quite evident from the observations made and the curves plotted in figure 4.10 that grid 2 with 21.54 million cells best satisfy the requirements of being mesh independent.

4.5. Mesh Quality

One of the most important steps in 3D grid generation to ensure faster convergence, a good illustration of the flow physics and minimum diffusion of the solution is the process of carrying out a check on the overall mesh quality, assessing its flaws and if needed improving this quality[55].

This mesh quality can be evaluated based on a system of metrics. In this study, the orthogonality, skewness, cell volume and aspect ratio have been chosen as properties of the mesh that if assessed would best describe the overall quality.

It must be noted that outlined below is the mesh quality report obtained by employing the refinements to the body of influence and far field that were recommended from the grid dependence study that was carried out and presented in section 4.4.

Orthogonality is a measure of the degree of closeness that angles between adjacent element faces/edges are to a selected optimal angle depending on the relevant topology [8].

It can be determined by first calculating, for a volumetric cell, the minimum among,

$$\frac{\vec{A}_i \cdot \vec{f}_i}{|\vec{A}_i||\vec{f}_i|} \quad \text{and} \quad \frac{\vec{A}_i \cdot \vec{c}_i}{|\vec{A}_i||\vec{c}_i|} \tag{4.3}$$

where, i refers to each face of a cell, A_i is the face area vector, $\vec{f}_i$ is the vector from the centroid of the cell to the centroid of that face and $\vec{c}_i$is the vector from the centroid of the cell to the centroid of the adjacent cell that shares the same face[81]. The orthogonal quality of a cell ranges between 0 and 1, where it is considered to be excellent for a value greater than 0.9 and unacceptable for values less than 0.1 [55].

The entire spectrum that is used to assess the orthogonal quality of the elements of the mesh is given in table 4.4

Table 4.4: Spectrum of Orthogonal quality mesh metric [8]

Range	Quality
0 - 0.001	Unacceptable
0.001 - 0.14	Bad
0.15 - 0.20	Acceptable
0.20 - 0.69	Good
0.70 - 0.95	Very Good
0.95 - 1.00	Excellent

The histogram presented in figure 4.11 displays the percentage of elements plotted against their corresponding range of orthogonal quality.

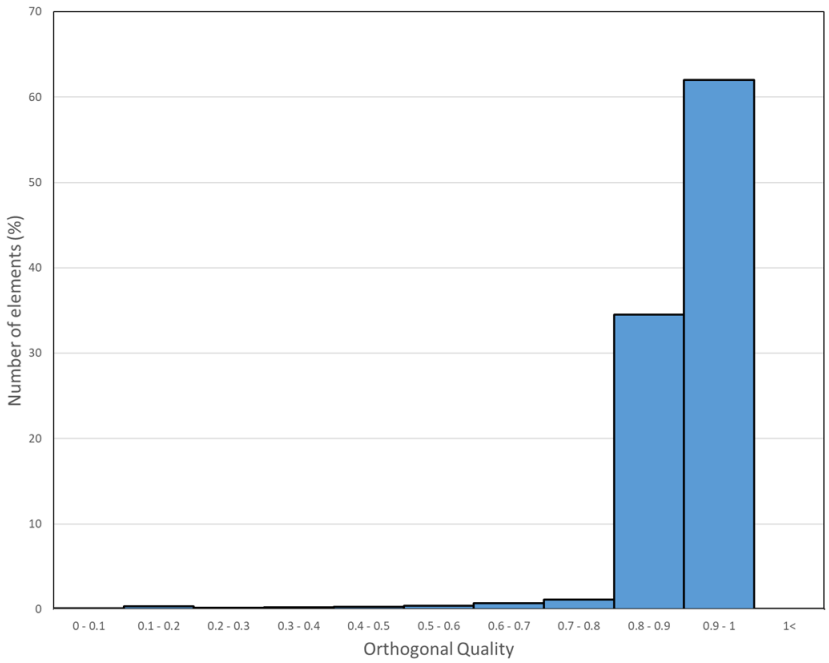

Figure 4.11: Distribution of orthogonal quality of all elements in a mesh

It is observed that 96.5% of all elements lie within the ranges of very good and excellent i.e. with an orthogonal quality ranging between 0.8 and 1, while only 0.1% of all elements have poor orthogonal quality that ranges between 0 and 0.1.

The property of skewness is another important parameter that is used to assess the quality of a mesh. Measured between 0 and 1, it determines the degree by which the size of the cell differs from the optimal cell size. A value of 0 indicates that a cell is equilateral while degenerate cells are characterized by a value of 1 [8]. When applied in case of a 3D cell, diagonal skewness is defined as the ratio of the lengths of two body diagonals subtracted from 1 to always provide a non negative value [13].

$$\text{Cell skewness} = 1 - \frac{\text{length of shorter body diagonal}}{\text{length of longer body diagonal}} \tag{4.4}$$

The contours of diagonal skewness 1 is presented in figure 4.12. From the figure it can very clearly be seen that the overwhelming majority of all the cells within the domain lie within a skewness range of 0.1 and 0.45. When comparing with the skewness spectrum presented in table 4.5 provided by ANSYS [8], these cells are recognized as ranging between 'good' and 'excellent'

Table 4.5: Spectrum of Mesh Skewness [8]

Skewness Range	Quality
0	Equilateral
0 - 0.25	Excellent
0.25 - 0.5	Good
0.5 - 0.75	Fair
0.75 - 0.90	Poor
0.90 - 1.00	Bad
1.00	Degenerate

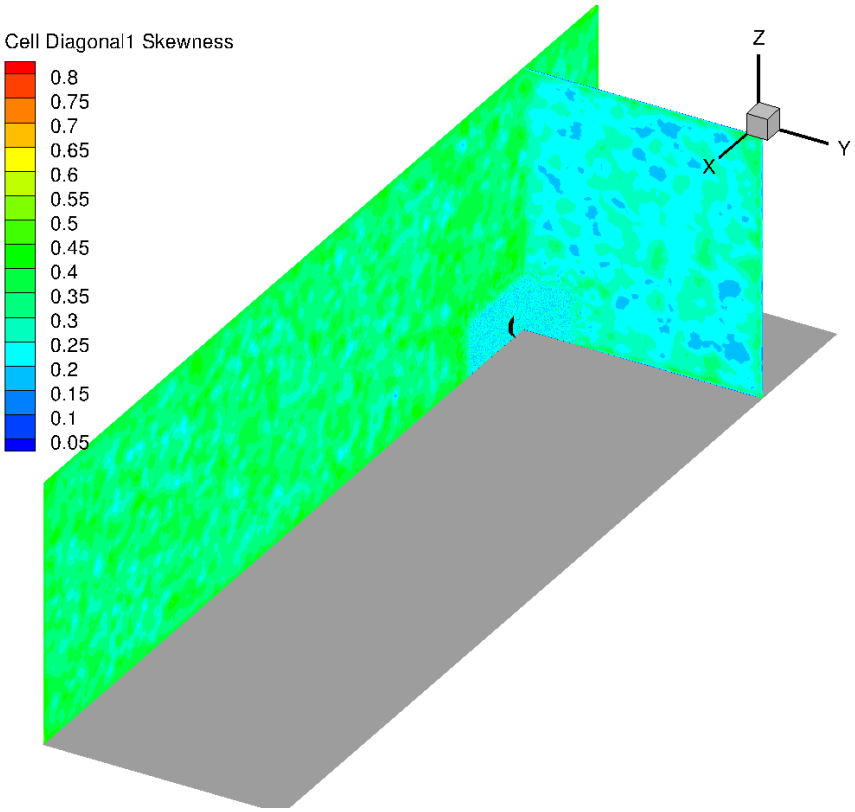

Figure 4.12: Contours of Diagonal Skewness 1 plotted on two planes at (1,0,0) and (0,0.1,0). Case: FV IGE at a $h/b = 0.5$ and $\alpha = 5^{\circ}$

To capture the flow phenomena in the wake of the FV with sufficient resolution and accuracy, emphasis was made while performing the grid dependency study to ensure that the elements which together make up the entire body of influence had very low values of skewness. As a result, a concentration of cells with a skewness range between 0.1 and 0.2 approximately can be seen in figure 4.12 within the body of influence

The extent to which a cell is stretched is given by its aspect ratio and is calculated using equation 4.5. Since polyhedral cells have been used, the maximum aspect ratio of all faces of a given cell are calculated [13]. Cells are generally supposed to have a low aspect ratio with an optimum value of 1 [22]. This is however not necessary to be employed in all regions of the domain as elongated cells can be used in the inflation layers to capture the turbulent boundary layer that is produced over the surface of the wing. However, care must be taken to ensure that these high aspect ratio cells are able to accurately capture the curvature of the wing and that there is no sudden change in the aspect ratio of cells neighboring each other.

$$\text{Aspect Ratio, AR} = \frac{(\text{Maximum edge length})^2}{Area} \tag{4.5}$$

Roughly 38.2% of all the cells in the domain had an AR ranging between 6-10 while only 8.6% of the cells had AR values between 1 and 2. Cells closest to the boundary layer near the walls of the FV had a maximum

aspect ratio ≈ 100 and because of their extremely small thickness account for nearly 51.76% of all the cells in the domain. As previously mentioned, these high aspect ratio cells within the boundary layer near the walls of the FV are less problematic as the flow velocity normal to the wall in this region is relatively low.

Iso-surfaces of the mesh at three specific cell volumes equal to 10^{-10}m^3, 10^{-5}m^3 are shown in figure 4.13.

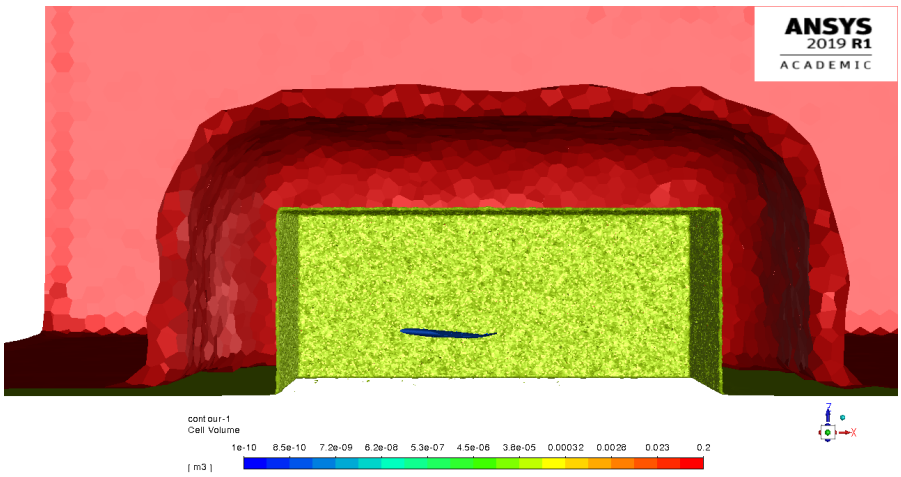

Figure 4.13: Iso-surfaces of cell volumes equal to 10^{-10}m^3, 10^{-5}m^3 and 0.2m^3. Case: FV IGE at a $h/b = 0.5$ and $\alpha = 5°$

This figure helps to highlight the density of cells in the vicinity of the wing. As can be seen, majority of the cells that make up the mesh are those cells that have the least volume and are used to resolve the turbulent boundary layer around the wing along with creating a smooth transition away from the wing to the wake region and the far field. The minimum cell volume is equal to 7.5138×10^{-13}m^3 while the maximum cell volume is about 0.956842m^3

4.6. Reynolds Number Verification

Since the Reynolds number that was selected for this thesis was set at 10 million, and is almost 10 times lower than the Reynolds number of the full scale model, a short test was carried out by running two cases - at a slightly higher Reynolds number (20 million) and at a lower Reynolds number (5million).

The percentage change in the drag forces calculated showed a 1.136% difference in the calculated lift and drag coefficients with the 20 million Reynolds number case. At the lower Reynolds number a greater change in the calculated drag coefficients is seen amounting to 2.366%. Based on the evidence provided above in Section 3.1 and the test that was conducted, it was considered acceptable to use a Reynolds number of 10 million for the remaining simulations.

5

Results and Discussions

The results obtained based on simulations that were carried out from the conclusions of the verification and validation studies are discussed elaborately in this chapter. Beginning with a comparison of the aerodynamic coefficients, the results aim to explain the influence that ride height(h/b) and the angle of attack, α have on the performance of the FV. Pressure contours both on and off surface, distributions of pressure coefficients, velocity contours, visualization of vortices and a near wake analysis of the FV in ground effect have all been reported and explained to study the behavior of the FV and its downstream wake evolution. These illustrations when correlated with the force and moment coefficients will help in the investigation of the flow behavior.

5.1. Comparison of Aerodynamic Coefficients IGE

Figures 5.1 to 5.3 present the lift, drag, lift to drag ratio and moment coefficient data respectively, for the simulations that were carried out with fluid properties as given in table 3.1. The simulations were carried out at four different heights for a range of α varying between $-5°$ and $20°$. These results are then compared with those of when the FV is OGE i.e. $h/b = \infty$.

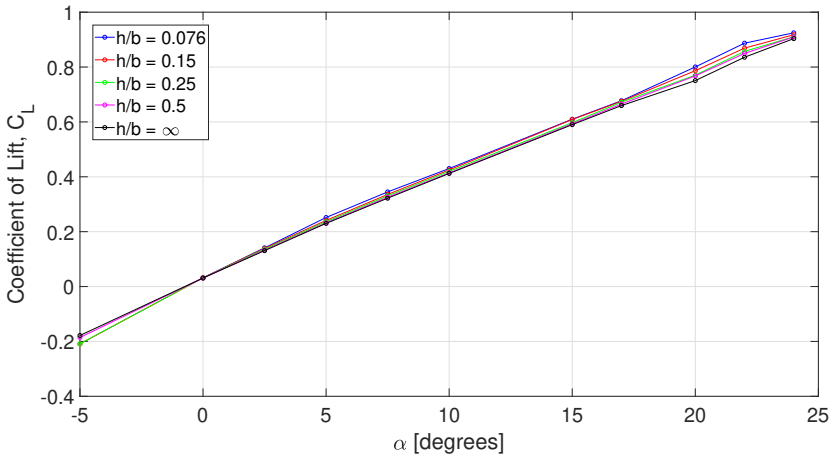

Figure 5.1: Variation in lift coefficient, C_L with height

Figure 5.1 shows the variation in the lift coefficient when plotted against the angle of attack α. An immediate takeaway from this figure is that the distance to the ground has an effect on the magnitude of the lift coefficient but not on the general trend that is followed with increasing α. Regardless of the height from the ground, the lift that is generated is seen to increase rather linearly. Also observable is that for all heights from the ground, there is no large difference between th forces of lift when $\alpha = 0°$. In fact, it is seen that as α increases the differences in the magnitude of the lift coefficient also increases. This phenomenon can be explained by using the illustrations of the effects of downwash in figure 2.9a and how ground proximity influences the lift vector. At $\alpha = 0°$, the lift vector is already very close to the perpendicular direction which is the

ideal case, as the relative direction of the airflow to the wing is equal to the free-stream direction. The shift in the lift vector that is expected when in ground proximity therefore does not have any significant impact on the increase of the lift force irrespective of the height from the ground. Since the FV is not a symmetrical wing with a varying camber and twist along its span, a $C_L \approx 0.03$ is obtained at $\alpha = 0°$.

At every positive angle of attack, the value of the lift coefficient is seen to increase as the FV moves from a $h/b = \infty$ to a $h/b = 0.0769$. Reasons for this increase will be addressed in subsequent sections of this chapter. When $\alpha = -5°$, the wing produces negative lift- "down force". The magnitude of this down force is directly related to the height of the FV from the ground, with the highest negative lift (= −0.2086) produced at $h/b = 0.15$. This value of C_L decreases as $h/b \to \infty$. Simulations pertaining to $\alpha = -5°$ and a $h/b = 0.0769$ were not feasible owing to the geometry of the FV which causes it to cut through the ground plane.

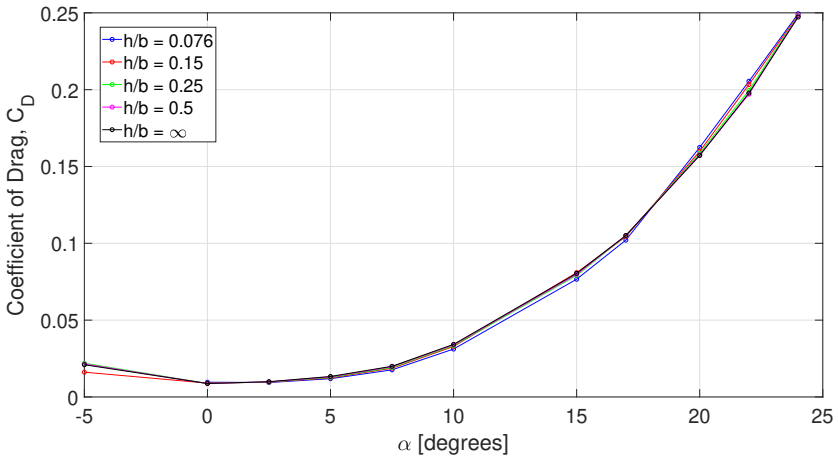

Figure 5.2: Variation in drag coefficient, C_D with height

The overall coefficient of drag of the FV calculated at different angles of attack and at different heights from the ground is presented in figure 5.2. The values of the drag coefficient are seen to increase with α similar to the way C_L increases with α in figure 5.1. What is characteristic of these curves is that at higher angles of attack, the rate at which drag increases, represented by the slopes of the curves also increase. Drag in case of in-compressible flows are broadly divided into profile drag and induced drag given by equation 5.1.

$$C_D = C_D + C_{D,i} \tag{5.1}$$

Profile drag is independent of the lift of the wing and is known to increase because of an increase in the projected area and thickness of the boundary layer. Induced drag, given by equation 5.2, is proportional to the square of the lift coefficient. The increase in drag that is seen with increasing α is attributed to an increase in both of these.

$$C_{D,i} = \frac{C_L^2}{\pi AR e} \tag{5.2}$$

The drag polar of the wing, K, given by $1/(\pi AR e)$ is affected by both the aspect ratio (AR) and the Oswald efficiency (e).

By differentiating C_D in equation 5.1 with C_L^2,

$$\frac{dC_D}{dC_L^2} = K \tag{5.3}$$

This implies,

$$\frac{dC_D}{dC_L^2} = \frac{1}{\pi AR e} \tag{5.4}$$

By creating a polynomial fit for the different coefficients of lift and drag for each height above the ground, it is possible to compute the drag polar, K and the Oswald efficiency (e). This is tabulated in table 5.1

As can be seen, the Oswald efficiency decreases and the drag polar increases as $h/b \to \infty$. Now the FV was designed with a low aspect ratio (≈ 2.394 for the half wing) and therefore the induced drag will account for a

Table 5.1: Percentage change in L/D ratios with respect to height

h/b	K(Drag Polar)	Oswald Efficiency
0.0769	0.260	0.490
0.15	0.276	0.478
0.25	0.285	0.463
0.50	0.286	0.462
∞	0.294	0.448

major portion of the total drag produced. At $h/b = 0.0769$, the drag polar, K reduces by 11% when compared to the drag polar of unbounded flow. This verifies that ground proximity does reduce the induced drag of the FV. Interesting observations can be made from figure 5.2 and by using table 5.1:

- The calculated drag coefficients appear to converge to a single value at $\alpha = 0°$. This is because the induced drag of the FV regardless of it's height from the ground remains relatively constant, accounting for only about 2.7% of the total drag.
- Between $\alpha = 2.5°$ and $\alpha = 18°$, the values of C_D decrease as the height of the FV from the ground reduces. This can be explained by the distortion of the downwash by the ground resulting in a reduction of the induced drag as shown by table 5.1 and therefore reducing the overall drag of the wing.
- For $\alpha > 18°$, there is a switch that is observed where cases closest to the ground exhibit higher drag than cases that are away from the ground and also OGE. A better understanding of this can only be made by visualizing the flow and understanding its interaction between the FV and the ground.

The calculated lift to drag (L/D) ratios for different α at different heights from the ground is presented in figure 5.3. As would be expected from looking at the lift and drag curves in figures 5.1 and 5.2, the L/D curves fro cases IGE follow a similar trend to OGE cases with maximum lift capabilities of the wing seen at $\alpha = 5°$ and $\alpha = 7.5°$. For positive α, lower ride heights have a positive effect on the L/D ratio with maximum values obtained for all angles of attack at $h/b = 0.0769$. From figure 5.3, it is interesting to see that there is an almost exponential increase in the rate at which the L/D ratios increase with a reduction in height.

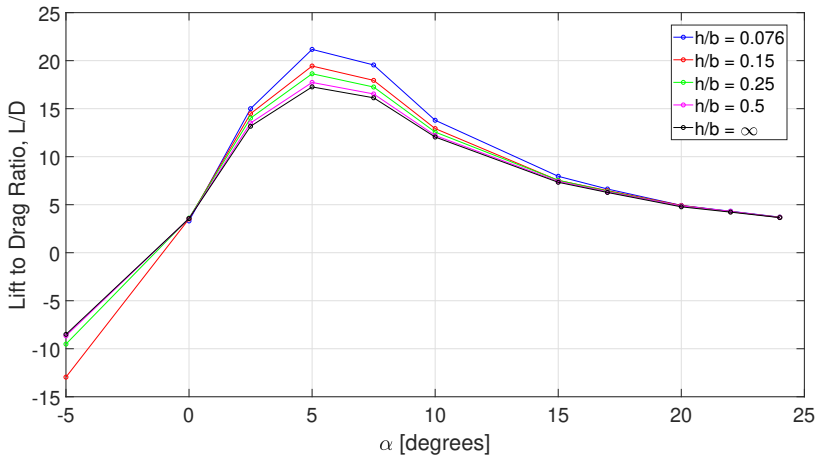

Figure 5.3: Variation in lift to drag ratio, C_M with height

For the sake of simplicity, the percentage change in L/D ratios for $\alpha = 5°$ at each height with respect to the preceding height is shown in table 5.2.

The percentages from this table also substantiate Gudmundsson's [34] statement that ground effect begins to influence an aircraft from a height that is equal to half its wingspan. The L/D ratios calculate at $h/b = 0.5$ has only a 2.7% change with respect to OGE while when closest to the ground, an approximately 21% increase in L/D is obtained. At very high angles of attack, $\alpha > 20°$ the L/D ratios appear to converge to relatively constant values that don't vary too much with respect to the height. The higher increase in drag as a

Table 5.2: Percentage change in L/D ratios with respect to height

h/b	**Percentage Increase** %
∞	-
0.50	2.72
0.25	5.01
0.15	4.30
0.0769	8.92

result of being at such a high α compensates for the increase in lift that is expected when IGE. When $\alpha = -5°$, the negative lift to drag ratio is seen to be consistent with the C_L vs α curve. The highest (negative) lift to drag ratio is produced when closer to the ground.

Figure 5.4 presents the variation in the pitching moment coefficient with a change in α. Again, the change in ride height does not influence the overall trend in the moment curve. The height from the ground does affect the magnitude of the moment. For all positive angles of attack up to $\alpha = 18°$, the magnitudes of the moment coefficient increase with a reducing ride height. Favorable pitching moment characteristics i.e. ($\frac{dC_M}{d\alpha} < 0$) are observed for $-5° < \alpha < 7.5°$ and $\alpha > 17.5°$. This variation that is seen in the pitching moment can be explained by the change in the local lift distribution over the wing at different angles of attack. The stabilizing moment that is seen is as a result of the wing becoming nose heavy with an increase in lift towards the aft of the wing as this portion of the wing experiences a greater increase in lift being closer to the ground plane. Between 7.5° and 17.5°, $\frac{dC_M}{d\alpha} > 0$ because of a shift in the amount of lift that is generated towards the root of the wing from the aft section of the wing. This is further validated by pressure distributions for a range of α between $-5°$ and 20° in section 5.3. These pressure distributions will also explain in thorough detail why the longitudinal stability of the FV suddenly increases when closer to the ground which is contrary to the trend that is observed for all $\alpha < 18°$.

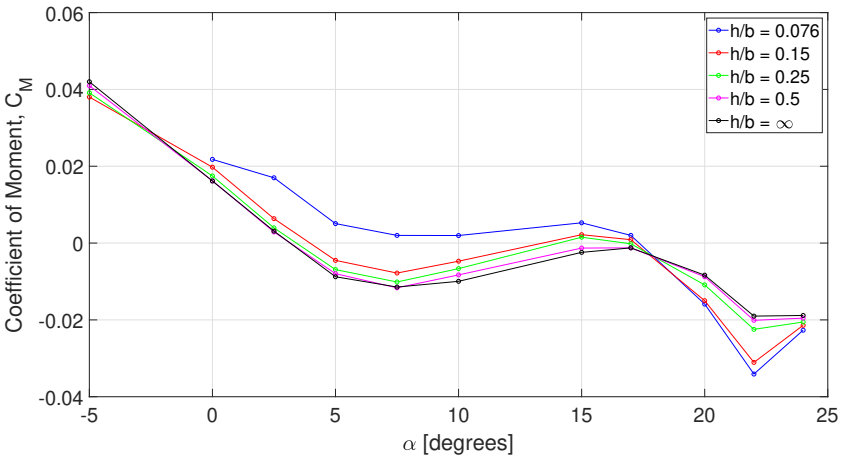

Figure 5.4: Variation in pitching moment coefficient, C_M with height

These lift, drag and pitching moment curves provide considerable information on the takeoff and landing behavior of the FV. The lift curve shows that the influence of ground effect allows the FV to touch down at an angle of attack that is one degree lesser i.e. $\alpha = 19°$ instead of $\alpha = 20°$. The lift to drag ratio at 20° is equal to ≈ 5 and given a thrust/weight ratio of 0.25, it is possible to still have a possible climb gradient. However, this is not the case when in a One Engine Idle (OEI) scenario. Therefore, $\alpha = 20°$ cannot be set as the maximum rotation angle during take off. For a positive climb gradient an L/D ratio equal to 10 is required, which corresponds to a maximum rotation angle of 13° from figure 5.3. The lift-off lift coefficient at $\alpha = 13°$ is approximately 0.56.

To highlight the reasons as to why the FV behaves the way it does when in ground proximity i.e. at different heights from the ground when compared to being out of ground effect, the pressure contours on the surface of the FV in unbounded flow and in ground effect at $h/b = 0.25$ and $h/b = 0.0769$ for $\alpha = 10°$ and $\alpha = 20°$ are presented in figures 5.5 and 5.6.

An immediate observation when looking at the pressure contours is that despite expecting an acceleration of the flow over the surface of the wing, no strong shock features can be observed. Both for $\alpha = 10°$ and $\alpha = 20°$, a similar trend on the suction and pressure sides of the wing can be seen when IGE and OGE. Both IGE and OGE, there exists a low pressure peak that is local to the leading edge of th wing which is followed by an increase in the pressure towards the trailing edge.

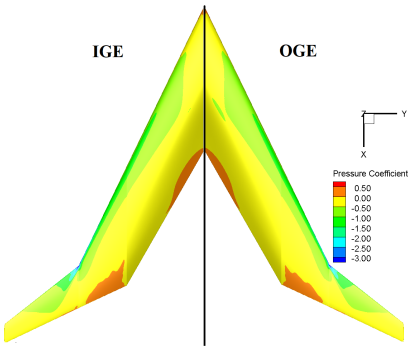

(a) Pressure contours on the upper surface when $h/b = 0.25$

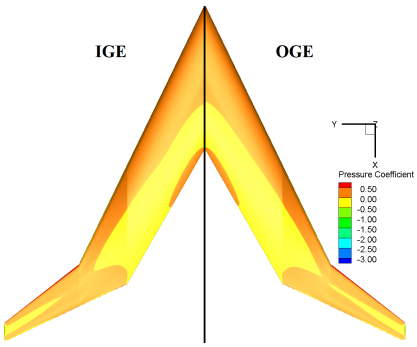

(b) Pressure contours on the lower surface when $h/b = 0.25$

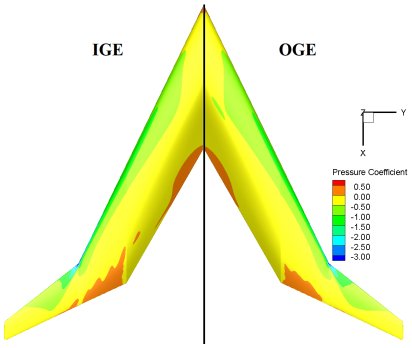

(c) Pressure contours on the upper surface when $h/b = 0.0769$

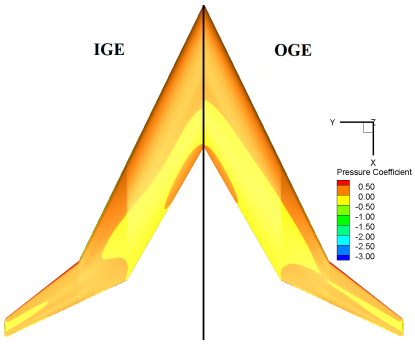

(d) Pressure contours on the upper surface when $h/b = 0.0769$

Figure 5.5: Comparison of pressure contours of the FV when IGE and OGE at $\alpha = 10°$

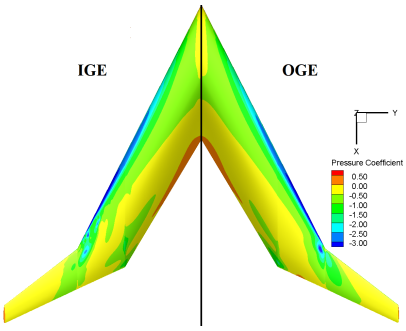

(a) Pressure contours on the upper surface when $h/b = 0.25$

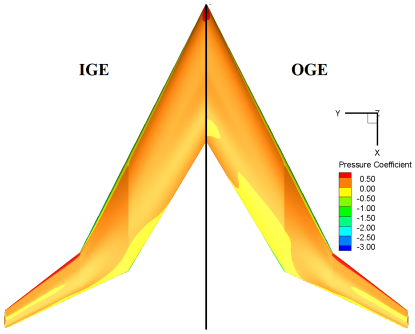

(b) Pressure contours on the lower surface when $h/b = 0.25$

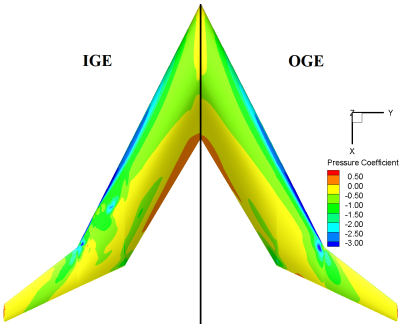

(c) Pressure contours on the upper surface when $h/b = 0.0769$

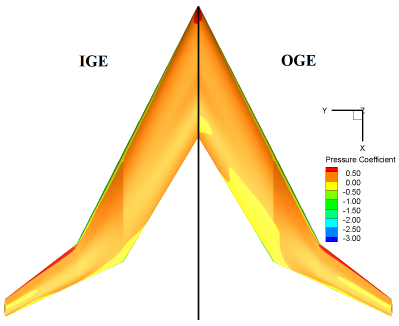

(d) Pressure contours on the upper surface when $h/b = 0.0769$

Figure 5.6: Comparison of pressure contours of the FV when IGE and OGE at $\alpha = 20°$

At low to medium angles of attack, large constant pressure regions are seen with adverse pressure gradients close to the trailing edges of the root and the outboard trunk of the FV. At $h/b = 0.0769$, these high pressure regions increase in area but their locations stay the same. On the pressure side of the wing, at $\alpha = 10°$, the distance to the ground dictates the size of the high pressure regions on the forward section of the wing. Towards the trailing edge, the pressure coefficient is equal to that on the upper surface at the same location. This is characteristic of wings that have a large thickness to chord ratio.

Now by increasing the angle of attack, the low pressure suction peaks at the leading edge further increases and so does the region on the wing that undergoes pressure recovery. From figures 5.6a and 5.6c, it can be seen that the region of low pressure peaks (indicated by blue contours) at the leading edge reduces with a decrease in ride height. The adverse pressure gradient is observed to stretch out over a longer section of the inboard trunk of the wing compared to when $\alpha = 10°$. The area that sees an adverse pressure gradient also increases as the ride height reduces. At high α, the low pressure regions located at the leading edge kink of the wing is seen to be directed further outward. This low pressure region along with the outboard trunk of the FV offers evidence of the presence of strong vortical structures being produced. For a better visualization of this, the iso-surfaces of Q-criterion are created and presented in section 5.4. When comparing the pressure side of the FV for both $\alpha = 10°$ and $\alpha = 20°$, it is evident that there is an overall increase in high pressure across the lower surface of the wing. In proximity to the ground, it can be seen that the flow is forced to remain attached and low pressure regions (represented by yellow contours in figures 5.6b and 5.6d) are reduced and instead replaced with regions of higher pressure.

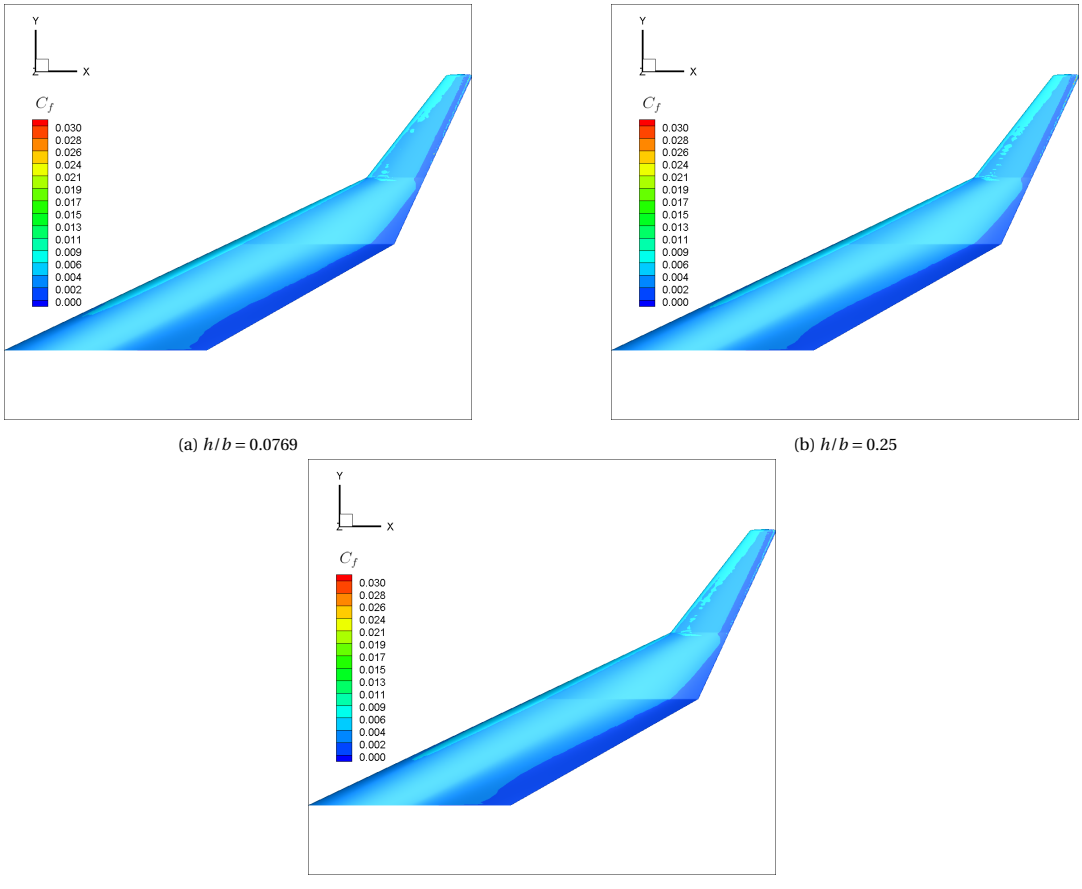

(a) $h/b = 0.0769$

(b) $h/b = 0.25$

(c) $h/b = \infty$

Figure 5.7: Contours of skin friction coefficient plotted at different heights from the ground and an $\alpha = 0°$

Figures 5.7, 5.8 and 5.9 show contours of skin friction coefficient (C_f). These contours were investigated in order to possibly identify regions of flow separation and the causes for it. When $C_f \to 0$, this would imply that the wall shear stress, $\tau_{\text{wall}} \to 0$ and the flow in this region is said to be separated. All three figures showcase characteristics similar to that of regular swept wings with high C_f values located at the leading edge of the wing which eventually reduce towards the trailing edge as the flow velocity reduces and a thickening of the

boundary layer occurs.

At 0° there is hardly any change in the distribution of the skin friction coefficient over the wing. Although the design of the FV has a high sweep angle, there is no indication of any 3D span-wise flow, in fact they show that the flow direction remains relatively straight.

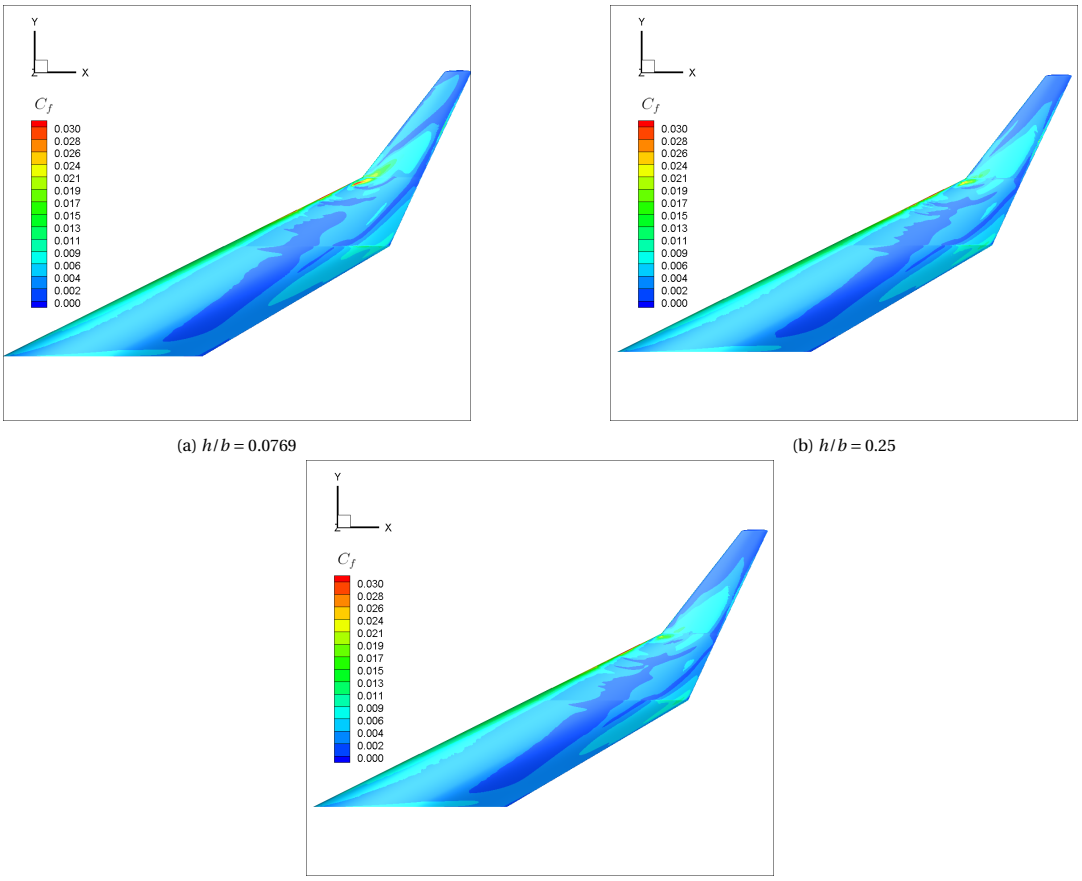

(a) $h/b = 0.0769$

(b) $h/b = 0.25$

(c) $h/b = \infty$

Figure 5.8: Contours of skin friction coefficient plotted at different heights from the ground at an $\alpha = 17°$

When the angle of attack increases to 17° however, a dramatic change in the C_f distribution over the wing can be seen. The C_f values about the leading edge have now increased from about 0.009 in case of $\alpha = 0°$ to about 0.019. At the leading edge kink of the wing, because of the acceleration of the flow that is caused by the change in the sweep angle, the skin friction values increase to an even higher value than when compared to that at the leading edge. When closest to the ground, this flow across the kink is seen to be at its highest acceleration as the local C_f in this region is the highest.

As is characteristic of highly swept wings, the phenomenon of vortex lift is noticeable from the contours of C_f in figures 5.8 and 5.9. For the case when $\alpha = 17°$, the plots suggest that there is a large vortex emanating from the leading edge kink which is directed outwards towards the tip of the wing.

As the height reduces in case of 17° and 24°, it can be seen that at the tips of the wing, the skin friction coefficient is not equal to zero which is representative of the existence of a tip vortex. In figure 5.8, the magnitude of C_f at the leading edge of the outer section of the wing is higher when closest to the ground which would mean that the wall shear stress at this location is large as well because of a greater change in velocity. This would result in the strengthening of the vortex as the height reduces.

The phenomenon of span-wise flow and vortex lift on the surface of the FV is quite clear when $\alpha = 24°$. A large vortex is generated at the root of the wing and propagates out towards the outer trunk of the FV while growing in size. The direction of the vortex that emanates from the leading edge kink is directed more and more outwards as the height reduces. The movement and production of these vortices have been visualized in section 5.4.

For a further illustration of the flow separation at low and high angles of attack at different heights from

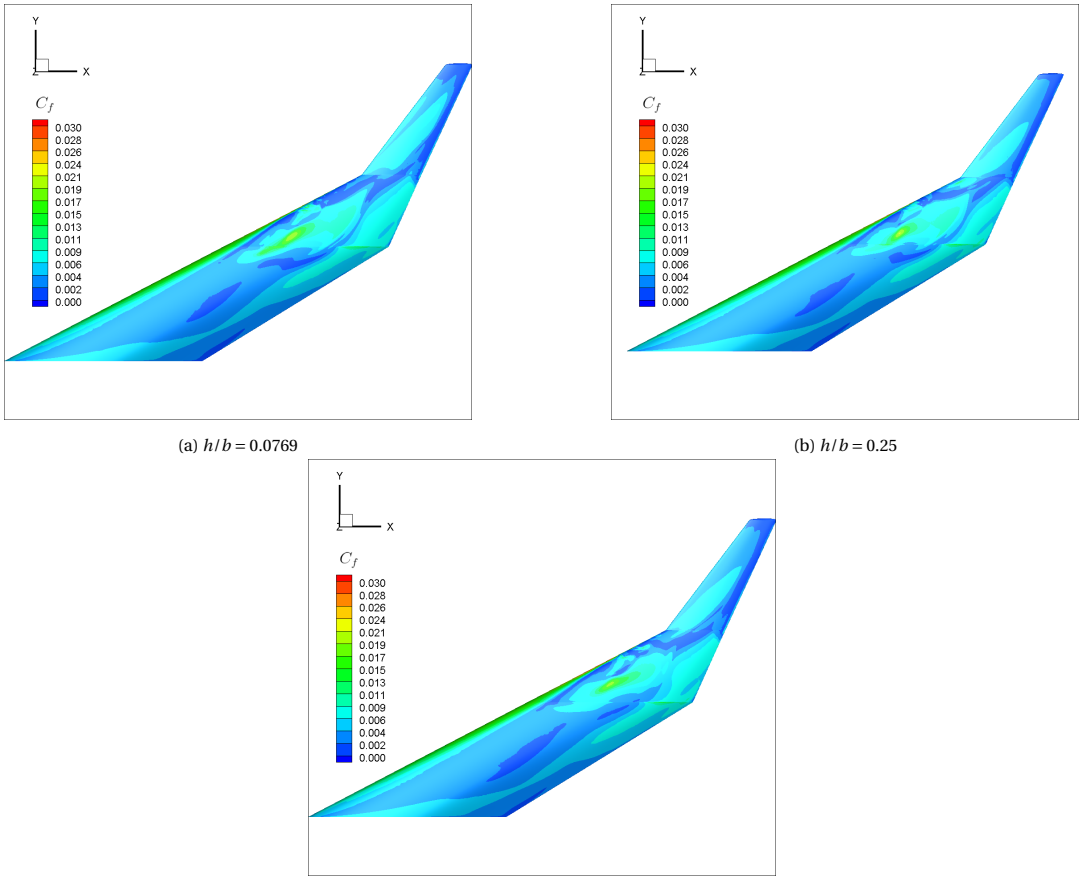

(a) $h/b = 0.0769$

(b) $h/b = 0.25$

(c) $h/b = \infty$

Figure 5.9: Contours of skin friction coefficient plotted at different heights from the ground at an $\alpha = 24°$

the ground, surface streamlines have been presented at $h/b = 0.0769$, $h/b = 0.25$ and $h/b = \infty$ in figures 5.12, 5.11 and 5.10 respectively. In the figures, when streamlines appear to converge and apprach a tangent of sorts then separation is said to have occurred and is called as a separation line. In figure 5.10a at low angles of attack i.e. 5°, the streamlines appear to move in the direction of the flow which is indicative of attached flow with a slight indication of span-wise flow outwards. Towards the trailing edge however, these streamlines then appear to converge to form a separation line.

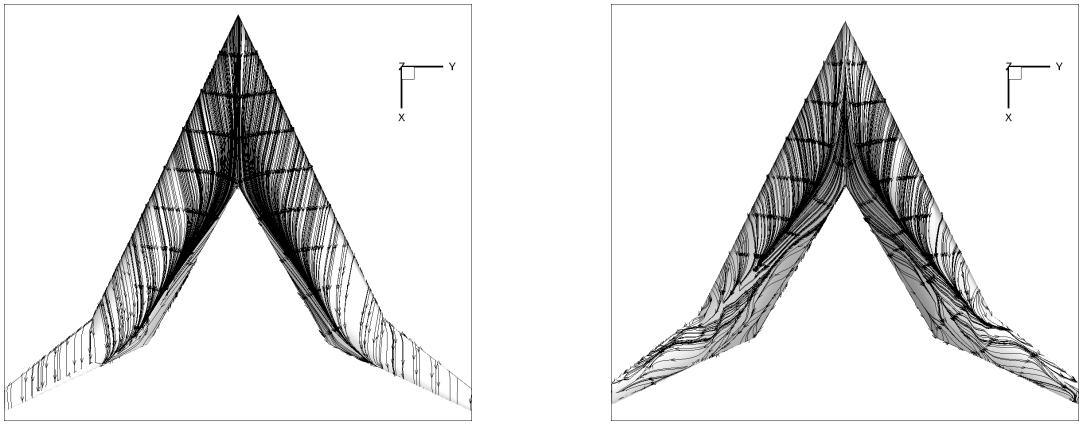

(a) $\alpha = 5°$

(b) $\alpha = 17°$

Figure 5.10: Surface streamlines over the FV for low and high angles of attack at $h/b = \infty$

Now when comparing this with streamlines on the FV when IGE, it can be seen that as the height reduces

there is a shift in the location of the separation line closer towards the leading edge. This would mean that as the height reduces, trailing edge separation occurs earlier along the mid-section of the wing. This is also representative of the skin friction coefficient contours that show values of C_F approaching zero at the trailing edge. Now when $\alpha = 17°$, the span-wise flow appears to move more aggressively outboard. At high angles of attack, the adverse pressure gradient increases with an increase in the thickness of the boundary layer. This causes separation much earlier as compared to at low angles of attack as seen by the location of the separation line. It is interesting to note that this separation line, irrespective of the height from the ground is furthest away from the leading edge of the wing at the root and closest at the kink. This implies that at high angles of attack, the flow stays attached longer at the roots and the least towards the kink. In unbounded flow, the separation line ends at the kink.

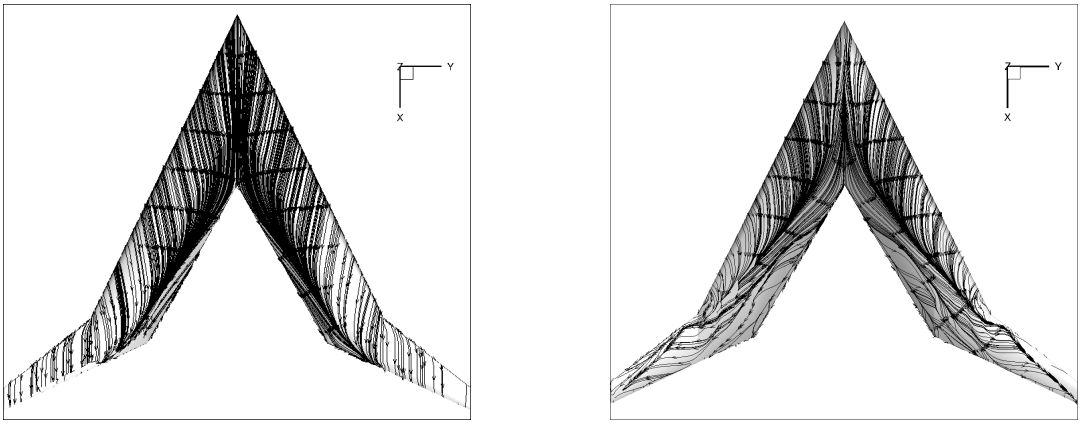

(a) $\alpha = 5°$ (b) $\alpha = 17°$

Figure 5.11: Surface streamlines over the FV for low and high angles of attack at $h/b = 0.25$

At $h/b = 0.25$ however the separation line is seen to continue all the way through to the tip of the wing. This would indicate that the proximity to the ground slightly delays the onset of flow separation at the leading edge of the outer trunk of the wing. At $h/b = 0.0769$, it is seen that there is a break in continuity of the separation line at the kink. This could be due to the acceleration of the flow at the kink as predicted in the skin friction contours. The flow also appears to stay attached at the outer trunk of the wing and towards the tip even more than when compared to the case at $h/b = 0.25$.

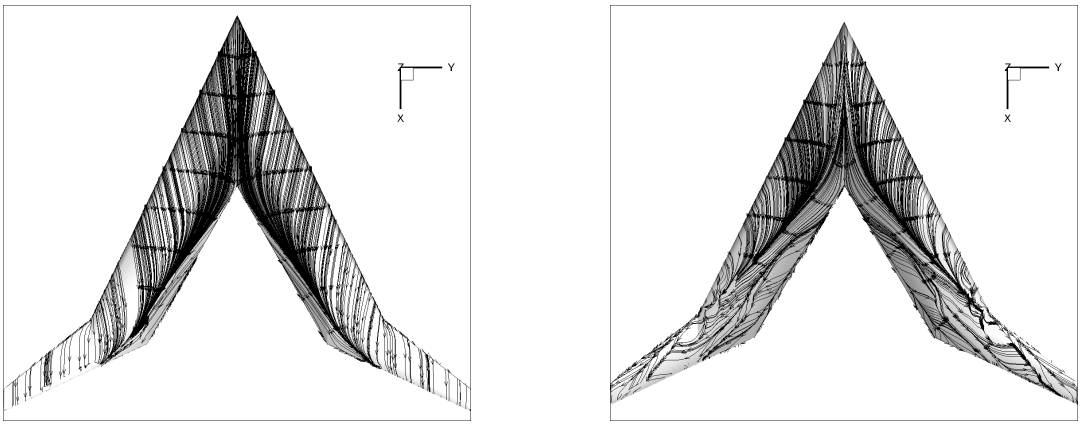

(a) $\alpha = 5°$ (b) $\alpha = 17°$

Figure 5.12: Surface streamlines over the FV for low and high angles of attack at $h/b = 0.0769$

Figures 5.13a and 5.13b were plotted to verify these conclusions that were drawn from the contours of skin friction coefficient and the surface streamline plots. Fluid path lines (also called streamlines) are plotted from an iso-plane located at a distance of $0.334b$ from the origin. These streamlines are colored with the magnitude of velocity. The FV in these plots have been oriented at $\alpha = 0°$ and $\alpha = 24°$ at a height of $0.0769b$ from the ground plane.

These streamlines very clearly show the acceleration of the flow over the upper surface of the wing in both cases. As indicated by the red colored regions, a substantial increase in the acceleration over the leading edge of the wing is seen for $\alpha = 24°$. The streamlines also show how the flow after acceleration over the leading edge, owing to the high sweep angle of the wing, is forced towards the outer trunk of the wing and tip in case of higher angles of attack. From these figures it is very interesting to see that the remarks made earlier about the flow over the wing using the C_f contours are correct. No span wise flow is seen when $\alpha = 0°$ and the flow appears to travel parallel to the stream-wise direction. Additionally, in case of very high angles of attack, the streamlines confirm the occurrence of a large vortex emanating from the leading edge kink of the wing.

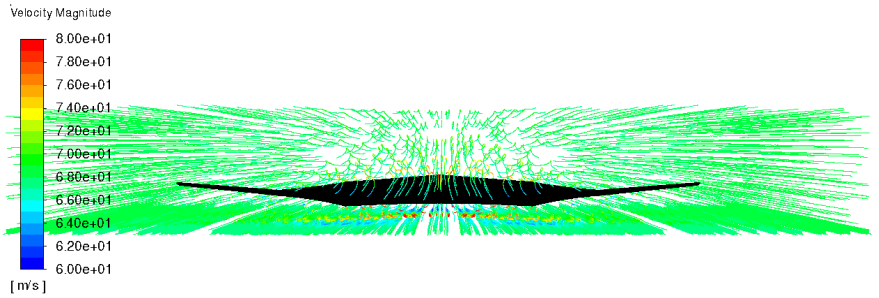

(a) $\alpha = 0°$

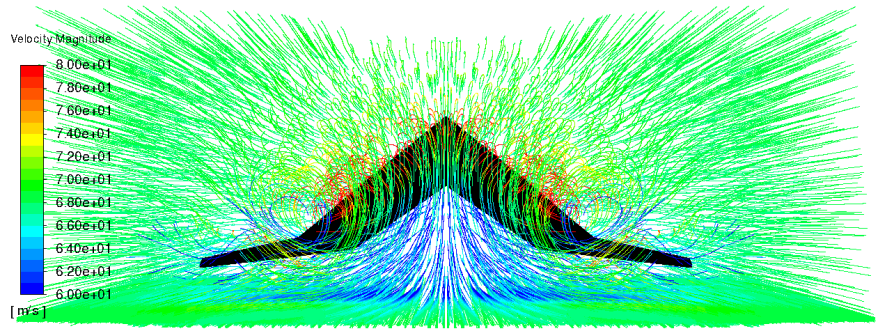

(b) $\alpha = 24°$

Figure 5.13: Flow streamlines over the FV for two extreme orientations with $h/b = 0.0769$

A fascinating visualization that the streamlines provide is the reduction in the flow velocity on the lower surface of the wing to magnitudes that are even lesser than the the free stream velocity. This slow moving flow can be associated to the high pressure regions that the coefficient of pressure contours show in figures 5.5 and 5.6 as height reduces. This is representative of chord dominated ground effect that was explained in section 2.2.1 where an increase in static pressure and a decrease in dynamic pressure is expected. An increase in pressure occurs because of the blockage effect. When in ground proximity a convergent passage is created between the wing and the ground causing the flow the slow down and thereby reducing the flux that crosses through this passage. As a result, part of this flux has no choice but to flow over the upper surface of the wing and thereby contributing to the increase in velocity and a further reduction in pressure on the suction side. This development of static pressure on the lower surface of the wing is termed as 'ram pressure' and can be be better illustrated by plotting Mach number contour distributions on the ground plane.

Figures 5.14 - 5.16 showcase this at three different heights that increase from the ground $h/b = 0.0769$, $h/b = 0.25$ and $h/b = 0.5$. At $h/b = 0.0769$ a large region of lower velocity flow is observed underneath the FV. Figures 5.15 and 5.16 show that as h/b increases to 0.25 and then to 0.5, this region of low velocity diminishes incrementally. This is because the convergent passage between the wing and the ground is growing in area and more flux is being allowed to flow through the passage. The interaction of the wings wake with the ground is also observed to reduce as the height increases with eventually little change in the variation of the velocity.

These distributions validate Staufenbiel et al's [82] statement that wings are said to experience a cushioning effect in ground effect. They also illustrate the ability of the FV to create such a strong low velocity region when very close to the ground which is advantageous in reducing the length of the runway that is required during a take-off.

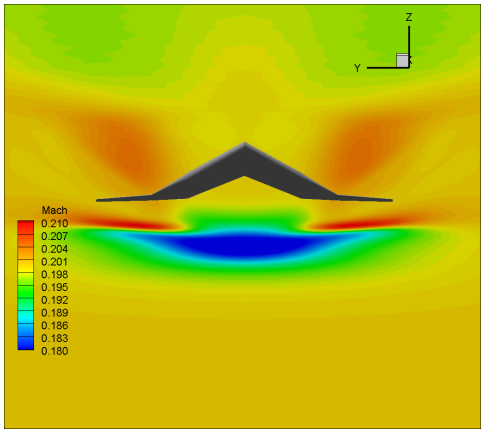

Figure 5.14: Mach distribution contours on the ground plane when $\alpha = 24^\circ$ and $h/b = 0.0769$

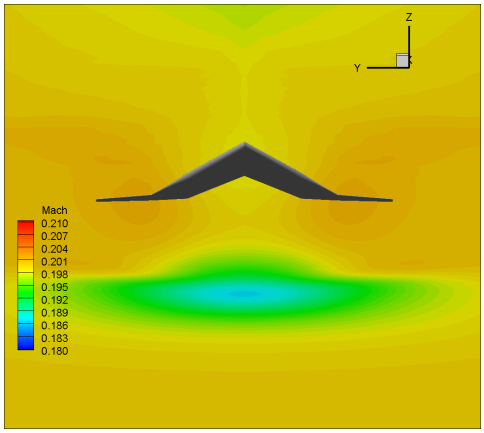

Figure 5.15: Mach distribution contours on the ground plane when $\alpha = 24^\circ$ and $h/b = 0.25$

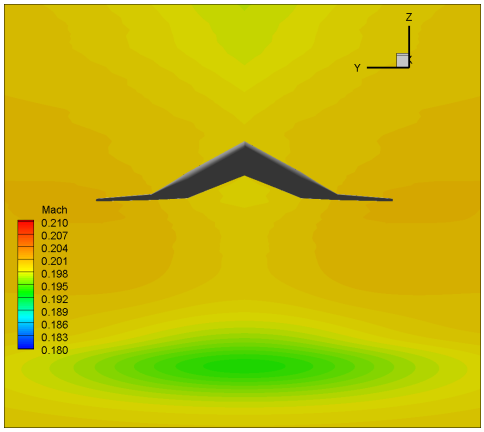

Figure 5.16: Mach distribution contours on the ground plane when $\alpha = 24^\circ$ and $h/b = 0.5$

5.2. Influence of Ride height

So far only a qualitative analysis of the flow phenomena over the FV has been discussed. Being able to plot the distribution of the pressure coefficient across different span wise locations of the wing would help in a more extensive understanding of the flow over the wing and the influence of the ground proximity to this flow. For this reason six different wing cross sections were considered across the wing, whose exact locations are shown in figure 5.17 along with their exact positions which are tabulated in table 5.3 as η.

$\eta = 2y/b$ where y refers to the coordinates along the y-axis which runs in the direction of the span and b

is the total wing span of the FV.

To understand the influence of ride height, the pressure distributions at three different heights and when OGE for $\alpha = 5^\circ$ and 20° are compared at the six different span wise locations and is presented in figures 5.18 and 5.19.

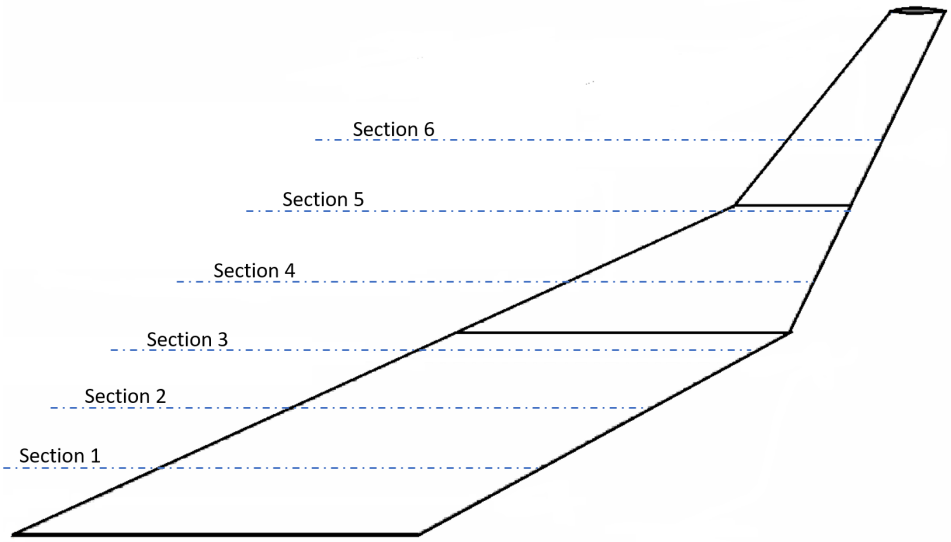

Figure 5.17: Overview of six different cross sections along the wing that were considered for drawing comparisons

Section Number	η
1	0.0668
2	0.200
3	0.334
4	0.468
5	0.602
6	0.758

Table 5.3: Position of each cross sectional plane represented in terms of η

An instant observation that is made when looking at the pressure distributions across all sections on the suction side of the wing is that there is a pronounced negative pressure gradient that moves outward towards the tip. It is this pressure gradient that causes the flow to move radially outward int he span-wise direction.

The heights of the leading edge suction peaks are seen to increase from $\eta = 0.0668$ to $\eta = 0.758$. However, in case of low angles of attack, leading edge low pressure peaks are seen to occur only from $\eta = 0.2$.

On the lower surface of the wing at all pressure locations, the $C_P$is relatively higher as h/b decreases. this is again an indication og the increase in the ram pressure as ride height reduces.

Towards the trailing edge of the wing an adverse pressure gradient is observed i.e. $\frac{dP}{dx} > 0$. This adverse pressure gradient begins at about the 52% chord at $\eta = 0.0668$ for $\alpha = 5^\circ$. However, as the angle of attack increases from 5° to 20°, the start of the adverse pressure gradient is delayed to a 56% chord location. The rate of increase of this adverse pressure gradient increases as α increases.

At $\eta = 0.334$, after the leading edge suction peak that is followed by the pressure recovery and the adverse pressure gradient, a tell tale sign of the start of vortices which are seen as bumps in the C_P curve at about the 86% span wise location exists when $\alpha = 10^\circ$ (not presented here). As the angle of attack increases the strength of these vortices is also seen to increase. This is understood by an even greater reduction in the value of C_P as the ride height reduces indicating an acceleration of the flow.

At high angles of attack i.e. 20°, it is seen that ride height influences the location of its origin and its span wise movement. When $h/b = 0.0769$ vortices are produced at 26% chord and 16% chord locations at $\eta = 0.468$

and $\eta = 0.602$ respectively.

At $\eta = 0.602$ as seen in figure 5.17, is located at the leading edge kink of the wing. As a result of the acceleration of the flow caused by the change int he sweep angle a very large spike in negative C_P is seen. This low pressure peak increases as h/b reduces from ∞ to 0.0769 with a maximum peak equal to -7.

By making use of equation 5.5, it is possible to determine the local Mach number in this region.

$$C_P = \frac{2}{\gamma M_\infty^2}\left[\left(1+\frac{\gamma-1}{2}M^2\right)^{\frac{-\gamma}{\gamma-1}}\left(1+\frac{\gamma-1}{2}M_\infty^2\right)^{\frac{\gamma}{\gamma-1}}-1\right] \tag{5.5}$$

After calculating, the local mach number when closest to the ground is about 0.603 Mach. Being greater than 0.3 Mach, this would indicate that the flow becomes locally compressible in this region.

At $\alpha = 20°$ and $\eta = 0.602$, the rapid deceleration fo the flow is then followed by a region of very little change in pressure along the chord-wise direction i.e. $\frac{dP}{dx} \approx 0$, representative of trailing edge flow separation.

At the tip of the wing i.e. $\eta = 0.758$, the proximity to the ground has a significant effect on the pressure distribution of this section at high angles of attack. Low pressure peaks are again observed at the leading edge of this section. Negative pressure gradients are seen for all heights except when $h/b = 0.0769$ towards the trailing edge. In contrast, a positive pressure gradient is produced at this height when $\eta = 0.758$. At low angles of attack, the low pressure peak is followed by an increase in pressure towards the trailing edge.

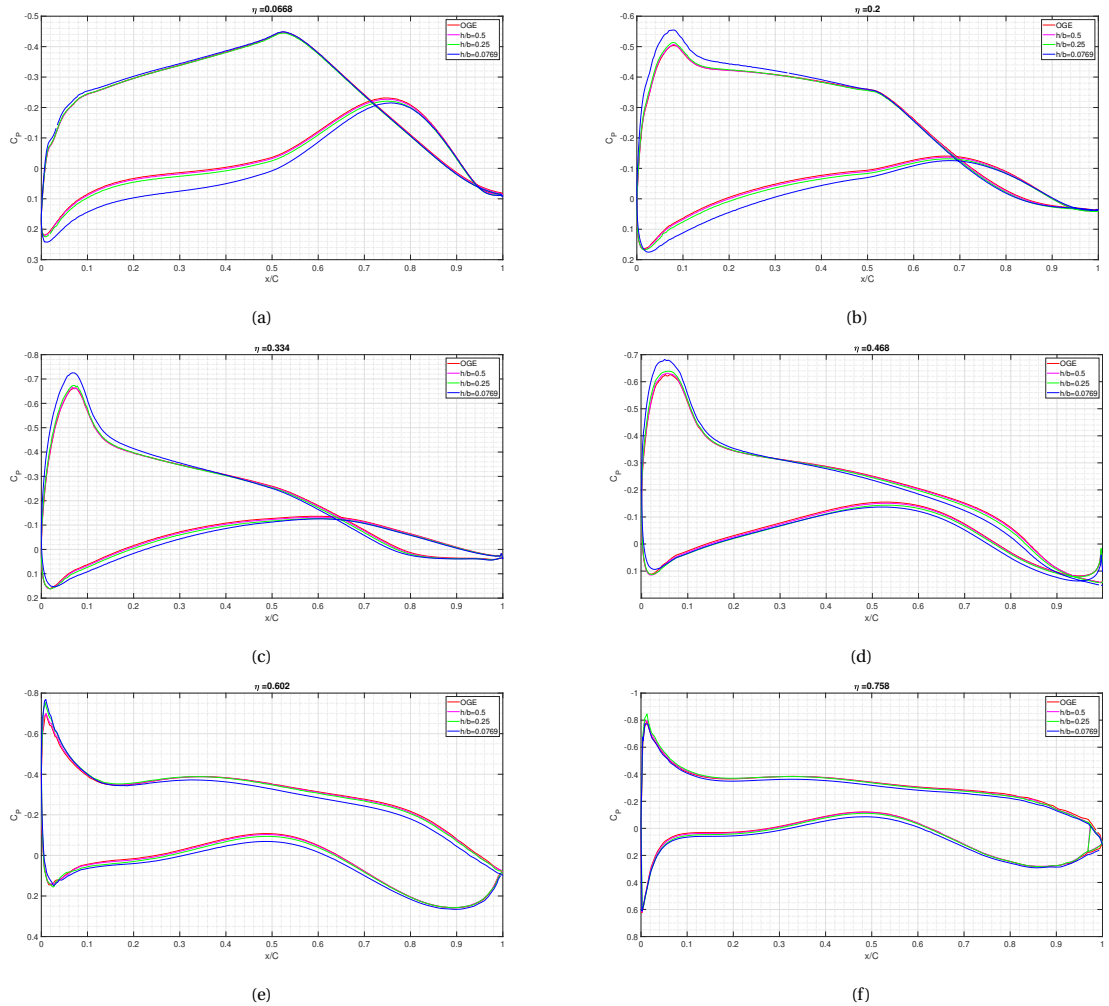

(a) (b) (c) (d) (e) (f)

Figure 5.18: Comparison of pressure distribution with h/b at six different wing section at $\alpha = 5°$

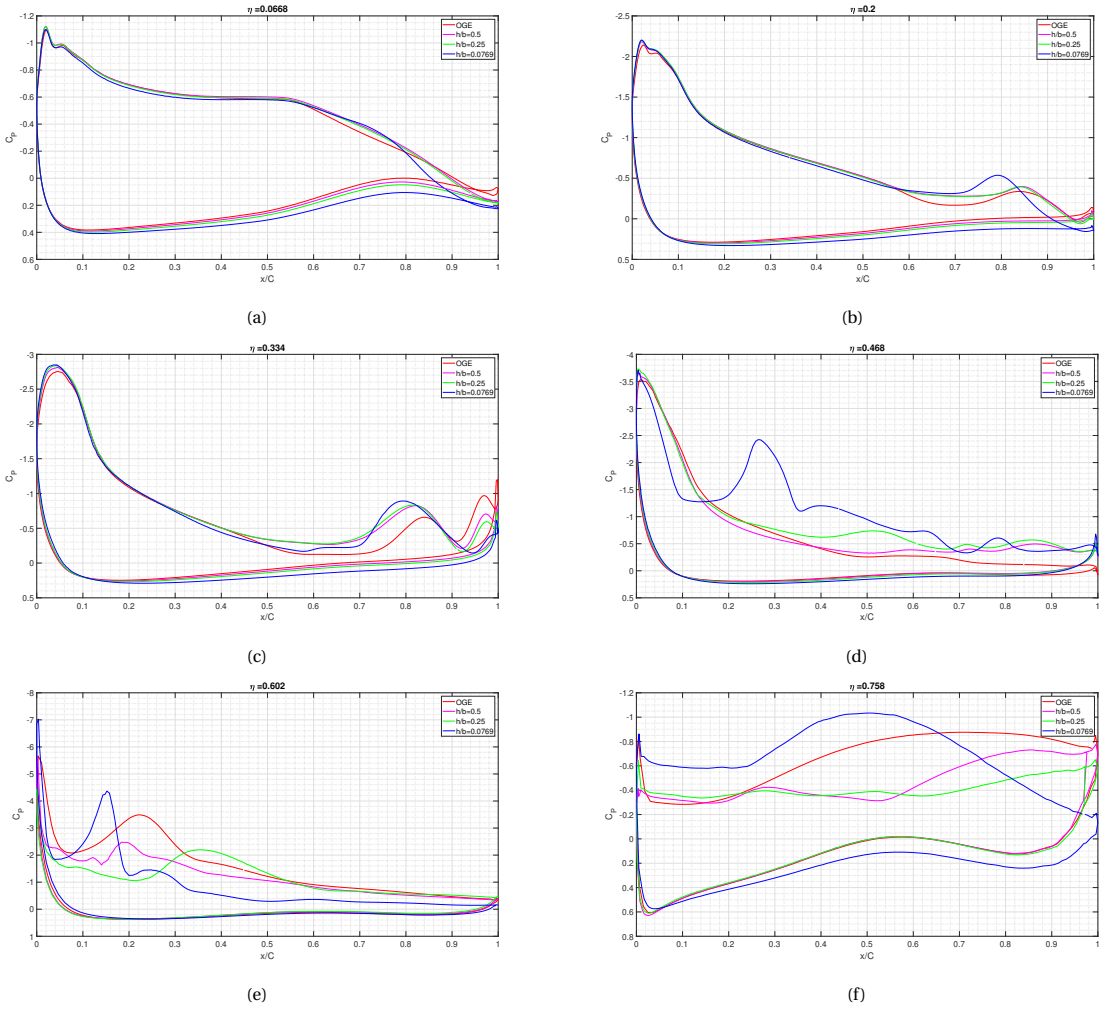

Figure 5.19: Comparison of pressure distribution with h/b at six different wing section at $\alpha = 20°$

5.3. Influence of angle of attack in ground effect

To investigate the influence of angle of attack on the lift charactersitics of the FV when in ground effect, the pressure distributions over different sections of the wing for a range of angles of attack at $h/b - 0.0769$ and $h/b = 0.5$ are presented in figures 5.20 and 5.21.

Some of the general observations that can be made when looking at these figures is that with an increase in the angle of attack from 0° to 20° there is both an increase in the low pressure on the suction side and an increase in high pressure on the pressure side. This can be explained by understanding that in ground effect, a converging-diverging passage is created between the wing and the ground. As α increases, the length of the converging passage increases with an increase in the slope while that of the diverging passage decreases and so does its slope. As a result, a strengthening of the blockage effect occurs causing an increase in pressure on the lower surface of the wing and a decrease in pressure on the upper surface of the wing.

Consider the section closest to the root i.e. $\eta = 0.0668$, it can be observed that leading edge suction peaks only occur for $\alpha > 10°$. The pressure differences between the upper and lower surfaces appear to be directly proportional to the angle of attack. Adverse pressure gradients are seen to occur at all angles of attack towards the trailing edge of this section at roughly the same chord-wise location i.e. 55%. Another interesting observation is that for $\alpha < 10°$ there is a reduction in pressure towards the trailing edge at the lower surface of the FV. This reduction in pressure is seen to be dependent on the height from the ground, further reducing when the height to the ground is reduced as is seen in 5.20a.

In figure **??** at about the 85% chord location for $\alpha \geq 15°$, the formation of vortices is seen. The location and strength of this trailing edge vortex that is seen is dependent on the angle of attack. For $\alpha = 20°$ the vortex is produced earlier at 85% chord while when $\alpha = 15°$ the vortex peak is located at about 90% chord. Secondary

vortices are also observed very close to the trailing edge at about 98% chord.

When looking at figures 5.21c and 5.21d, it is seen that these vortices grow in size before presumably separating as they are not seen anymore at $\eta = 0.468$. When comparing with figures 5.20c and 5.20c it isseen that a similar trend is also followed for $\eta = 0.2$ and $\eta = 0.334$. However when closest to the ground it is seen that at $\alpha = 20°$, large variations in the pressure over the suction surface can be seen. For all $\alpha < 15°$ at sections $\eta = 0.2$ to $\eta = 0.602$ trailing edge separation is seen to occur. This has already been verified to occur for low angles of attack in the surface streamline plots and C_f contour plots presented earlier.

When $\eta = 0.758$, leading edge separation can be observed when looking at figures 5.20f and 5.21f for all $\alpha \leq 10°$.

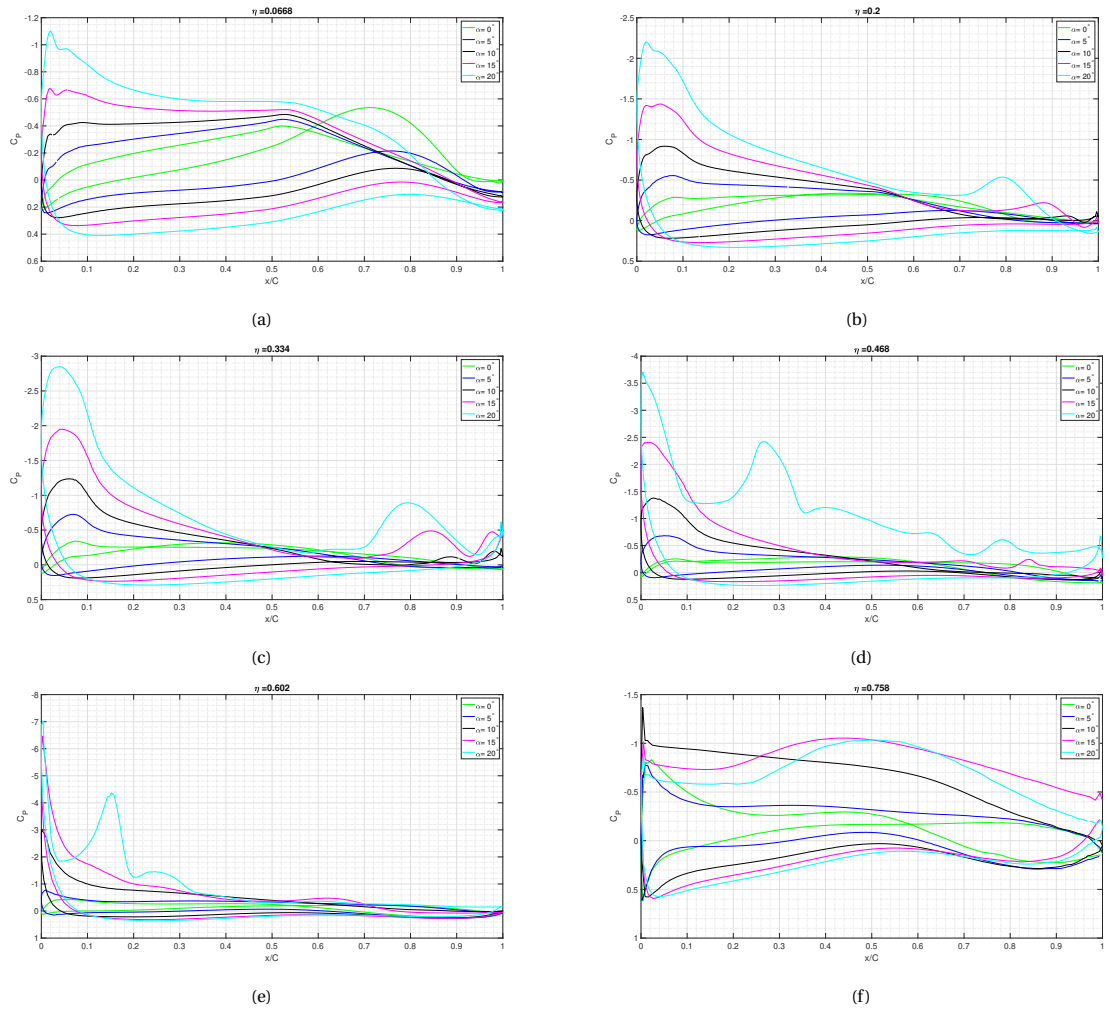

(a) (b) (c) (d) (e) (f)

Figure 5.20: Comparison of pressure distribution at six different wing sections at a $h/b = 0.0769$

To understand the large variations in pressure that are seen at $\eta = 0.468$ and $\eta = 0.602$, the velocity contours at each of these two sections are plotted as shown below in figures 5.22a and 5.22b.

In figure 5.22a the velocity contour shows the formation of a separation bubble very close to the leading edge. This separation bubble is characterized by slow moving air which is why the pressure contour at this location shows a sudden pressure increase. This separation bubble is encapsulated by faster moving air around it and so an immediate low pressure spike is seen on the upper surface of this section in the C_P plot.

In 5.22b the velocity contours show very accurately what happens to the flow at $\eta = 0.602$. owing to the angle of incidence of this section with the free-stream, flow acceleration is seen to take place at the leading edge. This explains the low pressure peak that is seen on the C_P distribution in figure 5.20e. The velocity contour shows that after this acceleration there are sudden breaks in the flow that alternate between high velocity and low velocity air likely caused by the strong span wise vortices moving across this section.

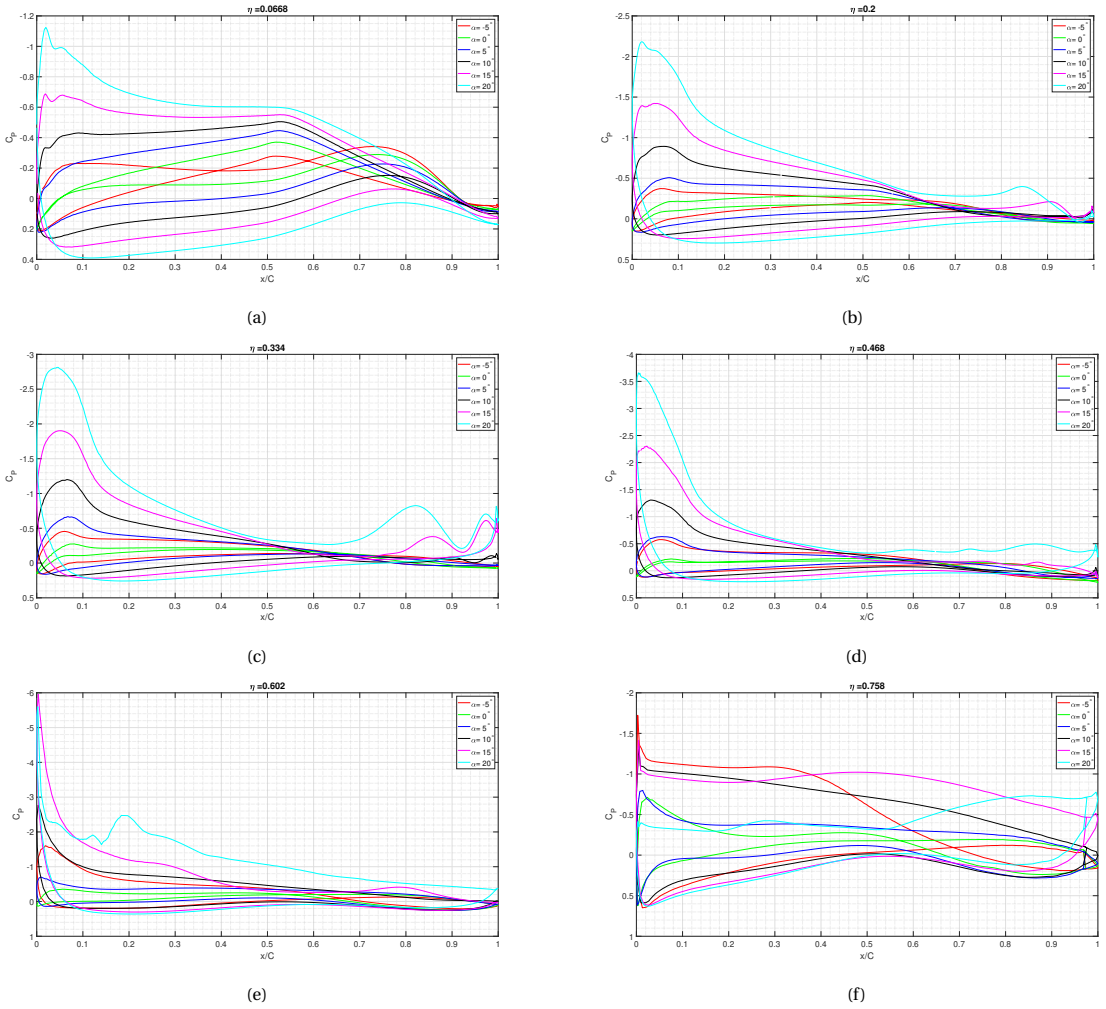

(a) (b)

(c) (d)

(e) (f)

Figure 5.21: Comparison of pressure distribution at six different wing sections at a $h/b = 0.5$

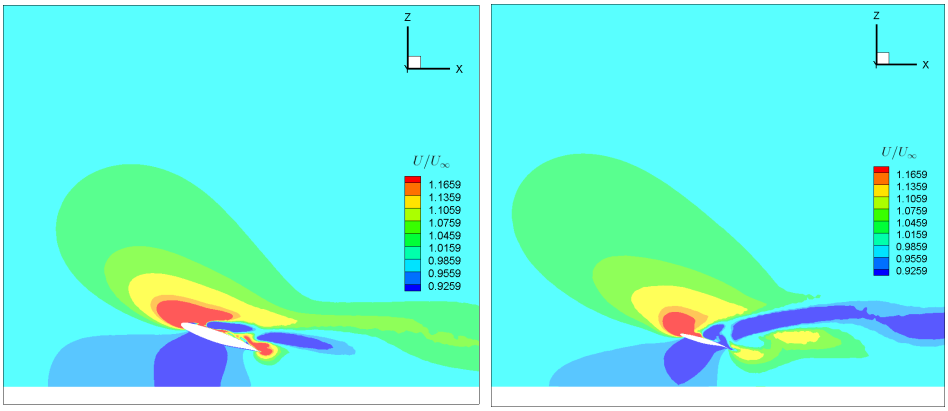

(a) $\eta = 0.468$ (b) $\eta = 0.602$

Figure 5.22: Velocity contours across planes located at the vicinity of the leading edge kink of the FV oriented at $\alpha = 20^\circ$ and $h/b = 0.0769$

5.4. Vortex Visualization

To visualize the vortices produced over the wing when IGE and OGE as mentioned in previous sections the Q-criterion was used. Given by equation **??**, it essentially refers to a balance between the shear strain rate S

and the magnitude of vorticity Ω such that when $Q > 0$, then $\Omega > S$, vortices can be defined.

$$Q = \frac{1}{2}\left(||\overline{\Omega}||^2 - ||\overline{S}||^2\right) \tag{5.6}$$

Figures 5.23, 5.24 and 5.25 show iso-surfaces of the Q criterion that is equal to 1×10^5 for different heights from the ground and at different angles of attack, produced over the wing .

In order to compare all the different cases, each angle of attack at each height is compared with each other.

- $\alpha = \mathbf{5}^\circ$ Irrespective of the height from the ground at low angles of attack as was shown by the surface streamlines, separation is seen to occur only towards the trailing edges of the inner trunk and mid trunk sections of the wing. Apart from this, two types of vortices can be identified. For all heights from the ground, the tip vortices are visualized over the wing and are not significantly different from each other. The second set of vortices that can be seen are the those that are rolling up from the lower surface of the FV towards the trailing edge. These vortices also do not change in size or direction if h/b reduces

- $\alpha = \mathbf{10}^\circ$ At this angle of attack many vortices are seen to develop over the wing. In unbounded flow the two trailing edge vortices that were present for the 5° case can also be seen here. However it can clearly be seen that the increase in angle of attack brought with it an increase in the span wise flow over the wing causing these vortices to bulk up. When comparing these vortices for different heights, it can be seen that as h/b reduces one of these trailing edge vortices located on the suction side starts moving more inwards towards the middle trunk of the wing. The vortex that flows up from the pressure side to the suction side is mainly responsible for causing the low pressure peaks that are seen on the upper surface of the pressure distributions at $\eta = 0.334$ on wards. Some amount of leading edge separation has also started to occur which is representative of what is seen for $\eta = 0.758$. These iso-surfaces also highlight how the flow increases in its tendency to flow incrementally outwards towards the tip

- $\alpha = \mathbf{20}^\circ$ The trialing edge vortex that was developing over the suction side of the wing is seen to be energized by a vortex that emanates from close to the root of the wing. In ground effect, this vortex grows in size as it is fed by smaller vortices emerging from the leading edge of the inboard trunk. This vortex eventually separates from the surface of the wing at the trailing edge located at the end of the inboard trunk. When closest to the ground, another large vortex is seen to develop close to the leading edge kink. This vortex then just develops and flows away from the wing in the stream-wise direction itself. The vortex that was first identified rolling up from the pressure side towards the suction is still present at $\alpha = 20^\circ$. This vortex eventually separates away from the FV at the end of the inboard trunk of the wing. In unbounded flow, it can be clearly seen that a very large vortex is produced at the leading edge kink of the wing. As the height reduces, this vortex at the kink grows in size as the flow accelerates and then is also made to flow further outwards before separating away from the wing at the middle of the outer trunk. At the outer trunk although there is leading edge separation taking place, at high angles of attack, the vortices moving in the span-wise direction delay its onset.

5.5. Near Wake Analysis

In the previous section, the vortical structures shown using the Q criterion, indicate the formation of prominent vortices emanating from the leading edge kink of the wing and from the middle trunk of the wing at high angles of attack. This section aims to investigate the near wake behavior due to these vortices when in ground proximity as the pressure gradient over the wing is said to have a huge influence on the development of the wake and its structure [48].

The figures 5.26 to 5.28 depict the pressure coefficients on a plane located very close to the tip of the wing and in its wake at a distance of $x/b = 0.868$ for four angles of attack varying between $\alpha = 0^\circ$ and $\alpha = 20^\circ$ and three different heights between $h/b = \infty$ to $h/b = 0.0769$.

At low angles of attack i.e. $\alpha = 0^\circ$ and $\alpha = 10^\circ$, there does not seem to be large pressure variations in the wake of the FV. What in fact can be seen is that the tip vortices produced increase in strength as the angle of attack increases. When in unbounded flow a secondary vortex located inboard is produced at $\alpha = 17^\circ$. The diameter of the tip vortex is seen to be greater than the inboard secondary vortex for $\alpha = 17^\circ$. But it is also possible that the refinement of the mesh in each of these regions were different and so may not be entirely accurate. In unbounded flow the secondary vortex and the tip vortex appear to merge together but as the ride

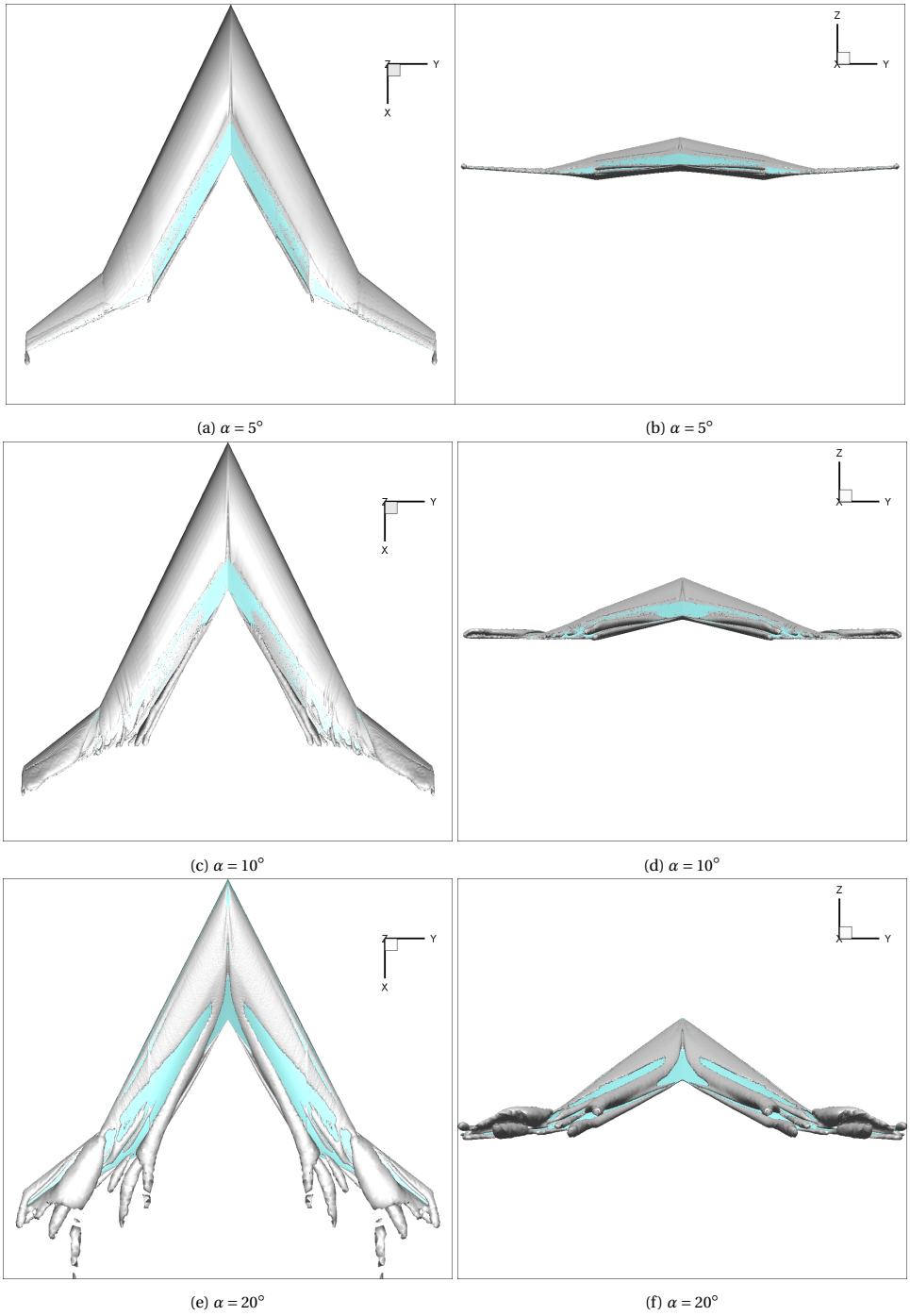

(a) $\alpha = 5°$ (b) $\alpha = 5°$

(c) $\alpha = 10°$ (d) $\alpha = 10°$

(e) $\alpha = 20°$ (f) $\alpha = 20°$

Figure 5.23: Top and rear views of vortical structures over the FV at a $h/b = \infty$

height reduces, the two vortices appear to become more and more independent. This merging of vortices becomes possible when the distance between the two vortices is very small in comparison to the diameter of their centers[75].

At greater angles of attack, the secondary vortex is seen to grow in diameter as the height reduces. The strength of this secondary vortex also increases when it is closest to the ground at a very high angle of attack. This is explained by an increase in circulation and the very low pressure that they bring about. This strengthening of the vortex will lead to a delayed vortex breakdown as is also seen in the iso-surfaces of the Q criterion. Interesting to also see is that the inboard secondary vortex starts moving more and more inboard as the ride height reduces. This growth of the secondary vortex when closest to the ground at high angles of

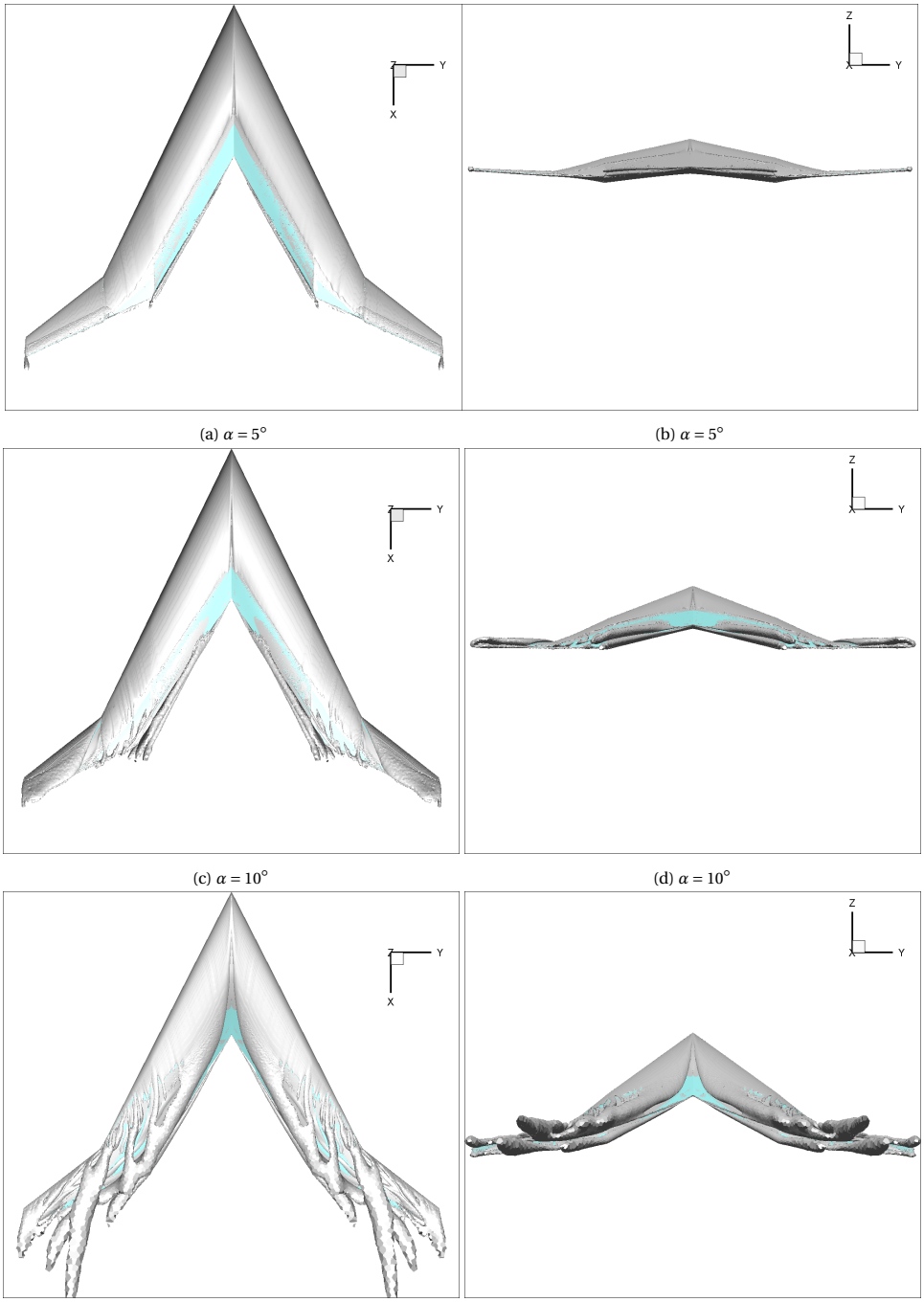

(a) $\alpha = 5°$ (b) $\alpha = 5°$

(c) $\alpha = 10°$ (d) $\alpha = 10°$

(e) $\alpha = 20°$ (f) $\alpha = 20°$

Figure 5.24: Top and rear views of vortical structures over the FV at a $h/b = 0.25$

attack is what is noticed in the C_D vs α curve that was plotted in figure 5.2.

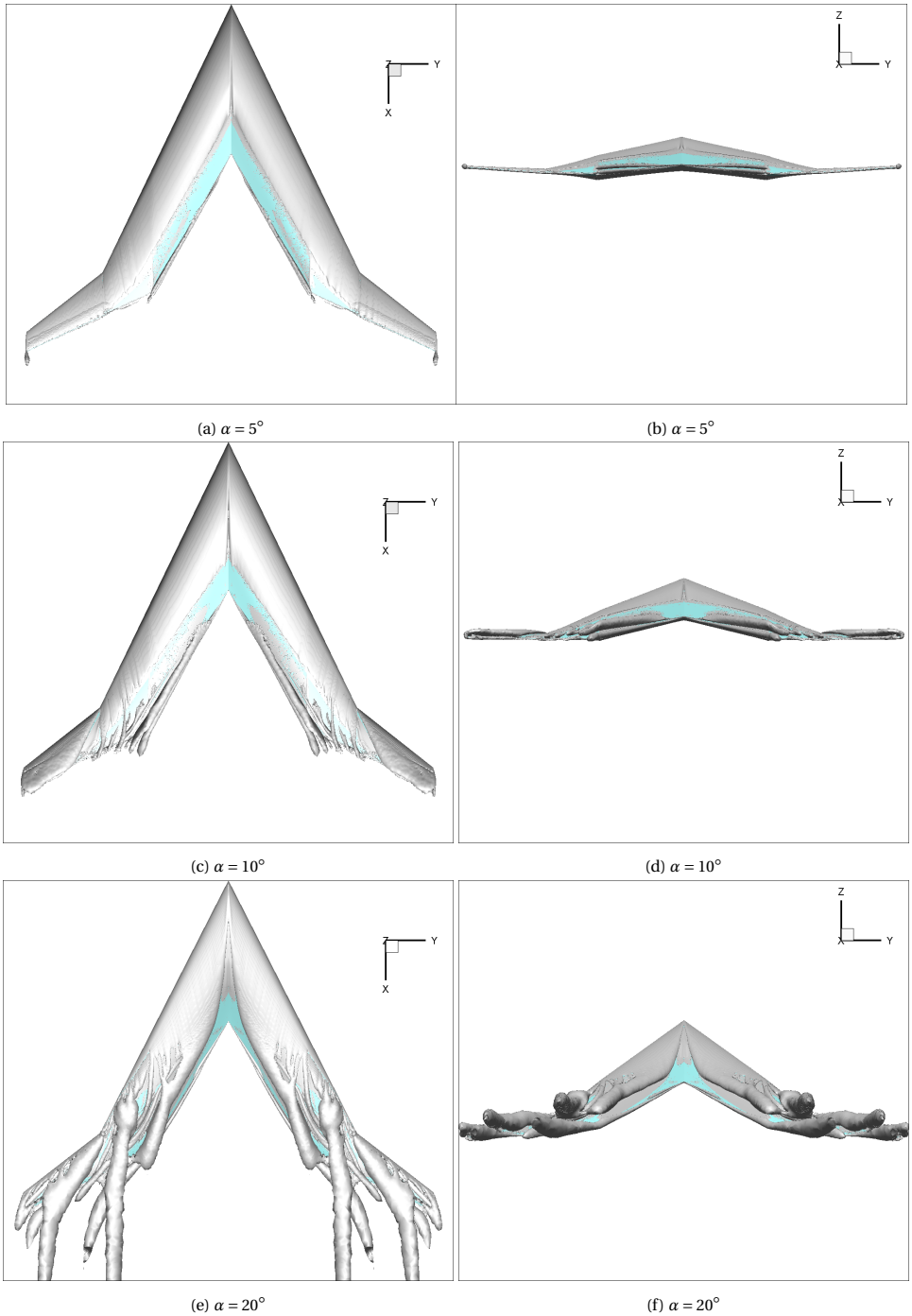

(a) $\alpha = 5^\circ$ (b) $\alpha = 5^\circ$

(c) $\alpha = 10^\circ$ (d) $\alpha = 10^\circ$

(e) $\alpha = 20^\circ$ (f) $\alpha = 20^\circ$

Figure 5.25: Top and rear views of vortical structures over the FV at a $h/b = 0.0769$

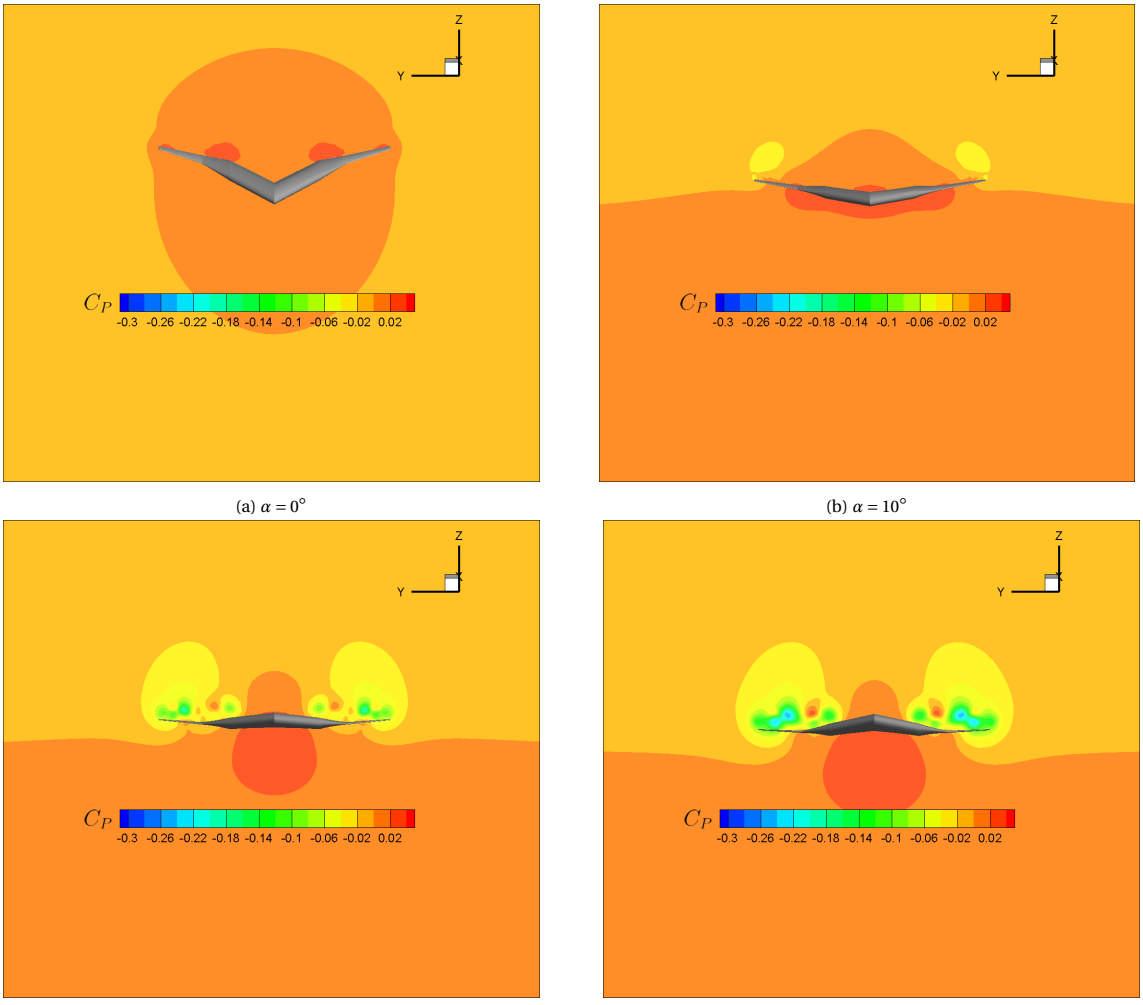

(a) $\alpha = 0°$

(b) $\alpha = 10°$

(c) $\alpha = 17°$

(d) $\alpha = 20°$

Figure 5.26: Comparison of near wake pressure coefficient plots on a plane located in the stream-wise direction at $x/b = 0.868$ and $h/b = \infty$ (OGE)

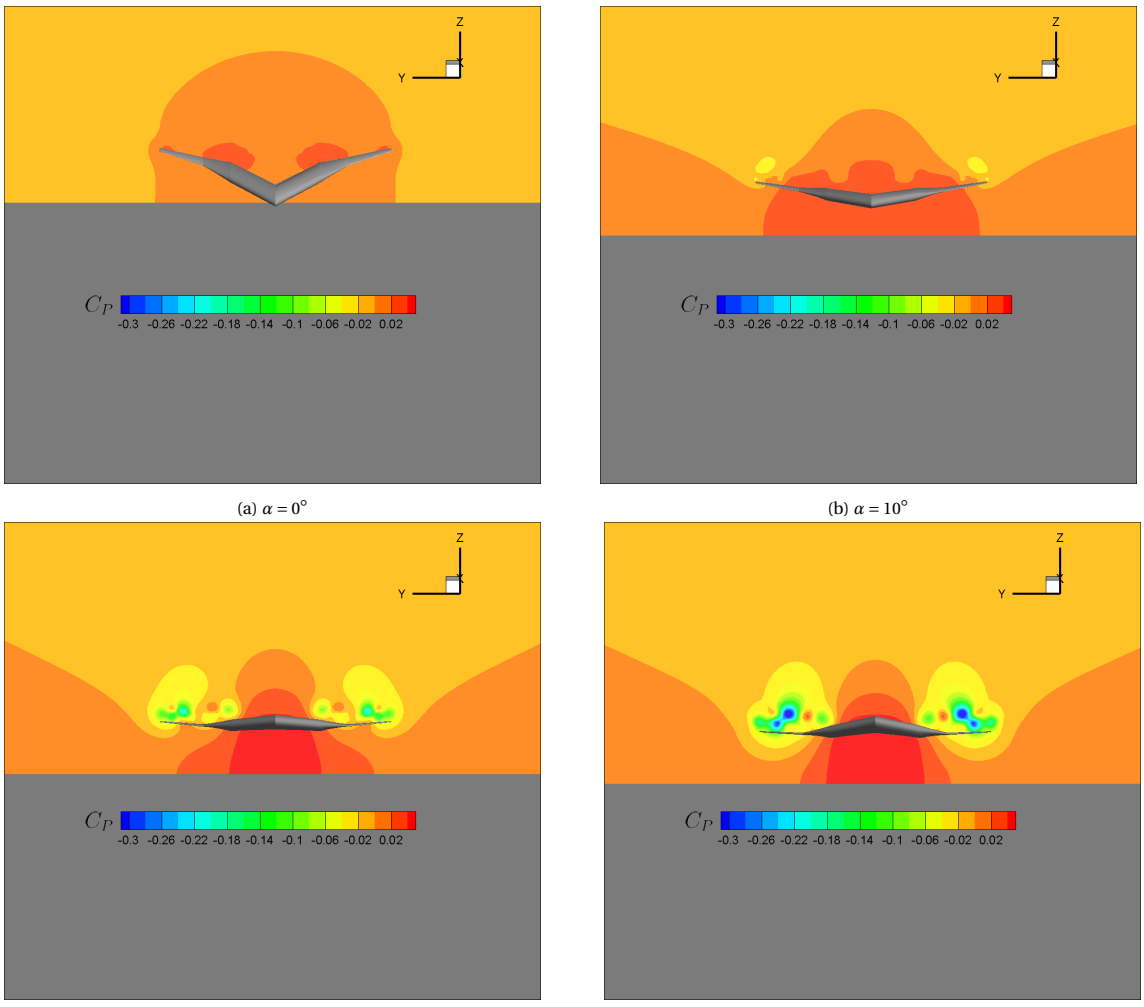

(a) $\alpha = 0°$

(b) $\alpha = 10°$

(c) $\alpha = 17°$

(d) $\alpha = 20°$

Figure 5.27: Comparison of near wake pressure coefficient plots on a plane located in the stream-wise direction at $x/b = 0.868$ and $h/b = 0.25$

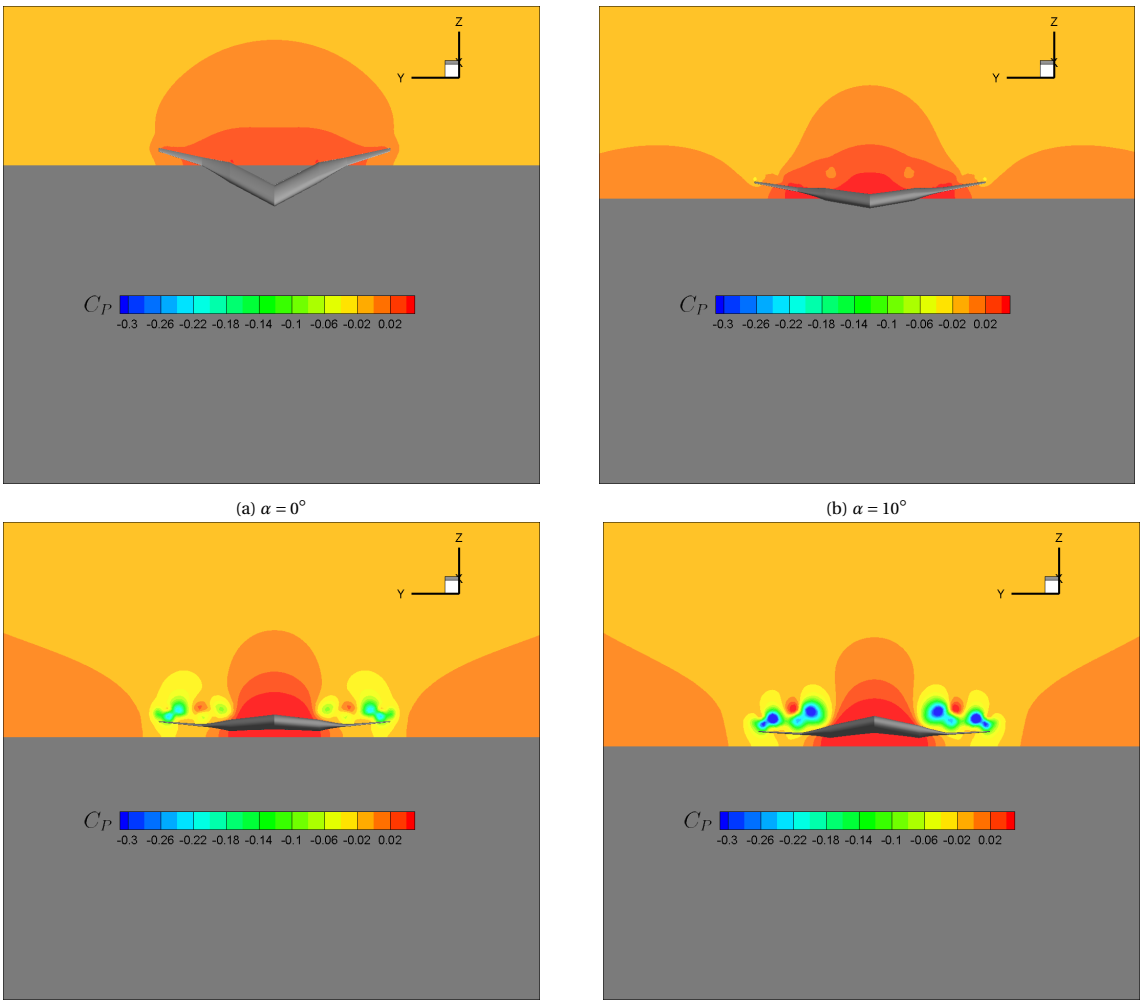

(a) $\alpha = 0°$

(b) $\alpha = 10°$

(c) $\alpha = 17°$

(d) $\alpha = 20°$

Figure 5.28: Comparison of near wake pressure coefficient plots on a plane located in the stream-wise direction at $x/b = 0.868$ and $h/b = 0.07694$

6

Conclusions and Recommendations

The aim of this thesis was to study the influence of ground effect on the Flying V aircraft from the perspective of aerodynamics and assess its lift performance and stability at several different heights from the ground at different angles of attack. To perform these RANS simulations, the $k-\omega$ SST turbulence model was used based on a verification and validation study that was conducted by making use of LES data. Simulations were performed by making use of a 4.6% scaled model of the FV. A domain sensitivity study showed a change of less than 0.1% when the domain size was set to $6.688b$ while the grid dependence study that was also carried out ensured that a grid of medium refinement consisting of 21.54 million cells would be the most ideal.

The results were determined by dividing the problem into four main areas:

- Comparison of Aerodynamic Coefficients IGE
- Flow Phenomena Analysis
- Influence of Ride Height on the FV IGE
- Influence of Angle of Attack IGE
- Vortex Visualization
- Near Wake Analysis

The key findings obtained from these studies were :

- Results obtained showed that as the ride height, h/b decreases from ∞ to 0.0769 for a fixed angle of attack, the FV experiences a gain in lift and a reduction in drag caused mainly by a reduction in the induced drag. The drag polar K showed a reduction of 11% when closest to the ground as compared to being in unbounded flow. The gain and loss in lift and drag can be attributed to chord dominated ground effect and span dominated ground effect respectively. Given the improvement in lift that is seen in ground effect the FV can fly at an α that is one degree lesser when it is closest to the ground to obtain a specific coefficient of lift in unbounded flow. The ramification of this is that while landing the FV can touch down at an angle of 19° rather than 20°. The FV requires a lift-drag ratio of at least 10.0 in order to have a positive climb gradient. This would mean that during take off the maximum rotation angle is equal to 13° for a specified lift off lift coefficient of 0.56.
- Favorable pitching moment characteristics are observed for $-5^\circ < \alpha < 7.5^\circ$ and $\alpha > 17.5^\circ$. This variation that is seen in the pitching moment can be explained by the change in the local lift distribution over the wing at different angles of attack.
- Surface streamlines showed that as the height reduces there is a shift in the location of the separation line closer towards the leading edge. This would mean that as the height reduces, trailing edge separation occurs earlier along the mid-section of the wing.

- No significant span wise flow is seen when $\alpha = 0°$ and the flow appears to travel parallel to the streamwise direction. Additionally, in case of very high angles of attack, the flow streamlines confirm the occurrence of a large vortex emanating from the leading edge kink of the wing.
- When in unbounded flow a secondary vortex located inboard is produced at $\alpha = 17°$. The diameter of the tip vortex is seen to be greater than the inboard secondary vortex for $\alpha = 17°$. At greater angles of attack, the secondary vortex is seen to grow in diameter as the height reduces.

As a result of the conclusions drawn from this thesis, several different topics of research can be considered:

- Numerical results are obtained on the basis of a large number of assumptions and approximation. For this reason, an experimental campaign to validate the results obtained from this thesis would be beneficial.
- Since ground effect stems from the distortion of the wings downwash, it would be especially interesting to study the effects that ground proximity would have on the FV after the integration of winglets.
- The effects of introducing bank angles and yaw angles at different angles of attack at different heights from the ground is also a very crucial segment within the assessment of ground effect behavior of the FV that must be carried out in the future. At a specific bank angle, the wings of the FV are influenced very differently by the ground with one side closer to the ground than the other and therefore experiencing an imbalanced lift improvement and drag change. This would directly affect the lateral stability of the FV. As a result of the increase in lift on one side of the wing, a righting moment is introduced. Additionally, the drag imbalance on either side of the wing can result in an adverse yaw moment.

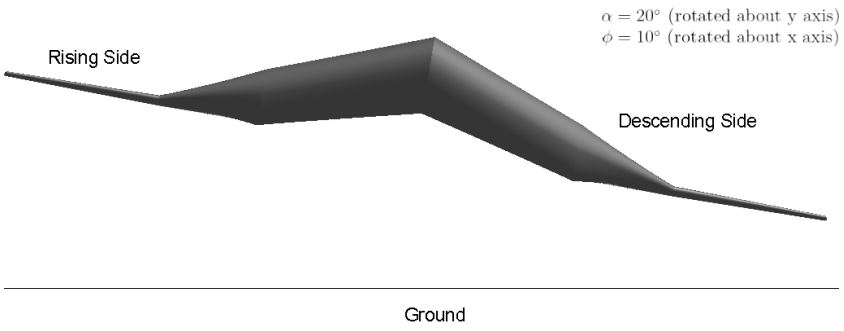

Figure 6.1: Representation of Bank Angle and the proximity of each side of the wing to the ground

- This thesis only considers a single component of motion. In real world scenarios, during take off and landing it is almost impossible to have a uni-directional flow of air that interacts with the aircraft. For this reason, another interesting research area of study would be to consider the behavior of the FV in cross flow conditions.

Bibliography

[1] URL https://www.simutechgroup.com/images/easyblog_articles/7/ANSYS-Fluent-Mosaic-Technology-Automatically-Comb pdf.

[2] Effects of ground proximity on the aerodynamic characteristics of aspect-ratio-1 aerofoils with and without end plates. *NASA TN D-970*.

[3] Air - specific heat at constant pressure and varying temperature. URL https://www.engineeringtoolbox.com/air-specific-heat-capacity-d_705.html.

[4] Aviation boost through box-wing design. URL https://ec.europa.eu/research/infocentre/printversion_en.cfm?id=/research/headlines/news/article_18_04_06_en.html?infocentre&item=Infocentre&artid=48017.

[5] Tomasz Abramowski. Numerical investigation of airfoil in ground proximity. *Journal of Theoretical and Applied Mechanics*, 45:425–436, 2007.

[6] Mohammed Rafiuddin Ahmed, Hideyuki Siragane, and Yasuaki Kohama. Boundary layer contrlo with a moving belt system for studies on wing-in-ground-effect. *JSME International Journal Series B Fluids and Thermal Engineering*, 42(4):619–625, 1999.

[7] John D Anderson Jr. Solutions manual to accompany introduction to flight. *energy*, 20(26):6, 2005.

[8] Ansys Fluent Tutorial's Guide Ansys and Solver Modeling Guide. Release 14.5. *Canonsburg, PA*, 2012.

[9] Mario Asselin. *An introduction to aircraft performance*. American Institute of Aeronautics and Astronautics, 1997.

[10] ATAG. Aviation benefits beyond borders, April . URL https://aviationbenefits.org/media/26786/ATAG__AviationBenefits2014_FULL_LowRes.pdf.

[11] Tracie Barber and Stephen Hall. Aerodynamic ground effect: a case study of the integration of cfd and experiments. *International Journal of Vehicle Design*, 40(4):299, 2006.

[12] Eckhard Beese. *Untersuchungen zum Einfluß der Reynolds-Zahl auf die aerodynamischen Beiwerte von Tragflügelprofilen in Bodennähe*. PhD thesis, Ruhr-Universität Bochum, 1982.

[13] Washington Bellevue. Tecplot 360 ex 2018 release 1 user manual. *Tecplot Inc*, 2018.

[14] J. Benad. The flying v: A new aircraft configuration for commercial passenger transport. *Deutscher Luft- und Raumfahrtkongress*, 08 2015.

[15] AL Bolsunovsky, NP Buzoverya, BI Gurevich, VE Denisov, AI Dunaevsky, LM Shkadov, OV Sonin, AJ Udzhuhu, and JP Zhurihin. Flying wing—problems and decisions. *Aircraft design*, 4(4):193–219, 2001.

[16] Arthur W Carter. Effects of ground proximity on the longitudinal aerodynamic characteristics of an unswept aspect-ratio-10 wing. *NASA TN D-5662*, 02 .

[17] Reagan I. Porter C. Cooper, T. and C. Precourt. Global fleet and mro market forecast commentary 2019–2029, 2019. URL https://www.oliverwyman.com/content/dam/oliver-wyman/v2/publications/2019/January/global-fleet-mro-market-forecast-commentary-2019-2029.pdf.

[18] Erjie Cui and Xin Zhang. Ground effect aerodynamics. *Encyclopedia of Aerospace Engineering*, 2010.

[19] TU Delft. Chapter 7: Practical guidelines for cfd simulation and analysis. URL https://www.researchgate.net/profile/Md_Washim_Akram/post/Could_you_present_more_detailes_about_your_CFD_setting/attachment/5b443dcdb53d2f892899790c/AS%3A646709319319554%401531198925877/download/tu2018.pdf.

[20] Ning Deng, Qiulin Qu, and Ramesh K Agarwal. Numerical study of the aerodynamics of dlr-f6 wing-body in unbounded flow field and in ground effect. In *55th AIAA Aerospace Sciences Meeting*, page 1424, 2017.

[21] Vladimir G Dmitriev, Leonid M Shkadov, Vladimir E Denisov, Boris I Gurevich, Sergei V Lyapunov, and Oleg V Sonin. The flying wing concept- chances and risks. In *2003 AIAA/ICAS International Air and Space Symposium and Exposition: The Next 100 Years*, 2003.

[22] Bastian Dose. *CFD Simulations of a 2.5 MW wind turbine using ANSYS CFX and OpenFOAM*. PhD thesis, MSc Thesis, UAS Kiel and FhG IWES, Germany, 2013.

[23] S D'Urso and Rodrigo Martinez-Val Peñalosa. Flight dynamics of the flying wing. 2008.

[24] Jac van Egmond.

[25] B Fago, H Lindner, and O Mahrenholtz. The effect of ground simulation on the flow around vehicles in wind tunnel testing. *Journal of Wind Engineering and Industrial Aerodynamics*, 38(1):47–57, 1991.

[26] Joel H Ferziger and Milovan Perić. *Computational methods for fluid dynamics*, volume 3. Springer, 2002.

[27] F.Faggiano. Aerodynamic design optimization of a flying v aircraft,. page 99, 11 2016.

[28] TB Gatski and CL Rumsey. Linear and nonlinear eddy viscosity models. *Closure strategies for turbulent and transitional flows*, pages 9–46, 2002.

[29] Bosko ; Dulikravich George ; Parezanovic Vladimir Gavrilovic, Nikola ; Rasuo. Commercial aircraft performance improvement using winglets. *FME Transaction*, pages 1–8, 01 2015. doi: 10.5937/fmet1501001g.

[30] AR George. Aerodynamic effects of shape, camber, pitch, and ground proximity on idealized ground-vehicle bodies. 1981.

[31] F George. Flying the a350: Airbus's most technologically advanced airliner. *Aviation Week & Space Technology, May*, 22:2015, 2015.

[32] Klaus Gersten. Hermann schlichting and the boundary-layer theory. In *Hermann Schlichting–100 Years*, pages 3–17. Springer, 2009.

[33] Lillian Gipson. The double bubble d8, Mar 2015. URL https://www.nasa.gov/content/the-double-bubble-d8-0.

[34] Snorri Gudmundsson. Chapter 9 - the anatomy of the wing. In Snorri Gudmundsson, editor, *General Aviation Aircraft Design*, pages 299 – 399. Butterworth-Heinemann, Boston, 2014. ISBN 978-0-12-397308-5. doi: https://doi.org/10.1016/B978-0-12-397308-5.00009-X. URL http://www.sciencedirect.com/science/article/pii/B978012397308500009X.

[35] H. Helmholtz. Lxiii. on integrals of the hydrodynamical equations, which express vortex-motion. *The London, Edinburgh, and Dublin Philosophical Magazine and Journal of Science*, 33(226):485–512, 1867. doi: 10.1080/14786446708639824. URL https://doi.org/10.1080/14786446708639824.

[36] Michael Holloran and Sean O'Meara. Wing in ground effect craft review. Technical report, DEFENCE SCIENCE AND TECHNOLOGY ORGANISATION CANBERRA (AUSTRALIA), 1999.

[37] Chih-Min Hsiun and Cha'o-Kuang Chen. Aerodynamic characteristics of a two-dimensional airfoil with ground effect. *Journal of Aircraft*, 33(2):386–392, 1996.

[38] IATA. Iata fuel fact sheet, June 2019. URL https://www.iata.org/pressroom/facts_figures/fact_sheets/Documents/fact-sheet-fuel.pdf.

[39] ICAO. Icao annual report of the council 2018, December 2018. URL https://www.icao.int/annual-report-2018/Pages/default.aspx.

[40] Ph.D. Ideen Sadrehaghighi. Mesh generation in cfd. page 59, 04 1989.

[41] Shubham Jain, Nekkanti Sitaram, and Sriram Krishnaswamy. Effect of reynolds number on aerodynamics of airfoil with gurney flap. *International Journal of Rotating Machinery*, 2015, 2015.

[42] Qing Jia, Wei Yang, and Zhigang Yang. Numerical study on aerodynamics of banked wing in ground effect. *International Journal of Naval Architecture and Ocean Engineering*, 8(2):209–217, 2016.

[43] George Karniadakis, Ali Beskok, and Narayan Aluru. *Microflows and nanoflows: fundamentals and simulation*, volume 29. Springer Science & Business Media, 2006.

[44] Roy H Lange. Review of unconventional aircraft design concepts. *Journal of Aircraft*, 25(5):385–392, 1988.

[45] CT Lao and ETT Wong. Cfd simulation of a wing-in-ground-effect uav. In *IOP Conference Series: Materials Science and Engineering*, volume 370, page 012006. IOP Publishing, 2018.

[46] Zhong Lei. Effect of rans turbulence models on computation of vortical flow over wing-body configuration. *Transactions of the Japan Society for Aeronautical and Space Sciences*, 48(161):152–160, 2005.

[47] Kevin W Linfield and Robert G Mudry. Pros and cons of cfd and physical flow modeling. *Air Flow Sciences Corporation*, 8, 2008.

[48] Xiaofeng Liu, Flint Thomas, and Robert Nelson. An experimental investigation of wake development in arbitrary pressure gradients. In *37th Aerospace Sciences Meeting and Exhibit*, page 677, 1999.

[49] Stephen Mahon and Xin Zhang. Computational analysis of pressure and wake characteristics of an aerofoil in ground effect. *Journal of Fluids Engineering*, 127(2):290–298, 2005.

[50] Barnes W McCormick. Aerodynamics, aeronautics and fligth mechanics. 1995.

[51] Fadi Mishriky and Paul Walsh. Towards understanding the influence of gradient reconstruction methods on unstructured flow simulations. *Transactions of the Canadian Society for Mechanical Engineering*, 41 (2):169–179, 2017.

[52] Young J Moon, Hyeon-Joon Oh, and Jung-Hee Seo. Aerodynamic investigation of three-dimensional wings in ground effect for aero-levitation electric vehicle. *Aerospace science and technology*, 9(6):485–494, 2005.

[53] Mark V Morkovin. Effects of compressibility on turbulent flows. *Mécanique de la Turbulence*, 367:380, 1962.

[54] BR Munson, DF Young, and TH Okiishi. Fundamentals of fluid mechanics, 1998.

[55] G. Anzaldo Muñoz. Mesh quality and advenced topics ansys workbench 16.0. URL https://www.academia.edu/16970000/MESH_QUALITY_AND_ADVENCED_TOPICS_ANSYS_WORKBENCH_16.0.

[56] S Murakami. Comparison of various turbulence models applied to a bluff body. *Journal of Wind Engineering and Industrial Aerodynamics*, 46-47:21 – 36, 1993. ISSN 0167-6105. doi: https://doi.org/10.1016/0167-6105(93)90112-2. URL http://www.sciencedirect.com/science/article/pii/0167610593901122. Proceedings of the 1st International on Computational Wind Engineering.

[57] Mimoza Musaj. *Computational and Experimental Investigation of the Aerodynamics of a W-shaped leading edge reversed delta plan-form wing*. PhD thesis, City, University of London, 2010.

[58] John K Northrop. The development of all–wing aircraft. *The Aeronautical Journal*, 51(438):481–510, 1947.

[59] Marco Palermo. *The Longitudinal Static Stability and Control Characteristics of a Flying V Scaled Model: An Experimental and Numerical Investigation*. PhD thesis, TU Delft Repository, 2019.

[60] JW Paulson Jr and Scott O Kjelgaard. An experimental and theoretical investigation of thick wings at various sweep angles in and out of ground effect. 1982.

[61] Brian Pearce. The shape of air travel markets over the next 20 years. In *Global airport development conference*, 2014.

[62] Li Peifeng, Binqian Zhang, Chen Yingchun, YUAN Changsheng, and LIN Yu. Aerodynamic design methodology for blended wing body transport. *Chinese Journal of Aeronautics*, 25(4):508–516, 2012.

[63] Milovan Peric. Flow simulation using control volumes of arbitrary polyhedral shape. *ERCOFTAC bulletin*, 62:25–29, 2004.

[64] Qiulin Qu, Wei Wang, Peiqing Liu, and Ramesh K Agarwal. Airfoil aerodynamics in ground effect for wide range of angles of attack. *AIAA Journal*, 53(4):1048–1061, 2015.

[65] William C Reynolds. The potential and limitations of direct and large eddy simulations. In *Whither turbulence? Turbulence at the crossroads*, pages 313–343. Springer, 1990.

[66] Timothy K Risch. X-48b flight research progress overview. 2008.

[67] Luke S Roberts, Joao Correia, Mark V Finnis, and Kevin Knowles. Aerodynamic characteristics of a wing-and-flap configuration in ground effect and yaw. *Proceedings of the Institution of Mechanical Engineers, Part D: Journal of Automobile Engineering*, 230(6):841–854, 2016.

[68] Dino Roman, Richard Gilmore, and Sean Wakayama. Aerodynamics of high-subsonic blended-wing-body configurations. In *41st Aerospace Sciences Meeting and Exhibit*, page 554, 2003.

[69] J Roskam and G Fillman. Design for minimum fuselage drag. *Journal of Aircraft*, 13(8):639–640, 1976.

[70] B. rubio Pascual. Engine-airframe integration for the flying v. page 90, 02 2018.

[71] Aviation Safety. Statistical summary of commercial jet airplane accidents, 2017. URL https://www.boeing.com/resources/boeingdotcom/company/about_bca/pdf/statsum.pdf.

[72] R. D. Schaufele. Faa aerospace forecasts fiscal years 2018-2038, 2018. URL https://www.faa.gov/data_research/aviation/aerospace_forecasts/media/fy2018-38_faa_aerospace_forecast.pdf.

[73] Ralph L Schwader. The development of the flying wing. *Journal of Aviation/Aerospace Education & Research*, 8(1):4, 1997.

[74] M Sereez, Nikolay Abramov, and M Goman. Computational ground effect aerodynamics and airplane stability analysis during take-off and landing. EUCASS, 2017.

[75] Philippe R Spalart. Airplane trailing vortices. *Annual Review of Fluid Mechanics*, 30(1):107–138, 1998.

[76] Dieter Steinbach. Comment on" aerodynamic characteristics of a two-dimensional airfoil with ground effect". *Journal of Aircraft*, 34(3):455–456, 1997.

[77] L.A. van der Schaft. Development, model generation and analysis of a flying v structure concept by. page 133, 06 2017.

[78] Oliverio Esteban Velázquez Salazar, Julien Weiss, and François Morency. Development of blended wing body aircraft design. 01 2015. doi: 10.13140/RG.2.1.3878.9840.

[79] Th Von Kármán. Mechanische änlichkeit und turbulenz. *Nachrichten von der Gesellschaft der Wissenschaften zu Göttingen, Mathematisch-Physikalische Klasse*, 1930:58–76, 1930.

[80] Roelof Vos and Saeed Farokhi. Review of fundamental equations. In *Introduction to Transonic Aerodynamics*, pages 62–69. Springer, 2015.

[81] Sameer Vyas. Ansys meshing user's guide. URL https://www.academia.edu/27974461/ANSYS_Meshing_Users_Guide.

[82] R W. Staufenbiel and U.-J Schlichting. Stability of airplanes in ground effect. *Journal of Aircraft - J AIRCRAFT*, 25:289–294, 04 1988. doi: 10.2514/3.45562.

[83] GJ Walker, AHD Fougner, SP Younger, and TJ Roberts. Aerodynamics of high speed multihull craft. In *Fourth International Conference on Fast Sea Transportation*, volume 1, pages 133–138, 1997.

[84] Setyawan Bekti Wibowo, TA Rohmat, et al. An evaluation of turbulence model for vortex breakdown detection over delta wing. *Archive of Mechanical Engineering*, 65(3), 2018.

[85] C Wieselsberger. Wing resistance near the ground. 1922.

[86] Chester H Wolowicz, JS Brown Jr, and William P Gilbert. Similitude requirements and scaling relationships as applied to model testing. 1979.

[87] Xiaoping Xu and Zhou Zhou. Study on longitudinal stability improvement of flying wing aircraft based on synthetic jet flow control. *Aerospace Science and Technology*, 46:287–298, 2015.

[88] Wei Yang, Feng Lin, and Zhigang Yang. Three-dimensional ground viscous effect on study of wing-in-ground effect. In *The third international conference on modelling and simulation (ICMS2010), Wuxi*, pages 165–168, 2010.

[89] Zhi-Gang Yang, Wei Yang, and Qing Jia. Ground viscous effect on 2d flow of wing in ground proximity. *Engineering Applications of Computational Fluid Mechanics*, 4(4):521–531, 2010.

[90] Jonathan Zerihan and Xin Zhang. Aerodynamics of a single element wing in ground effect. *Journal of aircraft*, 37(6):1058–1064, 2000.

[91] Yang Zhiyin. Large-eddy simulation: Past, present and the future. *Chinese journal of Aeronautics*, 28(1): 11–24, 2015.

A

MATLAB Script to modify fluid properties for a given Reynolds number and Mach number

```
clc
clear

M     = 0.2;                                % Mach number
Re    = 1e7;                                % Reynolds number
R     = 286.9;                              % Specific gas constant for air (J/kgK)
gamma = 1.4;                                % Ratio of specific heat
c     = 1.1;                                % Wing root chord (meters)
P     = 101325;                             % Refernce pressure of our problem (Pa)
T     = 288.15;                             % Ambient temperature (K)

func  = @(Mach) 1 + (gamma-1)/2*Mach^2;

%%%Calculated Properties

Pt    = P*func(M)^(gamma/(gamma-1));        %Total Pressure
Tt    = T*func(M);                          %Total Temperature
rho_t = Pt/(R*Tt);                          %Total Density
rho   = rho_t/(func(M))^(1/(gamma-2));      %Density
V     = sqrt(gamma*R*T)*M;                  %Velocity of flow
mu    = rho*V*c/Re;                         %Calculated Viscosity
gpres = Pt-P;                               %Guage Pressure
```